EFFECTS OF LANTHANOID ION IMPLANTATION ON THE PHOTOLUMINESCENCE OF SILICON NANOCRYSTALS EMBEDDED IN SILICON NITRIDE FILMS

By

TRES ALLAN HARRIMAN

Bachelor of Science in Mechanical Engineering
University of Missouri - Columbia
Columbia, Missouri
2003

Submitted to the Faculty of the
Graduate College of the
Oklahoma State University
in partial fulfillment of
the requirements for
the Degree of
MASTER OF SCIENCE
July, 2008

COPYRIGHT

By

TRES ALLAN HARRIMAN

July, 2008

EFFECTS OF LANTHANOID ION IMPLANTATION ON THE PHOTOLUMINESCENCE OF SILICON NANOCRYSTALS EMBEDDED IN SILICON NITRIDE FILMS

Thesis Approved:

Don A. Lucca

Thesis Adviser

C. Eric Price

Ranga Komanduri

A. Gordon Emslie

Dean of the Graduate College

ACKNOWLEDGMENTS

I would like to thank my advisor Dr. Don A. Lucca for his guidance and support throughout my graduate studies. I am grateful for the opportunity to have worked in his lab on such an exciting topic and to have had such close interactions with his fellow collaborators and colleagues. I am also thankful for the invaluable classroom teaching experience and responsibility that I was afforded. I would also like to thank my committee members -Dr. C. Eric Price and Dr. Ranga Komanduri- for their valuable comments and suggestions. I would like to extend my gratitude to Dr. Michael Nastasi and Dr. Jung-Kun Lee for their technical and intellectual guidance, as well as Dr. Gun-Yong Sung and his group for synthesizing and providing specimens.

I would like to thank my colleagues in the Ultraprecision Surfaces Group, especially Dr. Rudy Ghisleni, Mr. Ben Dvorak, and Ms. Golnaz Bassiri for all of their help. My time at OSU would not be complete without mentioning the wonderful guidance and support that Dr. C. Eric Price provided.

Finally I would like to thank my parents, brother, extended family, and friends for their support and encouragement. Thank you Lisa for your patience, companionship, encouragement, and love.

This work was performed, in part, at the Center for Integrated Nanotechnologies, a U.S. Department of Energy, Office of Basic Energy Sciences user facility at Los Alamos National Laboratory (Contract DE-AC52-06NA25396) and Sandia National Laboratories (Contract DE-AC04-94AL85000).

This material is based upon work supported by the National Science Foundation under Grant No. CMMI-0529085. Any opinions, findings, and conclusions or recommendations expressed in this material are those of the author and do not necessarily reflect the views of the National Science Foundation.

TABLE OF CONTENTS

1 Introduction **1**

1.1 Motivation for the Present Study 1

1.2 Objectives 2

1.3 Approach 2

2 Background **3**

2.1 Quantum Confinement 3

2.2 Silicon 4

2.2.1 Characteristics 5

2.2.2 Light Emission and Nanostructures 7

2.3 Lanthanoid Elements 12

2.3.1 Characteristics 12

2.3.2 Doping in Si 15

2.4 Optical Spectroscopy 18

2.4.1 Photoluminescence Spectroscopy 18

2.4.2 Raman Spectroscopy 18

2.5 Confocal Microscopy 22

3 Experimental **24**

3.1 Synthesis of Si nanocrystals 24

3.2 Lanthanoid Ion Implantation 26

3.3 Instrumentation 26

3.3.1 Laser 27

3.3.2 Objectives 27

3.3.3 Confocal pin-hole 27

3.3.4 Monochromator/Detector 29

3.4 Procedure for the Photoluminescence and Raman Experiments 29

3.5 Probing Depth 31

4 Results and Discussion **32**

4.1 As-Grown Films 32

4.1.1 Photoluminescence response 32

4.1.2 Raman response 34

4.2 Lanthanide Ion Implantations 40

4.3 Ce Implantation 44

4.3.1 Photoluminescence Enhancement 44

4.3.2 Concentration Quenching 50

4.4 Energy Transfer Mechanism 52

5 Conclusions and Future Work **58**

5.1 Conclusions 58

5.2 Future Work 60

Bibliography **61**

A Operation of WITec Alpha SNOM in Confocal Mode **74**

LIST OF TABLES

2.1 Crystalline Si properties at 300 K. 6

2.2 Commonly observed emission bands of Nd^{3+}, Eu^{3+}, and Tb^{3+}. 13

3.1 Absorption coefficient and approximate probing depth of materials using 325 and 532 nm excitation 31

4.1 Summary of Si nanocrystal PL intensity change and spectral shifting, relative to the as-grown film, due to Ce implantation. 48

LIST OF FIGURES

2.1 Density of state (DOS) functions for a) bulk material, b) a quantum wire, and c) a quantum dot. 5

2.2 Energy band diagram for Si and InP. 7

2.3 Diagram of the excitation and recombination processes that can result in photoluminescence. 19

2.4 Interaction between light and matter. 20

2.5 Energy model of the Raman effect. 21

2.6 Diagram showing a confocal setup where rays from the focal plane pass through the pinhole but rays from other planes are blocked. 22

3.1 Schematic of the amorphous SiN_x film containing Si nanocrystals on a Si substrate. . 25

3.2 Schematic showing the components and beam path of the WITec Alpha SNOM configured in a reflection confocal mode, and the monochromator and CCD. (1) white light source, (2) 50:50 beamsplitter, (3) holographic bandpass filter, (4) laser blocking filter, (5) rotating turret holding three gratings, and (6) fiber coupler and a single mode fiber. 28

3.3 Integrated intensity of the 520 cm^{-1} Si peak as a function of focus distance with respect to the surface (positive value is above the surface). System z-resolution is given by the FWHM. Other than fiber diameter, experimental parameters remained constant implying the decrease in the integrated intensity is the result of decreased signal throughput. 30

4.1 Room temperature confocal PL spectra of 200 nm thick Si:SiN_x films grown on Si. The nominal emission of the nc-Si went from red to green to blue as nc-Si decreased. Spectra are not normalized. 33

4.2 Room temperature confocal PL spectra of 200 nm thick Si:SiN_x films grown on SiO_2. The nominal emission of the nc-Si went from red to yellow to green to blue as nc-Si decreased. 34
4.3 Room temperature confocal Raman spectra of 200 nm thick Si:SiN_x films grown on Si that contain small and medium Si nanocrystals. Both spectra have been normalized using the 3TO Si peak at 1450 cm^{-1}. 36
4.4 Room temperature confocal Raman spectra of (a) 200 nm thick amorphous SiN_x film grown on bulk Si that contains medium Si nanocrystals and (b) bulk crystalline Si. The inset shows structure of the lower intensity peaks and spectra (a) has been shifted up for clarity. All spectra have been normalized with respect to the 520 cm^{-1} peak. 37
4.5 Confocal Raman spectra of bulk crystalline Si implanted with Ar at increasing fluences leading to an increasingly amorphous structure. 38
4.6 Room temperature confocal Raman spectra of 200 nm thick amorphous SiN_x films grown on SiO_2. Nominal PL emission of the nc-Si appeared in the red, yellow, green, and blue spectral regions as the nc-Si size decreased. Inset shows details of the blue and green emitting films. 39
4.7 Room temperature confocal PL spectra of 200 nm thick amorphous SiN_x films grown on Si implanted with various lanthanide ions. Vertical lines show the approximate spectral centers of the as-grown films.(Note that the spectra from the Ce implanted small and medium Si nanocrystals is not fully shown as it is discussed further in Section 4.3). 41
4.8 Room temperature confocal PL spectra of 200 nm thick amorphous SiN_x films grown on Si implanted with various lanthanide ions after the 500 °C heat treatment. Vertical lines show the approximate spectral centers of the as-grown films. 42
4.9 Room temperature confocal PL spectra of 200 nm thick amorphous SiN_x films grown on Si implanted with various lanthanide ions after the 800 °C heat treatment. Vertical lines show the approximate spectral centers of the as-grown films. 43
4.10 Room temperature confocal PL spectra of 200 nm thick amorphous SiN_x films grown on Si. Ce implanted films are compared with those of the as-grown film. Vertical lines show the approximate spectral centers of the as-grown films. 45

4.11 Room temperature confocal PL spectra of 200 nm thick amorphous SiN_x films grown on Si. Ce implanted films heat treated at 500 °C are compared with those of the as-grown films. Vertical lines show the approximate spectral centers of the as-grown films. 46

4.12 Room temperature confocal PL spectra of 200 nm thick amorphous SiN_x films grown on Si. Ce implanted films heat treated at 800 °C are compared with those of the as-grown films. Vertical lines show the approximate spectral centers of the as-grown films. 47

4.13 Room temperature confocal PL spectra of 200 nm thick amorphous SiN_x films grown on bulk Si that contain a) small, b) medium, and c) large Si nanocrystals. The as-grown films and films implanted with Ce ions at fluences of 3×10^{19}, 5×10^{20}, and 1×10^{26} ions/cm^2 are shown. 51

4.14 PL enhancement of Si nanocrystals after the implantation of Ce ions at fluences of 3×10^{19}, 5×10^{20}, and 1×10^{26} ions/cm^2. Enhancement is given as a fraction of the the intensity of the as-grown film for each size of nanocrystal. Note that fluence is plotted on a log scale. 53

NOMENCLATURE

a_B . . . . Effective Böhr radius

AFM . . . . Atomic force microscopy

a-Si . . . . Amorphous silicon

BP . . . . Band pass

C . . . . Confinement parameter

CCD . . . . Charge-coupled device

c-Si . . . . Crystalline silicon

CVD . . . . Chemical vapor deposition

d . . . . Particle diameter

d . . . . Distance between grates

d_z . . . . Depth resolution

DOS . . . . Density of states

e . . . . Electron charge

E . . . . Energy

$E_{nanocrystal}$ . . . . Band-gap of nanocrystal

E_{bulk} . . . . Bulk band-gap

f . . . . Focal length of monochromator

FRET . . . . Fluorescence (Förster) resonant energy transfer

FWHM . . . . Full width at half maximum

h . . . . Planck's constant

$\hbar$ . . . . Reduced Planck's constant

HRTEM . . . . High-resolution transmission electron microscopy

J_{da} . . . . Overlap of donor emission and acceptor absorption spectra

k . . . . Thermal conductivity

k . . . . Orientation factor

k_{FRET} . . . . Rate constant of FRET

k_{OP} . . . . Rate constant of all other processes

L .... Length between walls of potential well

LA .... Longitudinal acoustical

LED .... Light emitting diode

LO .... Longitudinal optical

LPCVD .... Low-pressure chemical vapor deposition

m .... Mass

m_e^* .... Effective mass of electron

m_h^* .... Effective mass of hole

n .... Index of refraction

n .... Positive integer

NA .... Numerical aperture

NBE .... Near-band edge

nc-Si .... Silicon nanocrystal

NDT .... Nondestructive Technique

p .... Momentum

PECVD .... Plasma enhanced chemical vapor deposition

PL .... Photoluminescence

PLE .... Photoluminescence excitation

R_o .... Donor/acceptor separation distance when FRET is 50%

sccm .... Standard cubic centimeters per minute

SNOM .... Scanning near-field optical microscopy

T_m .... Melting temperature

TA .... Transverse acoustical

TEM .... Transmission electron microscopy

TO .... Transverse optical

ULSI .... Ultra large scale integration

UV .... Ultraviolet

v .... Velocity

W .... Larger of the monochromator entrance width or CCD pixel size

ϵ .... Relative dielectric constant

λ .... Wavelength

Φ_d .... Donor quantum efficiency

π-Si .... Porous silicon

τ .... Fluorescence lifetime

θ_o .... Half angle of the objective

2TA .... 2nd order transverse acoustical

2TO .... 2nd order transverse optical

3TO .... 3rd order transverse optical

Chapter 1

Introduction

1.1 Motivation for the Present Study

Devices containing integrated circuits have become commonplace in all facets of our daily lives. As more demand is placed on these devices to perform more functions, in less time, and in a smaller space, the desire to use photons instead of electrons becomes more enticing. Si nanocrystals (i.e., particles with a crystalline structure that are 1 to 10 nm in size) have become of key interest due to their potential of being easily integrated into existing Si-based circuits and the fact that by varying their size their band-gap can be shifted throughout the visible and infrared spectra. While the development of light based computers is a considerable distance in the future, Si nanoparticles have the potential of being integrated into other optoelectronic devices. Conceivably this could first appear as fixed wavelength light emitting devices (LEDs) that could be custom made to a specific visible wavelength or even be used for broad-band white light emission. With the potential to tune the band-gap *in situ* through an applied strain, the creation of a new class of advanced infrared sensors that can be used in high sensitivity and multi-spectral applications ranging from remote temperature sensing, trace gas sensing of chemical and biological species, military target discrimination and identification, and ground-based astronomy is feasible. Understanding the effects of quantum confinement, surface chemistry, dopants, and strain are all essential for creating reliable, optimized devices.

1.2 Objectives

The objective of the present study is to investigate the enhancement of light emission from a Si based material system, namely, SiN_x films containing Si nanocrystals by means of implanting lanthanoid ions. Although light emission is known to occur from Si nanocrystals embedded within thin films, a method of increasing the light emission intensity is highly desirable and would make investigations into the coupled effects of applied strain and quantum confinement easier. By including lanthanoid ions within the SiN_x films that contain Si nanocrystals, there are two possible enhancements that could take place. First, the lanthanoid ions could emit light and the Si nanocrystals help to increase the efficiency of this emission, as has been reported for Er ions [1–6]. The emitted light wavelength will be dependent upon the type of lanthanoid ion implanted. Second, where the lanthanoid ions act as a sensitizer to the emission from the Si nanocrystals thus leading to higher intensity light output from the nanocrystals. The emitted light wavelength would be dependent upon the size of the nanocrystal.

1.3 Approach

In the present work, photoluminescence (PL) spectroscopy was used first to investigate the light emission from different sizes of Si nanocrystals that were embedded within amorphous SiN_x films grown with plasma enhanced chemical vapor deposition (PECVD). Raman spectroscopy was used to investigate the atomic bonding of the thin films. Ion-implantation was carried out on the specimens using different lanthanoid ions (Ce, Nd, Eu, or Tb) followed by a series of heat treatments to reduce any damage caused by the ion implantation process. The implanted films were examined using PL spectroscopy prior to and after each heat treatment cycle. Based on results of the initial study of the implanted specimens using a single fluence and each of the four lanthanoid ions, attention was focused on Ce and specifically the effect of Ce ion fluence on the PL emission of the films containing Si nanocrystals.

Chapter 2

Background

2.1 Quantum Confinement

Since quantum confinement is one of the major effects on the behavior of materials at nanometer length scales, such as those in this study, a brief background on the topic is given [7]. In quantum mechanics, a particle (e.g., an electron) can be described by a wavefunction in the form of a solution to the Schrödinger equation. When the length scale of one or more of the physical dimensions of a body is of the order of a tens of nanometers, the electrons (and holes) in that body are confined to a limited space. This physical confinement places constraints on the allowable wavefunctions of the electrons. An example of this is the classic problem of a particle in a box [7].

For the 1-D case, if one has two infinitely tall energy barriers separated by a distance of L, only waves that have nodes at both barriers are allowable. This implies that only standing waves are allowed giving $L = n\lambda/2$, where n is a positive integer and λ is the wavelength. Using the de Broglie equation, $\lambda = h/p$, where h is Planck's constant and p is the particle's momentum, the momentum of the particle represented by the standing wave as $p = h/\lambda = hn/2L$. Finally the energy of the particle is found to be $E = \frac{1}{2}mv^2 = p^2/2m = h^2n^2/8mL^2$. The energy is only allowed to take discrete values since n is a positive integer. Although more complicated, it can be shown that for both the 2-D and 3-D cases, the allowed energy states take on discrete values.

In bulk materials the natural radius of a bound electron-hole pair, or exciton, is given by the Böhr radius and is typically between 1 and 10 nm depending upon the semiconductor. The Böhr radius of the exciton is the critical length that determines the degree of quantum confinement. Weak confinement is considered to begin when the radius of the particle is approximately twice that of the Böhr radius. When the radius of the particle is approximately equal to the Böhr radius and

smaller, it is described as strongly confined. The equation for the Böhr radius of an exciton in a bulk semiconductor is given by

$$a_B = \frac{\hbar^2 \varepsilon}{e^2} \left(\frac{1}{m_e^*} + \frac{1}{m_h^*} \right) \tag{2.1}$$

where $\hbar$ is the reduced Planck's constant, ε is the relative dielectric constant, e is the electron charge, m_e^* is the effective mass of the electron, and m_e^* is the effective mass of the hole [8].

If one starts with a piece of bulk material (3-D body) and reduces one of the dimensions to a few nanometers, a quantum well (2-D body) is created. If one of the other dimensions is again reduced to a few nanometers, a quantum wire (1-D body) is created. If the final dimension is reduced to a few nanometers, a quantum dot (0-D body) is created.

In the case of a quantum dot, which is confined in all three dimensions, the density of states takes on a series of discrete values. This same behavior is observed in single atoms or molecules, which explains why quantum dots are sometimes referred to as artificial atoms. Figure 2.1 shows the density of states for bulk material (3-D), a quantum wire (1-D), and a quantum dot (0-D). The density of states represents the total number of solutions to the Schrödinger equation per volume for a particular energy.

Effective mass approximation predicts that the band-gap of a spherical semiconductor nanocrystal increases proportionately to the inverse square of its diameter [9]. This relationship between the material's bulk band-gap, the particle size, and the particle's band-gap is $E_{particle} = E_{bulk} + C/d^2$, where $E_{particle}$ is the energy gap of the zero dimensional spherical particle, E_{bulk} is the band-gap of the bulk material, C is the confinement parameter, and d is the diameter of the particle in nm. This implies that for light emission from quantum confined particles, as they become smaller, the band-gap increases and the wavelength of the emitted light decreases (blue shifts). Ultimately, this means that if one has the ability to control the nanoparticle size, it is possibly to tune the emission from the nanoparticle to a desired wavelength.

2.2 Silicon

With the continual increase in needed bandwidth for inter- and intra-chip connections, optoelectronic devices that are compatible with current silicon-based ultra large scale integration (ULSI) technology are seen as a necessity to avoid bottlenecks using current electrical connections [10]. Use in integrated circuits is just one possible practical application for Si nanoparticles. Other applications that could potentially be realized in the shorter term include light emitting diodes (LEDs), advanced sensors capable of high sensitivity and multi-spectral response, trace gas sensors, biological species sensors,

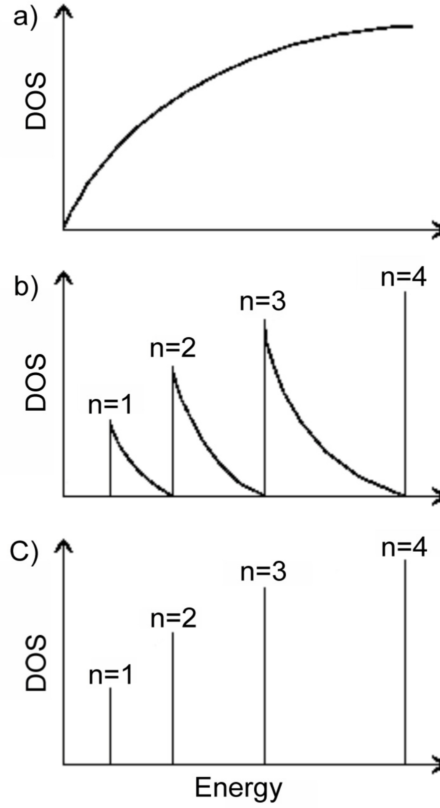

Figure 2.1: Density of state (DOS) functions for a) bulk material, b) a quantum wire, and c) a quantum dot.

non-volatile memory [11], and solar cells [12].

2.2.1 Characteristics

Table 2.1 lists some relevant properties of Si.

Crystalline Si, as a result of its diamond structure translation symmetry, has a well known Raman peak near 520 cm^{-1} due to triply degenerate optical phonons. In an ideal, stress-free, bulk Si crystal, the peak is a single strong Lorentzian and is centered at 520.3 cm^{-1} with a full width at half maximum (FWHM) of $\sim$ 3 cm^{-1} [19]. In reality its frequency is sensitive to elastic strain, thermal effects, and defects, while its width and symmetry are sensitive to size effects and defects [20]. Of these influences the strain effect on the Raman frequency is the most dominant and is given by

$$\sigma = -434 \, \Delta\omega \tag{2.2}$$

where σ is stress in MPa, and $\Delta\omega$ is the Raman shift of the 520 cm^{-1} Si peak in cm^{-1} [21]. Other

Table 2.1: Crystalline Si properties at 300 K.

Physical Property	**Symbol**	**Value**	**Units**	**Reference**
Structure		Diamond		[13]
Atomic Weight		28.086		[13]
Density		2.3290	g cm^{-3}	[13]
Melting Temperature	T_m	1410	°C	[14]
Energy Band Gap	E_g	1.1242	eV	[15]
Electron Effective Mass	m_e^*	1.09	m_e	[15]
Hole Effective Mass	m_h^*	1.15	m_e	[15]
Intrinsic Carrier Concentration	n_i	1.07×10^{10}	cm^{-3}	[15]
Bulk Böhr Radius	a_B	∼4.3	nm	[16]
Lattice Constant	a_0	5.43102	Å	[17]
Thermal Expansion Coefficient	da_0/dT	1.41	10^{-5}Å K^{-1}	[17]
Thermal Conductivity	k	147	W m^{-1} K^{-1}	[7]
Optical absorption				
at 325 nm	α	1.24×10^6	cm^{-1}	[18]
at 532 nm	α	6.69×10^3	cm^{-1}	[18]

commonly observed Raman peaks in crystalline Si are at 300 cm^{-1} which is associated with the second-order transverse acoustical (2TA) phonon and a broad peak at 960 cm^{-1} that is associated with the second-order transverse optical phonon (2TO) [22].

In the case of amorphous Si, there is a Raman band between 40 and 200 cm^{-1} associated with the TA phonon and a Raman band between 440 and 520 cm^{-1} associated with the TO phonon [23]. Since by definition there is no translation symmetry in the amorphous structure, the Raman spectrum is dependent upon the density of phonon states within the material, which results in a broad band instead of a sharp peak.

Light emission from bulk Si is extremely inefficient due to the indirect nature of its band-gap. As can be seen from the band structure shown in Fig. 2.2, for a direct band-gap semiconductor the highest energy of the valence band and the lowest energy of the conduction band occur at the same wavevector k. This implies that electron-hole recombination is momentum conserving and the recombination results in the emission of a photon with energy equivalent to that of the band-

gap. In the case of an indirect band-gap (e.g., Si), the highest energy of the valence band and the lowest energy of the conduction band occur at different wavevectors k, therefore momentum is not conserved. In order to overcome the difference in wavevectors (and therefore the difference in momentum), a phonon must be involved in the electron-hole recombination.

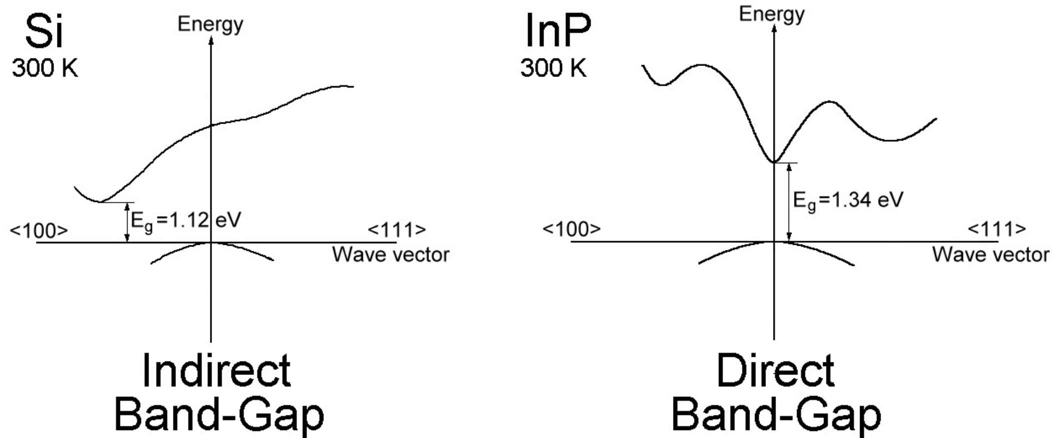

Figure 2.2: Energy band diagram for Si and InP.

2.2.2 Light Emission and Nanostructures

Bulk Si, despite its usefulness for producing integrated circuits, is an extremely inefficient light emitter due to its indirect band-gap. A number of methods have been employed in attempts to realize efficient and tunable light emission which range from creating atomic layer superlattices, alloying, incorporating impurity centers, and quantum confinement of carriers [24, 25].

Superlattices are created by alternating very thin layers of different materials, which leads to a larger lattice constant and thus reduced Brillouin zone along one axis. With proper selection of the layer thicknesses the conduction band minimum can be shifted, as a result of Brillouin zone folding, so that the final band-gap is of a direct nature [26]. Si in a superlattice configuration with either Ge or SiO_2 has achieved light emission; however, the intensity of the red or more commonly infrared light is weak and often quenched at room temperature [27–29].

Band structure engineering through alloying with other group IV elements (e.g., Ge or Sn) has also been investigated to induce shifting of the band-gap. Both photoluminescence (PL) and electroluminescence (EL) of $Si_{1-x}Ge_x$ has been shown to produce a broad emission that is dependent upon the Ge concentration. The band-gap remains indirect but can vary from 1200 to 2000 nm for $0.1 < x < 0.5$ [30, 31]. Despite the emission, its relative intensity is weak and quenches at

temperatures above 80 K. Alloying with Sn is another possible route to Si light emission based on work which showed the band-gap of $Ge_{1-x}Sn_x$ becomes direct for x = 0.23 [32].

Inclusion impurities in a pure bulk Si crystal opens the possibility of creating states within the band-gap (i.e., defect states) which offers another avenue for electron-hole recombination and possibly photon emission. Studies on the effects of impurity centers have been conducted on a wide range of atomic species, for example, C, S, Er, Be, In, Al-N, and Se [33–36] (see also reviews by Davies [37] and Kimerling et al. [38]). According to Iyer and Xie [24], there are three observations common to the luminescence behavior of isoelectronic centers in Si: i) it is extremely weak at room temperature, ii) quantum efficiency is a few percent at low temperatures, and iii) non-radiative recombinations compete with radiative combination as a result of long emission lifetimes (milliseconds).

Quantum confinement has been one of the more widely studied methods of light generation in Si. In order to induce quantum confinement of carriers in a material the ability to create structures with dimensions on the order of the Bohr radius or smaller is critical. Prior to reviewing Si nanostructures, their synthesis, and properties, a description of commonly used terms is needed, especially considering the frequency with which they are interchanged, often erroneously. A nanostructure is any continuous volume of material that has a length scale of at least one-dimension on the order of 100 nanometers or less [39]. Nanoparticles are a subset of nanostructures, in which all three dimensions are on the length scale in the order of 100 nanometers or less. Nanoparticles can be either amorphous, having no long range order in the bonding of their constituent atoms/molecules, or crystalline if there is a repeated order in the constituent atoms/molecules (i.e., a nanocrystal). Quantum wells, quantum wires, and quantum dots are all nanostructures that have dimensions smaller than the Böhr radius of the material (thus inducing quantum confinement) in one-dimension, two-dimensions, and three-dimensions, respectively.

Although porous Si (π-Si) created by partial electrochemical dissolution has been known since 1956 [40], investigations into its morphology [41] and optical properties [42, 43] came much later. In 1990 Canham observed visible light emission from π-Si and attributed the emission to quantum confinement effects from the network of nanowires created after electrochemical dissolution [44]. Despite all the attention given to the findings of Canham in the literature, it was in fact Takagi et al. [45] a few months prior who first observed visible light emission from Si at room temperature in the form of nanocrystals embedded in a thin film of SiO_2. Since the emission energy was found to be inversely proportional to the square of the nanocrystal diameter, the light emission was attributed to quantum confinement. The discovery of room temperature visible light emission from quantum confined Si spurred a wide range of investigations into nanostructured Si.

Much of the early research into Si nanostructures investigated π-Si and Si-rich SiO_2 (Si nanoparticles in a SiO_2 matrix) just as Canham and Takagi et al. did. The typical method for creating π-Si is to apply a small current to a bulk Si crystal that is in a HF solution. Anodization of the Si wafer speeds up the chemical dissolution which generates a myriad of small holes running perpendicular to the surface. The resulting properties and degree of porosity are dependent upon electrolyte composition, substrate resistivity and type, anodization parameters, and post-dissolution treatments.

While light emission from π-Si has been reported from near infrared to blue, its fragility, high reactivity, spontaneous oxidation in air, and degradation of luminescence over time all make it poorly suited for optoelectronic devices [46]. Furthermore, the mechanism responsible for luminescence has been widely debated; emission from band-to-band transitions, emission from oxides, and emission due to surface states have all been proposed (see review by Fauchet [47] for details). Much of this debate is likely due to the result of different recombination mechanisms dominating for different sizes of particles that have been oxidized by contact with air for as little as a few seconds [48]. Wolkin et al. [48] showed that free exciton recombination was responsible for the emission in Si particles between 1 and 5 nm in size, as long as the particles remained passivated by H. However, once the same particles were oxidized as a result of exposure to O, there were three distinct regions where the recombination mechanism was dependent upon size. From 5 to $\sim$2.9 nm in size, free exciton recombination led to the expected blue-shift in emission with decreasing particle size. From $\sim$2.9 to 1.6 nm recombination of a trapped electron and free hole led to a blue-shift in emission but at a slower rate than would be expected due to purely quantum confinement effects. Finally, for particles smaller than $\sim$1.6 nm, the emission is due to the recombination of trapped excitons, implying that the emission energy is constant even as particle size is decreased.

Takagi et al. [45] created 500 nm thick Si-rich SiO_2 thin films through a process in which microwave plasma decomposition of SiH_4 created Si nanoparticles. These particles ranged in diameter from 2.5 to 14 nm depending upon the gas flow rate and were applied to the substrate by directing them into a collection chamber via a nozzle. Each nanoparticle was found to have an amorphous shell approximately 1 nm thick which upon exposure to a room temperature, high humidity environment oxidized over a period of 1 hour; beyond this time the nanoparticle itself began to oxidize. PL emission was not observed prior to oxidation, nor for particles larger than 6 nm in diameter. Based on this and the fact that the emission energy was inversely proportional to the square of the nanoparticle diameter, the light emission was attributed to the quantum confinement of carriers in the Si nanoparticles.

Synthesis Techniques

A wide variety of techniques have been developed to synthesize Si nanoparticles either on or embedded within a variety of substrates. Ion implantation [49, 50], chemical vapor deposition (CVD), plasma-enhanced chemical vapor deposition (PECVD) [51], low-pressure chemical vapor deposition (LPCVD) [52], electron-beam lithography in combination with reactive ion etching [53], laser ablation of bulk Si [46], solid phase crystallization, liquid solution phase synthesis [54], and gas phase synthesis are some of the more commonly reported methods. As previously pointed out for the case of π-Si, spontaneous oxidation and degradation of luminescence over time make it clear that the nanostructure should ideally be protected within a host material that will isolate the structure and passivate the surface interface. Early studies focused primarily on SiO_x while much attention recently has shifted to SiN_x. Details of synthesis techniques and host materials follow.

Ion implantation of Si ions into either an oxidized layer on a Si wafer or a fused silica substrate, and a subsequent annealing cycle have been shown to produce PL active nanocrystals [49, 50]. After implantation with fluences between 10^{16} and 10^{17} ions/cm^2, an emission band was observed near 620 nm in the as-implanted specimens that was attributed to excess Si defect states. After a high temperature anneal ($> 1100\,^{\circ}$C) the defect peak disappeared and a new peak between 730 and 800 nm appeared that was attributed to the creation and emission of nanocrystals [49].

Heath reported a liquid-solution-based synthesis technique of Si nanocrystals based on the reduction of $SiCl_4$ and $RSiCl_3$ (R = H, octyl) using sodium metal in a nonpolar organic solvent [54]. Reactions were carried out at $385\,^{\circ}$C and pressures > 100 atm. under rapid stirring for 3 to 7 days. For the reaction using $HSiCl_3$ the resulting crystallites were found to have a size range of 5 to 3000 nm and a hexagonal shape. In the case of octyl-$SiCl_3$, the particles had a narrow size range (5.5 ± 2.5 nm), again with a hexagonal shape.

Laser ablation of bulk crystalline Si in the presence of O has been found to create SiO_x only in those areas exposed to the laser [46]. It was observed that increasing laser fluence led to more O incorporation, which in turn led to a PL peak between 540 and 630 nm associated with O defects. After annealing at $1000\,^{\circ}$C a second peak at 620 nm appeared and with longer annealing times red-shifted. This behavior led to the peak being identified as emission from Si nanostructures.

Valenta et al. [53] used electron-beam lithography to create resist dots as small as 50 nm in diameter on the surface of a Si wafer with a 25 nm thick thermal oxide layer. Areas not exposed to the electron-beam were then etched using CHF_3/O_2 to etch the top oxide layer, followed by Cl reactive ion etching of the Si substrate. Pillars 200 nm tall remained, which were first thermally

oxidized at 900 °C for 5 hours and then at 1000 °C for 12 min to further shrink the pillars. A final annealing cycle for 30 min at 400 °C in a mixture of H_2 and N_2 gas was performed to passivate the surface of the pillars. PL measurements taken over a large area of the specimen showed a broad peak (FWHM of ∼100 nm) centered at 710 nm. PL measurements of single pillars were much more narrow (FWHM of ∼50 nm) and depending upon the specific pillar was centered anywhere from 660 to 785 nm.

An rf co-sputtering method was also found to be capable of producing semiconductor nanocrystals that are encapsulated within a matrix. Fujii et al. [4] used this process to co-sputter Si and SiO_2 onto fused quartz plates. After the depositing of a 1 μm thick layer, the specimens were annealed at 1100 °C for 30 minutes in an N_2 environment. Particle size was controlled by a combination of the amount of Si that was sputtered and the annealing time. By increasing the amount of Si used in the process, the film can be made more Si rich, and by annealing for longer times the nanocrystals have more time to grow in size via an Ostwaldt ripening (a larger particle will grow in size at the expense of smaller particles nearby it). What makes this method attractive is that dopants can be incorporated into the films by co-sputtering along with the other raw materials. Additionally, other semiconductors such as Ge can be used to create nanocrystals [55].

One of the more common methods has been chemical vapor deposition (CVD) and often for the sake of low temperature growth either the plasma-enhanced (PECVD) or low-pressure (LPCVD) types of CVD are employed [51, 52, 56]. Baron et al. [52] used the LPCVD method to grow Si quantum dots on the surface of Si_3N_4, SiO_2, and SiO_xN_y substrates. SiH_4 was used as the reactant gas, the temperature ranged from 570 to 610 °C, and the chamber pressure ranged from 0.035 to 0.2 Torr. Quantum dot sizes were between 4 and 7 nm with densities between 10^{11} and 10^{12} cm^{-2} depending upon the substrate.

PECVD has been used to create embedded Si quantum dots within a Si_3N_4 matrix; these quantum dots have been both amorphous [56] and crystalline [51] in structure. The amorphous Si quantum dots were grown using N_2-diluted 5% SiH_4 and high purity N_2 on a crystalline Si substrate. The flow rate of the SiH_4 was a constant 10 sccm while the N_2 was varied from 100 to 800 sccm to control the particle size. The growth chamber pressure, temperature, and plasma power were maintained at 0.5 Torr, 300 °C, and 6 W, respectively. The resulting amorphous quantum dot size was found to vary from 2.4 to 1.4 nm and had PL emissions ranging from 2.0 to 2.76 eV. The crystalline Si quantum dots were grown using Ar-diluted 10% SiH_4 and high purity N_2 on a crystalline Si substrate. Particle size was controlled by varying both the SiH_4 and N_2 flow rates from 4 to 12 sccm and 500 to 1800 sccm, respectively. The growth chamber pressure, temperature, and

plasma power were maintained at 0.5 Torr, 250 °C, and 5 W, respectively. The resulting crystalline quantum dot size was found to vary from 6.1 to 2.6 nm and had PL emissions ranging from 1.46 to 3.02 eV.

There are key differences between the use of SiO_2 and Si_3N_4 as matrix materials. Tunneling barriers at the Si/SiO_2 interface for holes and electrons are 3.8 and 3.15 eV, respectively, while for the Si/Si_3N_4 interface they are 2.0 and 1.5 eV for holes and electrons, respectively [57]. Based on these values the electric fields required to inject carriers into the oxide become comparable with the breakdown value of SiO_2, which makes the nitride a more attractive option for use in optoelectronic devices. Additionally, reports on observed emission wavelengths of nanoparticles embedded within Si_3N_4 span much more of the visible spectrum than do those of nanoparticles embedded within SiO_2. Kim et al. [51] showed that by changing the particle size in a Si_3N_4 matrix over the range from 6.1 to 2.6 nm, the emission energy could be shifted from 1.46 to 3.02 eV. In the case of a SiO_2 matrix, changing the particle size from 5.5 to 2.7 nm was found to shift the PL emission from 1.2 to 1.5 eV [58]. The reason for this difference is the presence of Si=O bonds in the SiO_2 that create size dependent levels for both holes and electrons, where the exciton in the Si nanocrystal can radiatively recombine [48]. Since the process is size dependent a blue-shift is observed, only at a slower rate than what would be expected for a model based solely on quantum confinement effects.

2.3 Lanthanoid Elements

2.3.1 Characteristics

According to the International Union of Pure and Applied Chemistry (IUPAC), the lanthanoids consist of the 15 elements with atomic numbers from 57 to 71 [59]. In the past these elements, along with Sc and Y, were commonly referred to as rare earth elements. IUPAC now generally disapproves of this description since "earth" is an obsolete term for an oxide and these elements have turned out to be relatively abundant in the earth's crust. All of the lanthanoids have similar chemical properties that are reasonably independent of their environment, due to the shielding of the partially filled 4f electron shell by the completely filled 5s and 5p shells [60]. The electron configuration of the lanthanoid elements used in the present study are $[Xe]6s^2 4f^1 5d^1$ for Ce, $[Xe]6s^2 4f^4$ for Nd, $[Xe]6s^2 4f^7$ for Eu, and $[Xe]6s^2 4f^9$ for Tb [61].

Regardless of the technique used to include the lanthanoids into the matrix material, they will typically have an oxidation state of +3. Luminescence from lanthanoid ions are noted by their sharp

peaks whose spectral location are, in most cases, invariant to the type of host matrix due to the previously mentioned shielding of the 4f electrons. Intensity and fine structure are known to vary with different host materials [62]. Table 2.2 shows some commonly observed emission bands for Nd^{3+}, Eu^{3+}, and Tb^{3+} along with the responsible transition; a more complete table of the energy levels for both doubly and triply ionized lanthanoids can be found elsewhere [63]. The transitions show the levels given by the spectroscopic notation $^{2S+1}L_j$, where S (total spin quantum number) and j (total angular momentum quantum number) are integers or half integers, and L (total orbital quantum number) is given by a letter (S, P, D, F, G, H, I, K...) which corresponds to a numeric value (0, 1, 2, 3, 4, 5, 6, 7...), noting that J is intentionally omitted.

Table 2.2: Commonly observed emission bands of Nd^{3+}, Eu^{3+}, and Tb^{3+} [64].

Ion	Transition	$\lambda_{emission}$
Nd^{3+}	$^4F_{3/2} \rightarrow {}^4F_{9/2}$	880 nm
	$\rightarrow {}^4F_{11/2}$	1060 nm
	$\rightarrow {}^4F_{13/2}$	1330 nm
Eu^{3+}	$^5D_0 \rightarrow {}^7F_0$	580 nm
	$\rightarrow {}^7F_1$	590 nm
	$\rightarrow {}^7F_2$	613 nm
	$\rightarrow {}^7F_3$	650 nm
	$\rightarrow {}^7F_4$	690 nm
	$\rightarrow {}^7F_5$	710 nm
Tb^{3+}	$^5D_4 \rightarrow {}^7F_6$	490 nm
	$\rightarrow {}^7F_5$	545 nm
	$\rightarrow {}^7F_4$	590 nm
	$\rightarrow {}^7F_3$	620 nm
	$\rightarrow {}^7F_2$	650 nm

In the case of Ce^{3+}, the observed emission varies based on the host matrix, but typically a broad blue emission is observed as a result of a $5d \rightarrow 4f$ transition. This transition is a parity-allowed electric dipole having a large oscillator strength. In some cases there is a single emission band, while under other conditions the single band splits into two distinct bands separated by approximately 2000 cm^{-1}. These two bands are the result of the $4f^1$ ground configuration splitting into two levels,

$^2F_{5/2}$ and $^2F_{7/2}$, which is due to spin-orbit coupling [65]. In addition to the splitting of the ground state, depending on the host material, strong crystal field splitting of the $5d$ level can occur as well. This manifests itself in the number of absorption bands which range between 2 and 5 individual bands [62]. As a result, Ce has been seen as a promising candidate for use in widely tunable solid state UV lasers.

Aitasalo et al. [66] observed a single $5d \rightarrow 4f$ emission centered at 455 nm for $Y_2SiO_5 : Ce^{3+}$ with an X_1-type structure. When the same group investigated the same chemical system, only with an X_2-type structure instead of the X_1-type, they observed two emission bands at 395 and 430 nm [67]. These two bands are separated by 2000 cm^{-1}, which is consistent with the spacing between the $^2F_{5/2}$ and $^2F_{7/2}$ levels. Lin et al. [68] investigated core/shell particles consisting of a 350 nm diameter silica cores and a 50 nm thick shell of lanthanoid doped Y_2SiO_5. TheY_2SiO_5 was found to have an X_1-type structure and for specimens doped with Ce^{3+} the emission spectra consisted of a single broad peak centered at 443 nm.

In an MgS matrix, there were two emission bands observed as a result of $5d \rightarrow 4f$ transitions, one at 520 nm due to the transition back to the $^2F_{5/2}$ ground state and a second at 580 nm due to the transition to the $^2F_{7/2}$ ground state [69]. Paulose et al. [70] found the emission of Ce^{3+} in phosphate glass to be a single broad peak centered at 362 nm. A CeF_3 thin film that was used as a Ce^{3+} dopant source was found to have a PL emission peak at 340 nm by Fang et al. [71] and 335 nm by Xie et al. [72].

Li et al. [73] investigated the solubility and optical properties of Ce^{3+} in $R_2Si_5N_8$ (R = Ca, Sr, and Ba). Maximum solubility of Ce^{3+} in $Ca_2Si_5N_8$ and $Sr_2Si_5N_8$ was found to be 2.5 mol % while the maximum in solubility in $Ba_2Si_5N_8$ was 1.0 mol %. Emission bands assigned to the $5d \rightarrow 4f$ transition of Ce^{3+} were centered at 470, 553, and 451 nm for the case of R = Ca, Sr, Ba, respectively. Differences in the solubility and emission were attributed to the relative size difference between the Ce ion and the R ion which was substitutionally replaced in the crystal. Similarly, de Graaf et al. [74] observed emissions from Ce-doped RSiAlON (R = Sc, Y, La, Gd) glasses that ranged from 380 to 500 nm depending upon what site the Ce ion takes up. If the site is ionic in nature, the emission has shorter wavelengths, while if the site is more covalent in nature (near non-bridging O) the emission has a longer wavelength.

2.3.2 Doping in Si

Studies involving lanthanoid ions can be broken down into two groups, the first are those where the light emission from the lanthanoid ion is of interest and the second are those where the lanthanoid ions sensitize the light emission from either the host matrix or some other structure within the matrix.

From the first group, some of the more widely studied systems are either bulk Si or films containing Si nanocrystals that have been doped with Er. The light emission of Er, with a wavelength of 1540 nm, is of particular interest to the telecommunications industry since its wavelength corresponds to the absorption minimum of optical fibers. Despite luminescence from Er-doped bulk Si being reported in 1983 [75], little advancement has been made due to the low solubility of Er and damage created during the doping process. Beyond the solubility limit of $\sim 1 \times 10^{18}$ cm^{-3}, $ErSi_2$ precipitates form and they have been found to be optically inactive [76]. Xie et al. [77] reported that the concentration of Er ions that would be required for LEDs is one to two orders of magnitude less than the solubility of Er in Si.

Defects created during the doping process, especially in the case of ion implantation, provides non-radiative recombination centers that degrade the efficiency of the system. To reduce the damage an anneal is performed, which also has the effect of activating the Er ions through the creation of Er-O complexes [78]. Michel et al. [78] found that for an implantation energy of 4.5 MeV, the optimal annealing temperature was 900 °C. At temperatures lower than this, the damaged structure was not sufficiently recrystallized, and above this temperature the Er-O complexes were broken down.

Much of the recent attention has been on the interaction between Si nanocrystals and Er ions, which was spurred by the findings of enhanced Er emission in π-Si [79–81]. It was then that Fujii et al. [4] demonstrated an energy transfer occurred from Si nanocrystals to Er ions by investigating Er doped SiO_2 films that contained Si nanocrystals. The specimens in the Fujii et al. study were created by a co-sputtering process, followed by an 1100 °C heat treatment. Although the resulting Si nanocrystal size could be controlled over a range from 2.7 to 5.5 nm, only the 2.7 nm nanocrystals were used in their initial study. It was observed that as the Er concentration increased, the Er related emission increased while the Si nanocrystal emission decreased. They found that the energy transfer was limited by the number of active Er-ions and not by the laser power density. Further, they measured the Er emission of their specimens as a function of excitation energy, as well as for an Er-doped SiO_2 specimen without nanocrystals. The specimens containing both Er ions and Si nanocrystals showed an Er emission for all excitation energies and did not have any distinct excitation

peaks. The specimen without Si nanocrystals only showed an Er emission with an excitation energy of 2.54 eV (corresponding to the $^4F_{15/2} \rightarrow ^4 F_{7/2}$ transition) and the emission was more than a factor of 100 less intense than what was observed for specimens containing Si nanocrystals under the same conditions.

A subsequent study by Fujii et al. [5] investigated the effect of Si nanocrystal size on the PL response of both Er and the Si nanocrystals. The nanocrystals ranged in size from 2.7 to 3.8 nm and resulted in a Si nanocrystal emission range from 1.55 to 1.38 eV. When the Er concentration was fixed at 0.04 at. %, the Er emission was found to decrease in intensity as the nanocrystal size increased from 2.7 to 3.8 nm. This trend was found to coincide with the intensity of the Si nanocrystal emission, where smaller particles were more intense than larger ones, such that the intensity ratio of Er emission to Si nanocrystal emission remained constant over all particle sizes. The increase in PL intensity of the Si nanocrystals with decreasing size was attributed to either an increase in oscillator strength and/or the decrease in Auger recombinations. No specific energy transfer mechanism was attributed to the observations.

Franzo et al. [82] also investigated the effect of Er ions, as well as Yb, Nd, and Tm ions, in SiO_2 containing Si nanocrystals and achieved doping with the use of ion implantation. For all ion species, PL was only observed in pure SiO_2 when the excitation source is resonant with a lanthanide transition. However, when Si nanocrystals are present in the film after growth via Si ion implantation and thermal annealing, the PL excitation dependence of the lanthanide ions was the same as that of the Si nanocrystals, weakly dependent on the excitation source. Additionally, the observed intensities of the lanthanide PL were more intense with the Si nanocrystals than without (a factor of 50 increase for Er, a factor of 5 for Nd, and a factor of 4 for Yb). It was also determined that the ions responsible for the emission were located in the SiO_2 matrix and not contained within the Si nanocrystal. This conclusion was drawn since the observed PL peaks were the same shape as that of lanthanide ions embedded in bulk SiO_2, which has a different PL spectra shape than lanthanide ions embedded in bulk Si. Since the Si nanocrystal and lanthanide ions responsible for the emission are not in direct contact, the energy transfer mechanism responsible must take place over a distance.

Priolo et al. [2] also used Er ion implantation to dope SiO_2 films that contained Si nanocrystals. Time resolved PL measurements using a 2.54 eV excitation source put the effective excitation cross section of the Si nanocrystals prior to Er doping at 8×10^{-16} cm^2. After Er implantation of the films the effective cross section of the Er ions was found to be 1.1×10^{-16} cm^{-2}, compared to 1.5×10^{-19} cm^{-2} for the same Er ion distribution in a pure SiO_2 substrate. The similarity in cross sections of

the Si nanocrystals before doping and the implanted Er ions post doping is an indication of a strong interaction between the Si nanocrystals and the Er ions. Additionally, concentration quenching was found to have the combined effect of increasing the excitation cross section while decreasing the PL decay time (and intensity). The optimal Er content was found to be 2×10^{20} cm^{-3}.

Although SiO_2 matrices have been the most widely reported in lanthanide doped Si nanocrystal systems, Si_3N_4 matrices have also been investigated. Two studies from Park et al. [83,84] investigated the effect of Er ions on the PL from 50 nm thick Si_3N_4 films that contained amorphous Si quantum dots. This study is different from those previously discussed because of the observed emission energy from the Si quantum dots. Those contained in SiO_2 in other studies typically had an emission for the smallest particles between 1.46 and 1.77 eV. The emission from the films with the smallest particles used in the studies by Park et al. had emissions as high as 2.64 eV. It was found that the Si quantum dots needed to be smaller than 2.0 nm to efficiently sensitize the Er ions. As the particle size increased, its surface area increased as well, along with the number of Er ions that it could interact with. But the optically active Er ions were then more closely spaced to each other and as a result Er-Er interactions led to concentration quenching.

In the case of Ce, it has been observed that the Si nanocrystal PL emission can be enhanced at the expense of the Ce ion emission. Fang et al. [71, 85] doped nc-Si in SiO_2 by evaporating a thin film of CeF_3 on the surface of the SiO_2. Upon a subsequent heat treatment, the Ce^{3+} diffuses into the SiO_2. Their nanocrystals were an average of 4 nm in diameter and were in a 150 nm thick layer of SiO_2, giving an emission near 1.77 eV. The thickness of the CeF_3 layer and the annealing temperature were both investigated. After annealing there was no evidence of the 4.28 eV emission of bulk CeF_3 or that of perturbed Ce^{3+} near 3.54 and 3.02 eV, which was attributed to an energy transfer from the Ce^{3+} ion to the nanocrystals. They found that by fixing either the CeF_3 thickness and varying the annealing temperature (or vice versa), there was an increase in intensity to some critical value and then a decrease. It was also seen that the spectral center followed the same pattern by first red shifting until the same critical value and then blue shifting. This behavior was explained by the particle size decreasing while going from the surface toward the substrate. So, as the annealing temperature increased and the Ce^{3+} ion diffused farther into the SiO_2, the average size of the nanocrystals that were being sensitized and producing more intense PL became smaller. Their largest shifts observed were a 25.7 meV red shift and a 31.9 meV blue shift.

2.4 Optical Spectroscopy

Two optical spectroscopy techniques were used as characterization tools in this study, namely, photoluminescence (PL) and Raman spectroscopy. Some background on the principles of these techniques are presented in the following.

2.4.1 Photoluminescence Spectroscopy

Photoluminescence spectroscopy is a nondestructive technique (NDT) that is useful in probing energy states and allowed electronic transitions in a material. In materials that are photoluminescence active, an incident photon with energy greater than the band-gap of the material is absorbed causing an electron to move from the valence band to the conduction band. This excited electron and its now empty location in the valence band (hole) is known as an electron-hole pair, or if they are bound, an exciton. When the excited electron returns to a lower energy state, a photon with less energy than the excitation source can be emitted.

A near-band edge emission (NBE) occurs when the electron moves from a state near the edge of the conduction band to the valence band. The energy of the NBE emission is quite close to that of the energy of the material's band-gap. A defect emission occurs when the electron recombination involves a defect state whose energy lies in the mid-band-gap. PL emission related to defect states will vary depending upon the energy level of the defect and the overall concentration of the defects. By analyzing the energy of the re-emitted light, insight into the band-gap, defect levels, defect types, and defect concentrations can be obtained.

2.4.2 Raman Spectroscopy

Raman spectroscopy is another nondestructive technique that is useful in probing the chemical bonding nature of materials. Although the effect was discovered in 1928 by Sir C.V. Raman [86], Raman spectroscopy did not see widespread use until the mid-1960s with the arrival of commercially available, reliable, continuous wave lasers [87]. The Raman effect is the result of a photon being inelastically scattered, where either the creation or annihilation of a phonon results in a net energy change of the incident photon [13]. As seen in Fig. 2.4, when incident light interacts with an object surface there are a variety of paths that the photon can take. At the surface of the material the light is either reflected or transmitted. Once inside the material, the light can take part in the PL process as described earlier, or it can be scattered either elastically or inelastically.

If we consider the energy diagram shown in Fig. 2.5, for an elastically scattered photon, referred

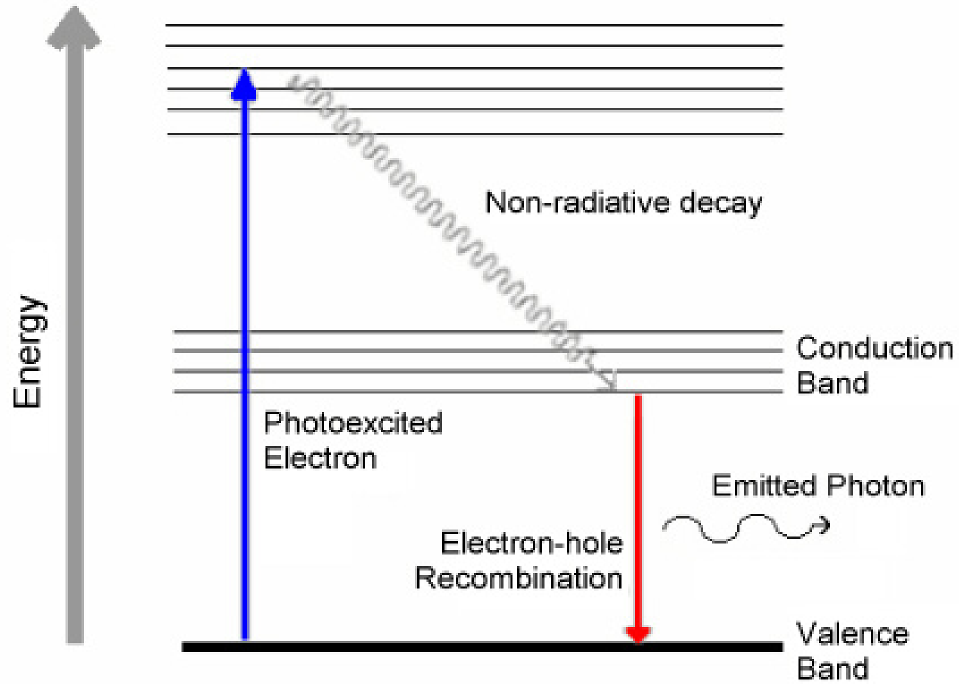

Figure 2.3: Diagram of the excitation and recombination processes that can result in photoluminescence.

to as Rayleigh scattering, the incident and resulting radiation have the same energy. In the case of an inelastically scattered photon (Raman scattering), there is a net energy difference between the incident and resulting radiation. If the net change of energy is positive, then the resulting photon has a higher frequency than the incident light and the shift is known as an anti-Stokes shift. If however, the net change is negative, then the resulting photon has a lower frequency than the incident light and the shift is termed a Stokes shift.

Rayleigh scattering is the most intense of these processes and results in re-emitted light which is about three orders of magnitude less in intensity than the incident excitation. In comparison, Raman scattered light is usually eight to twelve orders of magnitude less in intensity than that of the incident excitation. Comparing the Raman Stokes and anti-Stokes shifts, the Stokes shift results in more intense emission at room temperature since more initial states are at the ground state rather than at a vibrationally excited state. With changes in temperature, the overall system experiences a change in the population of vibrationally excited states; lower temperatures lead to fewer phonons in the lattice and more intense Stokes Raman lines. In fact, it is possible to measure the temperature of the specimen to within 5 K by measuring the intensities of both the Stokes and anti-Stokes Raman lines [88].

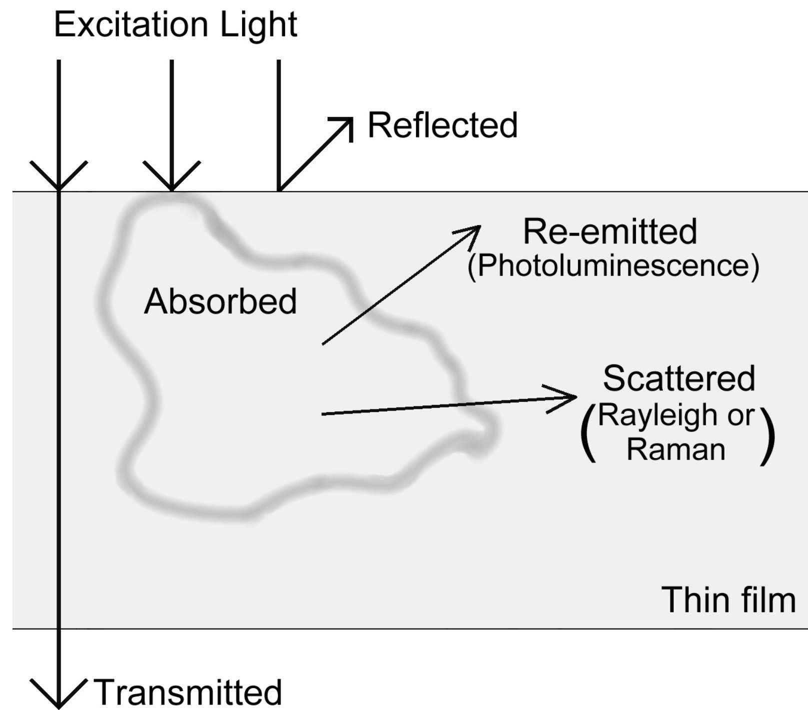

Figure 2.4: Interaction between light and matter.

A disadvantage of Raman spectroscopy is the low signal strength of Raman scattering. Fluorescence emission is six to eight orders of magnitude stronger than that of Raman scattering [87]. If a Raman shift occurs in the same region of the spectrum as a fluorescence emission, the Raman signal will not be detectable. This can be overcome by changing the wavelength of the excitation source to either a UV or near-IR excitation. Changing the excitation wavelength can also be useful to probe different depths of material since the absorption coefficient of a material is dependent upon the wavelength of light. Another approach to avoid problems associated with fluorescence is to take advantage of the photobleaching effect. Some fluorescing materials will breakdown with a sufficiently long time under excitation causing a decrease in the fluorescence intensity. By allowing the material to photobleach, Raman scattering that would otherwise be undetectable can be observed.

Although Raman shifts are occasionally reported in units of energy (eV) or frequency (Hz), the most commonly used units are wavenumbers (cm^{-1}). Typically relative wavenumbers are used; the relative wavenumber of a Raman band is the difference in absolute wavenumbers of the Raman shift and the excitation source. In order to find the absolute wavenumber of a quanta, one simply takes the inverse of its wavelength.

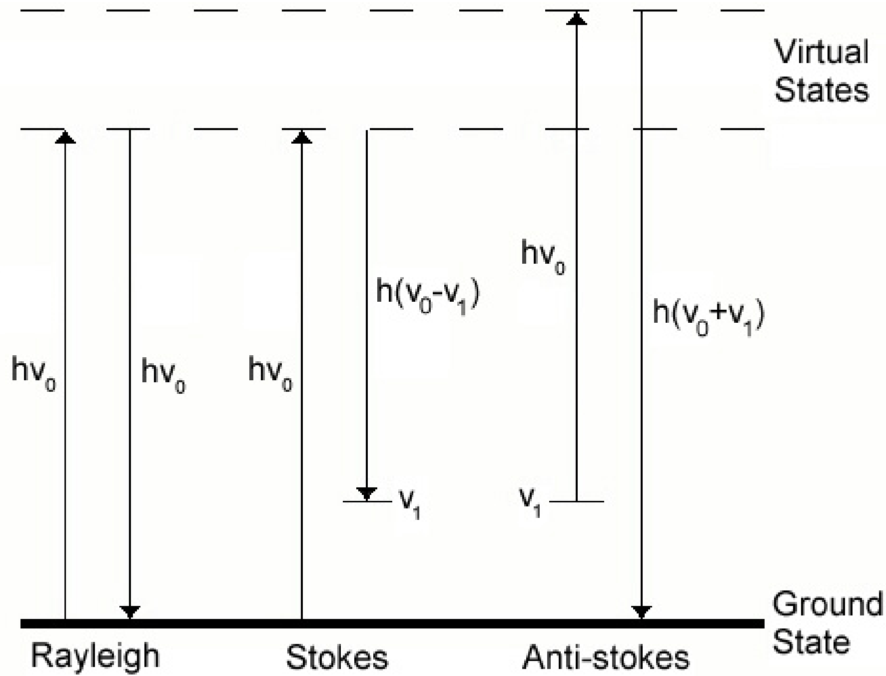

Figure 2.5: Energy model of the Raman effect.

For a Raman spectroscopy system there are a few key components required, a monochromatic light source (e.g., a laser), a set of collection optics, a means for dispersing the scattered light (e.g., a monochromator), and a light detector (e.g., a charge-coupled device (CCD) camera). The light source is typically a continuous wave laser in the visible region of the spectrum. Care should be taken when choosing the specific wavelength of the excitation laser. Both PL emission and the fact that the Raman scattering cross section varies as the fourth power of the excitation frequency must be considered [89]. This implies that for a constant laser power, the Raman spectra will increase in intensity as the wavelength of the excitation source becomes shorter.

A method of eliminating the high intensity Rayleigh scattering is also desirable, in order to achieve a high signal to noise ratio. This can be accomplished with the use of multiple monochromators or optical filters, such as notch type (transmits both Stokes and anti-Stokes scattering), longpass edge type (transmits only Stokes scattering), or shortpass edge type (transmits only anti-Stokes scattering).

2.5 Confocal Microscopy

The confocal microscope, invented in 1957, requires two key components in order to produce an image [90]. First, a diffraction limited excitation spot that can be scanned across the specimen and second, a way to collect the re-emitted light from the specimen and focus it onto a pinhole aperture. Light that passes through the pinhole can then be sent to a photosensitive device for analysis. As seen in Fig. 2.6, the advantage of using a confocal pinhole, as opposed to a conventional far-field microscope, is that light emitting from positions outside of the focal plane is rejected, thus achieving a small depth of field. In addition to the vast improvement in depth resolution as compared to a standard microscope, there is some improvement in the lateral resolution as well.

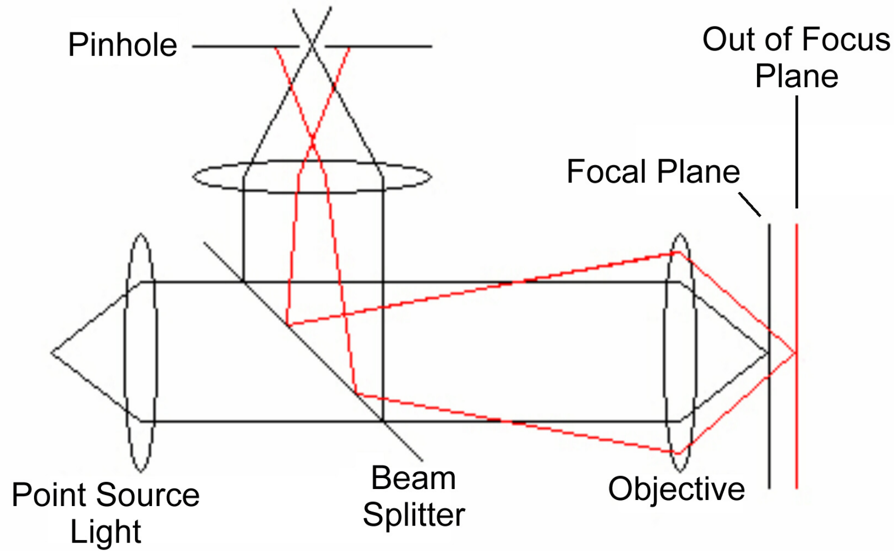

Figure 2.6: Diagram showing a confocal setup where rays from the focal plane pass through the pinhole but rays from other planes are blocked.

The theoretical depth resolution for an infinitely small aperture is given by

$$d_z = \frac{0.45\lambda}{n(1 - cos\theta_o)} \approx \frac{0.90\lambda}{NA^2}, \tag{2.3}$$

where λ is the excitation wavelength, n is the index of refraction of the medium between the objective and sample (assumed to have a value of 1 for air), θ_o is the half angle of the objective, and NA is the numerical aperture of the objective. The actual system resolution will be limited by the finite pinhole size as well as the incoherent Raman or fluorescent signal.

To find the actual resolution of a complete confocal Raman system, a technique is used that

measures the intensity of the 520 cm^{-1} Si peak as a function of z focal location [91, 92]. Starting with the focal point 10 μm above the Si surface, the microscope is incrementally moved to a focal point 10 μm below the surface, recording Raman spectra along the way. The full width at half maximum (FWHM) of the intensity vs. focal point z distance gives a good approximation of the depth resolution.

In a conventional microscope in air, the maximum lateral resolution is $2\lambda/3$, while the maximum lateral resolution for a confocal microscope is $\lambda/2$.

Chapter 3

Experimental

As previously stated, the objective of the present study was to investigate the effects of implanted lanthanoid ions on the photoluminescenece (PL) response of SiN_x films that contain Si nanocrystals. Specifically, films that contained one of three sizes of nanocrystals that, as a result of quantum confinement, had nominal PL emission in the red, green, and blue spectral regions, were considered. Following a baseline investigation of the as-grown films using both PL and Raman spectroscopy, the films were implanted with Ce, Nd, Eu, or Tb ions. Following implantation, the films were heat treated first at 500 °C and then 800 °C. PL spectroscopy was used to investigate the films after implantation, as well as after each heat treatment. The focus was on observing any intensity changes or spectral shifts in the PL emission associated with either the Si nanocrystals within the films or the implanted lanthanoid ions.

3.1 Synthesis of Si nanocrystals

Si rich SiN_x films provided by the Electronics and Telecommunication Research Institute in South Korea were used in this study. A plasma enhanced chemical vapor deposition (PECVD) process was used with Ar-diluted 10% silane (SiH_4) and nitrogen gas (N_2) with a purity greater than 99.9999% as reactant gas sources. Growth of 200 nm thick films was carried out on p-type (100) crystalline Si wafers with the reactor temperature, pressure, and plasma power fixed at 250 °C, 0.5 Torr, and 5 W, respectively. By controlling the flow rate of both reactant gases, the growth rate and stoichiometry of the resulting film could be controlled, which meant that the size of the nanocrystals within the SiN_x film could be tailored. Conditions were chosen to produce a set of films which contained "large", "medium", and "small" nanocrystals which would yield nominal emissions in the "red",

"green", and "blue" spectral regions. Flow rates of the N_2 and SiH_4 ranged from 500 to 1800 sccm and 4 to 12 sccm, respectively. After growth of the Si-rich SiN_x film using PECVD, no additional processing (i.e., heat treatment) was required. This is different from the usual method of creating Si nanocrystals in Si-rich SiO_x films, where post growth heat treatments as high as 1100 °C are required to cause the excess Si to segregate into nanocrystals [93]. Figure 3.1 is a schematic of the film and the implanted ion distrubtion as discussed in Section 3.2.

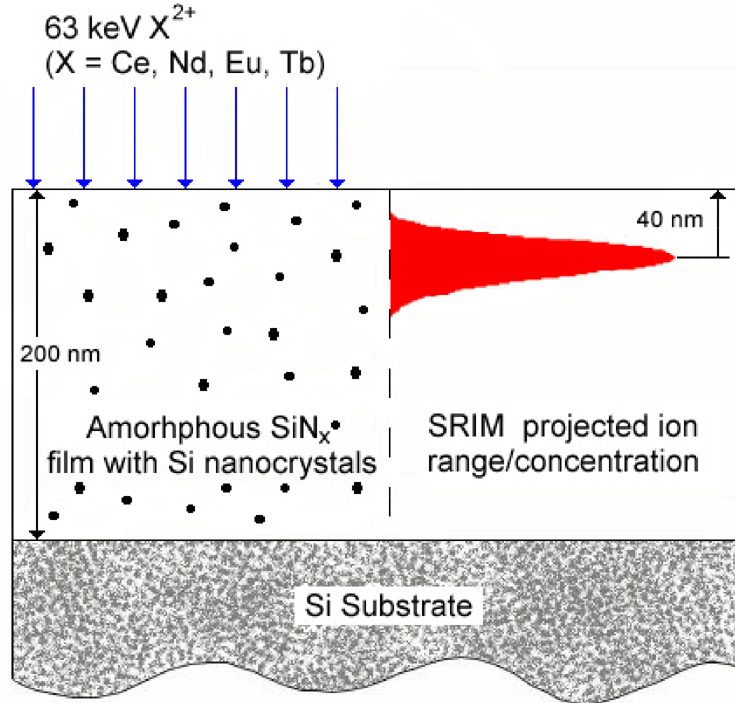

Figure 3.1: Schematic of the amorphous SiN_x film containing Si nanocrystals on a Si substrate.

High-resolution transmission electron microscopy (HRTEM) measurements on a set of films previously prepared under the same conditions as those of the present study indicated that the particles were crystalline in nature [51]. Furthermore, it was found in the previous study that the nominal emission from the nanocrystals produced fit the expression $E_{nanocrystal}(eV) = 1.16 + 11.8/d^2$, where d is the size of the nanocrystals in nm. As d approaches infinity, as in the case of bulk Si, $E_{nanocrystal}$ goes to 1.16 eV as compared to the band-gap of bulk Si of 1.12 eV. Based on the photoluminescence emission measured in the present study (and discussed in Section 4.1.1) the above relationship inferred that the large, medium, and small nanocrystals had average diameters of 3.9, 3.0, and 2.6 nm, respectively. In addition to the films containing the Si nanocrystals, stoichiometric Si_3N_4 specimens

were used as a control.

A second set of films were grown with the same experimental parameters, using fused silica (SiO_2) as the substrate instead of crystalline Si. These films were created specifically to aid in the investigation of the Raman scattering from the Si nanocrystals. Further details and discussion will be provided in Section 4.1.2, but it was found that Raman bands from the Si substrate dominated the observed spectrum.

3.2 Lanthanoid Ion Implantation

All ion implantations were performed at the Ion Beam Materials Laboratory at Los Alamos National Laboratory. Specimens were implanted at room temperature with one of four lanthanoid ion species (Ce^{2+}, Nd^{2+}, Eu^{2+}, or Tb^{2+}) with an energy of 63 keV and a fluence of 1×10^{15} ions/cm^2. Calculations using SRIM2006 software predicted the average projected depth of each ion species to be approximately 40 nm [94]. In order to remove implantation damage, two heat treatment cycles of 30 minutes each in a N_2 environment were performed on the implanted specimens; the first cycle was at 500 °C and the second at 800 °C. Photoluminescence and Raman measurements were conducted prior to implantation, after implantation, after the 500 °C heat treatment, and again after the 800 °C heat treatment. Based on the PL enhancement observed for films implanted with Ce ions in this initial investigation, it was decided to focus specifically on Ce^{3+} and to investigate the effects of ion concentration. In this follow up study, implantation was again carried out at room temperature with 63 keV ions and fluences of 3×10^{19}, 5×10^{20}, and 1×10^{26} ions/cm^2.

3.3 Instrumentation

There were two different instruments available to conduct the photoluminescence (PL) investigations. The first was a conventional far-field PL configuration using either the 3.53 eV (351 nm) line from an Ar ion laser or the 3.82 eV (325 nm) line from a HeCd laser as the excitation source. Emitted light was dispersed by a 0.5 m monochromator using a 2400 groove/mm grating and detected by a LN_2-cooled charge coupled device (CCD) camera. With the use of a continuous flow cryostat, the specimen temperature could be varied between 4.2 and 300 K. More details and specifications of this particular system can be found elsewhere [95].

The second system was a commercially available combination confocal microscope and scanning near-field optical microscope (SNOM) (WITec, GmbH). For the purpose of this study, only the

confocal microscopy mode of the system was employed. Confocal PL measurements were carried out using the 3.82 eV (325 nm) line from a HeCd laser, while a 2.33 eV (532 nm) frequency doubled Nd:YAG laser was used to perform Raman spectroscopy. A schematic of the system components and beam path is shown in Fig. 3.2. The following provides details and specifications of each component of the overall system. Checklists for the system can be found in Appendix A.

3.3.1 Laser

For the PL experiments a continuous wave Kimmon IK3151R-E helium cadmium (HeCd) laser operating at an energy of 3.82 eV (325 nm) was used. The beam output (TEM00) was rated at a maximum power of 17 mW. The laser was coupled to the microscope via a singlemode UV optical fiber with a core diameter of 2 μm. At the output end of the fiber, the maximum laser power was measured to be about 2.0 mW. For the Raman experiments a continuous wave frequency doubled Nd:YAG laser operating at an energy of 2.33 eV (532 nm) was used. Laser coupling with the microscope was achieved with a polarization maintaining optical fiber with a core diameter of 3.5 μm. At the output end of the fiber the maximum laser power was measured to be about 8 mW. Power output from each of the fibers could be varied by adjusting a micrometer screw integrated into the respective fiber couplers.

3.3.2 Objectives

In the WITec system, standard microscope objectives were mounted on an upright objective turret. One of the objective positions had the mounting armature for either an atomic force microscopy (AFM) or SNOM cantilever, as well as the inertial drive to control its movement. This allows different types of measurements to be made, either confocal, AFM, and/or SNOM, on the same region of the specimen. There was also the ability to mount one objective in an inverted position beneath the specimen stage, allowing for collection in transmission mode. When using the Nd:YAG laser, a 100x/0.9NA Nikon objective capable of producing an approximate spot size of 0.4 μm was used. The HeCd laser light required an objective that was capable of transmitting UV light, which required using a 10x/0.2NA Zeiss Ultrafluar objective with a theoretical spot size of 1.0 μm.

3.3.3 Confocal pin-hole

Scattered or re-emitted light that was collected by the objective was focused onto the end of a UV-visible multimode optical fiber, which acted as the confocal pin-hole. A total of three different

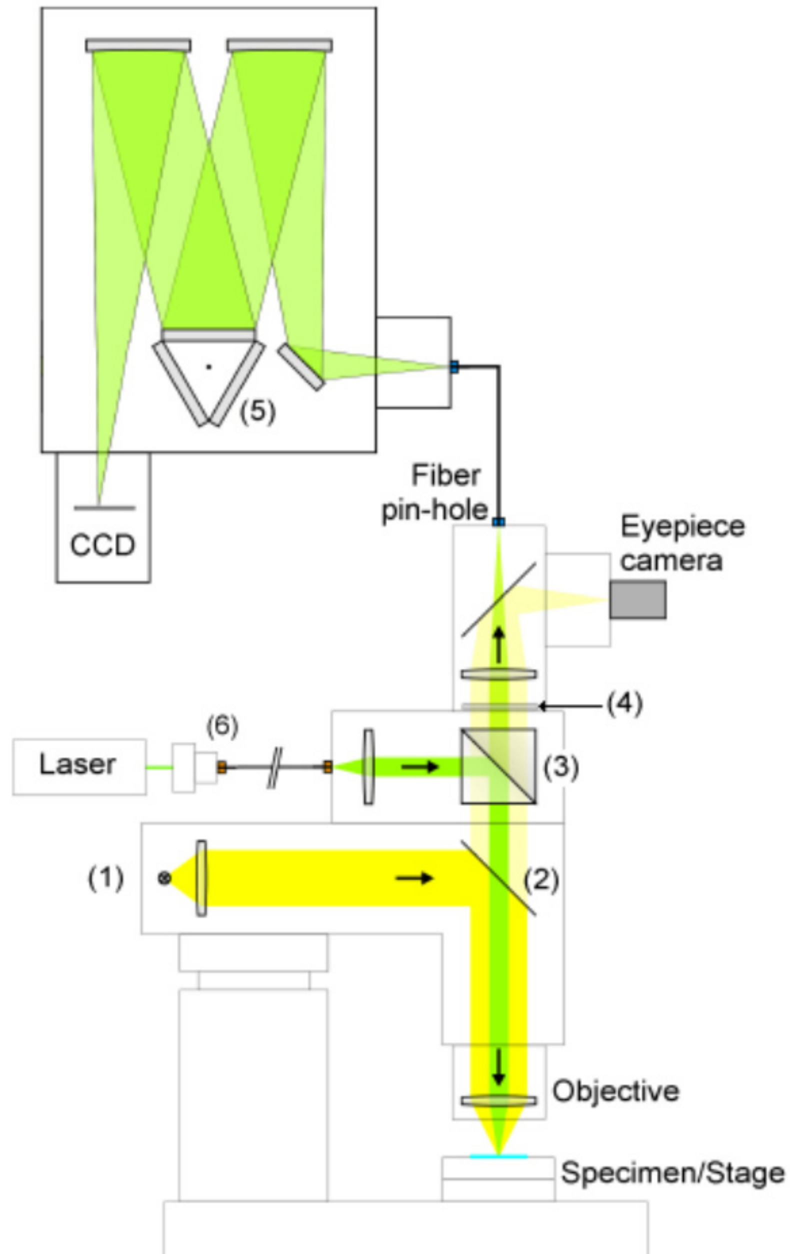

Figure 3.2: Schematic showing the components and beam path of the WITec Alpha SNOM configured in a reflection confocal mode, and the monochromator and CCD. (1) is a white light source, (2) is a 50:50 beamsplitter, (3) is a holographic bandpass filter, (4) is the laser blocking filter, (5) is a rotating turret holding three gratings, and (6) is the fiber coupler and a single mode fiber. (Modified from the Alpha SNOM Operating Manual.)

fibers were available, with core diameters measuring 100, 50, and 25 μm. Decreasing pin-hole (core diameter) size resulted in an increase in z-resolution, but at the cost of signal throughput. According to Eq. (2.3) the theoretical confocal depth resolution using the 100x objective and 532 nm Nd:YAG laser was 585 nm. The actual depth resolution of our system as measured by the technique described in Section 2.5 and shown in Fig. 3.3 was 1.21, 0.82, and 0.62 μm for 100, 50, and 25 μm diameter fibers, respectively. Only the 100 μm fiber was used in this study in order to maximize the signal intensity.

3.3.4 Monochromator/Detector

Light passing through the confocal pin-hole was directed by the optical fiber to a 0.3 m Acton monochromator. Light was dispersed with either a 150, 600, or 1800 gr/mm diffraction grating, each holographic blazed at 500 nm. All gratings were attached to a rotating turret, allowing for the selection of the grating without opening the monochromator. Light was detected with a 1024 x 128 pixel, thermoelectrically cooled ($-73\,^{\circ}$C) charge coupled device (CCD) from Andor Technology. The band pass of a monochromator is given by $BP = Wd/f$, where W is the larger of the entrance width or CCD pixel size, d is the distance between grates, and f is the monochromator focal length. Resolutions for the 0.3 m Acton monochromator using the 150, 600, and 1800 gr/mm gratings are 0.578, 0.144, and 0.0481 nm (23, 5.8, and 1.9 cm^{-1}), respectively.

3.4 Procedure for the Photoluminescence and Raman Experiments

The procedures for the photoluminescence (PL) and Raman experiments are essentially identical, with the only major differences being the excitation source, the spectral region examined, and the units used for analysis. For the PL measurements, the 3.82 eV (325 nm) line of the HeCd laser was used and the energy of the emitted light was measured. For the Raman measurements, the 2.33 eV (532 nm) line of the Nd:YAG laser was used and the relative wavenumber shift of the scattered light was measured.

A specimen was placed on a glass slide which was then placed on the stage under the microscope objective. For the Raman measurements, the angle of incidence was normal to the specimen surface. For the PL measurements, the specimen was tilted approximately 10°, in order to reduce the intensity of the laser plasma lines. Using the whitelight source of the microscope, the objective was moved

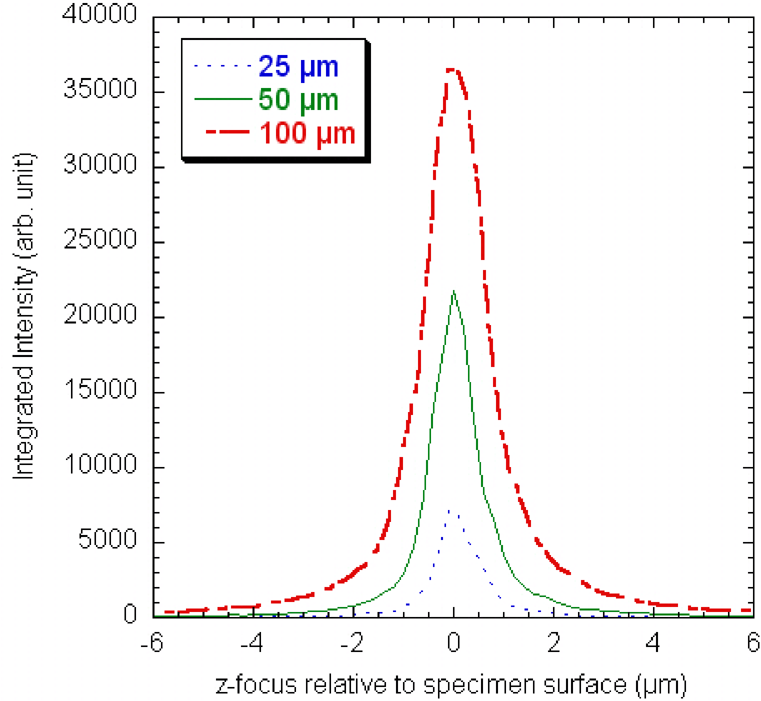

Figure 3.3: Integrated intensity of the 520 cm^{-1} Si peak as a function of focus distance with respect to the surface (positive value is above the surface). System z-resolution is given by the FWHM. Other than fiber diameter, experimental parameters remained constant implying the decrease in the integrated intensity is the result of decreased signal throughput.

relative to the specimen in order to focus on its surface. Once in focus, the whitelight source was blocked by removing the 50:50 beam splitter that directs it toward the specimen. After verifying that the micrometer screw on the laser coupler was at the desired setting, the laser shutter was opened to allow laser light to enter the microscope. Care was taken to start with a relatively low laser power and slowly increase it as needed, since large power densities are capable of changing the structure and altering other properties of the specimen. After verifying that the collimation of the laser was such that the beam was parallel within the microscope optics, the objective was again focused in order to achieve the smallest laser spot size. At this point, the laser was focused on the surface of the specimen and the pushrod of the sliding prism was pulled outward to direct the light from the eyepiece camera to the optical fiber acting as the confocal pinhole.

For the PL measurements the 150 gr/mm grating was used, while for the Raman measurements either the 600 or 1800 gr/mm grating was used depending on the required resolution. Once the proper grating was selected and positioned in place by the motor driven rotating turret, measurements were

ready to be taken. The FOCUS SPECTRUM function of the WITec ScanCtrl Spectroscopy Plus software was first used to verify that the integration time will not lead to damage of the CCD. The CCD is capable of collecting a total of 65,000 counts per column of pixels during a single integration. Once a proper integration time was established then final measurements could be made using the SINGLE SPECTRUM function of the ScanCtrl Spectroscopy Plus software. For each collected spectra, the cosmic ray removal box was selected to eliminate any cosmic ray-like features and the average box was also selected so that the output was the average of a user defined number of collected spectra.

3.5 Probing Depth

From the Beer-Lambert-Bouguer law, the ratio of light intensity at depth z under the surface to the incident light intensity is given as $I(z)/I_o = exp(-\alpha z)$, where α is the absorption coefficient for the particular wavelength of interest. The absorption depth is given by the distance in the material in which 63.2 % of the incident light is absorbed (i.e., $I(z)/I_o = 1/e$) [96]. This gives the absorption depth as the inverse of the coefficient of absorption. Since a back-scattered arrangment is used, scattered or re-emitted light must travel to a depth of z and then back through the same distance of material to reach the surface in order to be detected. This configuration means that the probing depth is given as $1/2\alpha$. Table 3.1 gives values for materials pertinent to this study. The absorption coefficient of SiN_x implies that the film will be essentially transparent to excitation from either the HeCd or Nd:YAG laser, allowing it to fully pass through the film to the substrate.

Table 3.1: Absorption coefficient and approximate probing depth of materials using 325 and 532 nm excitation

	$\lambda = 325$ nm		$\lambda = 532$ nm	
	α (cm^{-1})	Depth (nm)	α (cm^{-1})	Depth (nm)
Crystalline Si	1,225,000 [97]	4	6,680 [98]	750
Amorphous Si	—	—	∼60,000 [99]	80
Amorphous SiN_x	∼1,300 [100]	3,850	∼290 [100]	17,200

Chapter 4

Results and Discussion

This chapter presents the results obtained on the effect of nanocrystal size and the effects resulting from implanted lanthanoid ions on the photoluminescence of the Si nanocrystals. In the first section, investigations of the as-grown films (200 nm thick amorphous SiN_x films containing Si nanocrystals), first with confocal photoluminescence (PL) spectroscopy and then with confocal Raman spectroscopy are reported. In the next section results of the investigation on the effect of lanthanoid ions implanted into the films are reported. The third section focuses specifically on Ce ion implantation and the effect of dopant (ion) concentration. Finally, possible mechanisms responsible for the apparent energy transfer from the Ce ions to the Si nanocrystals are discussed. All of the spectra presented are typical and have not been filtered, smoothed, or corrected for the detector response. Stoichiometric Si_3N_4 films were used as a control.

4.1 As-Grown Films

4.1.1 Photoluminescence response

Photoluminescence (PL) spectroscopy performed at room temperature showed that the emission from the as-grown SiN_x films containing the Si nanocrystals blue-shifted with decreasing Si nanocrystal (nc-Si) size. The results for films grown on Si substrates are shown in Fig. 4.1. As discussed in Section 3.1, the relationship between nominal emission energy and nanocrystal size was found to be linear and to agree with the expression put forth by Kim et al. [51]. Using this expression and the measured emission energies of 1.97, 2.48, and 2.85 eV as shown in Fig. 4.1, infers nc-Si sizes of 3.9, 3.0, and 2.6 nm respectively.

All emissions were broad, with a FWHM of 660, 870, and 540 meV for the large, medium, and

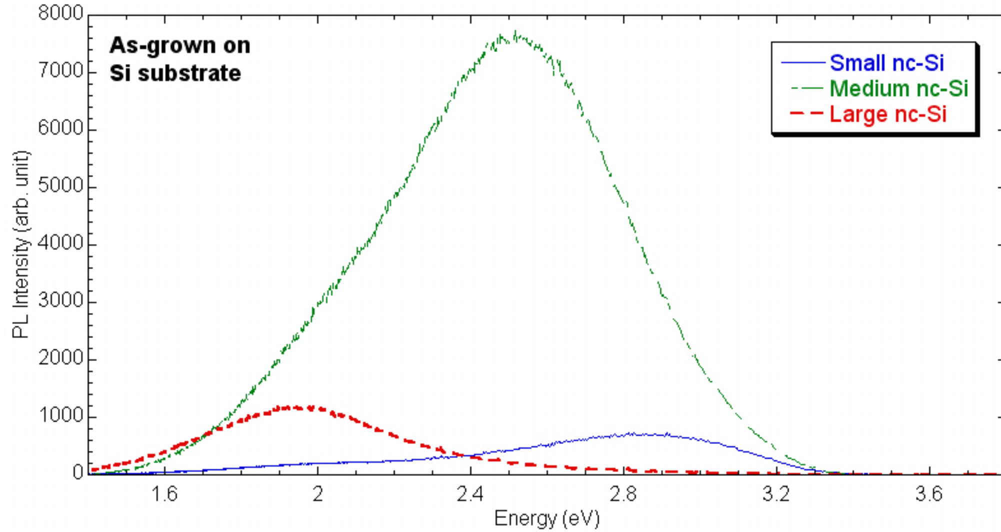

Figure 4.1: Room temperature confocal PL spectra of 200 nm thick Si:SiN$_x$ films grown on Si. The nominal emission of the nc-Si went from red to green to blue as nc-Si decreased. Spectra are not normalized.

small nc-Si, respectively. The relatively large bandwidth of the PL emission is typically attributed to inhomogeneous broadening due to variations in the size and shape of the nanocrystals. Films previously prepared under the same growth conditions had a standard deviation in size of 0.28 nm [51]. Other factors that can lead to broadening include interactions with phonons, multiple localized states in a single nanocrystal, and stress in the core of the nanocrystal [53]. Brun et al. [101] investigated inhomogeneous broadening of the PL emission of CdTe quantum dots using low temperature far-field and near-field PL. In the far-field, the PL emission had a FWHM of 130 meV, while the near-field PL showed that the FWHM of a single quantum dot was no greater than the system resolution of 0.33 meV.

PL intensity observed from the film containing the medium nanocrystals was about 9-fold more intense than the film with large nanocrystals and about 6-fold more intense than the film with small nanocrystals. Smaller nanocrystals are known to have higher oscillator strengths than larger ones, resulting in more intense PL emission from the smaller nanocrystals. It is unclear why the films containing the small nanocrystals are less intense than those containing the medium nanocrystals. The effect observed was repeatable based on a second set of films created under similar conditions which contained the same nanocrystal sizes.

While future integration into optoelectronic devices would likely see the SiN_x films deposited on Si substrates, as is the case with Fig. 4.1, similar PL response was observed when a SiO_2 substrate

was used. As shown in Fig. 4.2. Emission energies of 1.85, 2.10, 2.26, and 2.73 eV infers nc-Si sizes of 4.1, 3.5, 3.3, and 2.7 nm, respectively.

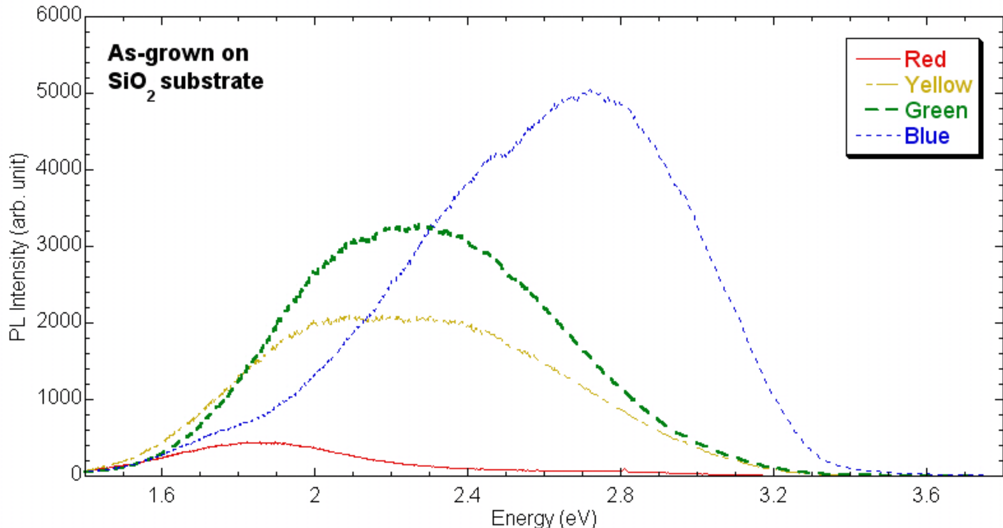

Figure 4.2: Room temperature confocal PL spectra of 200 nm thick Si:SiN_x films grown on SiO_2. The nominal emission of the nc-Si went from red to yellow to green to blue as nc-Si decreased.

A preliminary investigation into the temperature dependence of the PL response was conducted from room temperature down to liquid N_2 temperature (from 300 to 77 K) using a conventional far-field PL system. Results are not presented as the signals are relatively weak due to the far field setup and the presence of many plasma lines from the Ar ion laser. Consistent with the observations reported in the literature, there was an increase in PL intensity when temperature was reduced from 300 to ∼100 K at which the intensity leveled off until reaching the minimum temperature of 77 K [102, 103]. The intensity increase was approximately 25% and there was no observable change in the spectral center or shape. Brongersma et al. [102] attributed the temperature dependence of the PL intensity to the recombination of strongly localized excitons in the Si nanocrystals.

4.1.2 Raman response

The results obtained on the Raman response of the as-grown SiN_x films containing the Si nanocrystals grown on Si substrates are divided into two regions; from 0 to 1000 cm^{-1}, which contain the response from the Si nanocrystals, and from 1800 to 3600 cm^{-1}, which contains the related to Si-H bonds and N-H bonds. The later region involving H from the silane (SiH_4) reactant gas is presented first.

Si-H and N-H bonds

In Raman studies of bulk Si containing H, the Si-H related spectrum is usually divided into lower-frequency and higher-frequency regions that span from 1900 to 2050 cm^{-1} and from 2050 to 2300 cm^{-1}, respectively. The modes in the lower frequency region are assigned to hydrided multi-vacancies, while modes in the higher-frequency region are assigned to either hydrided single vacancies or SiH_x on (100) surfaces [104, 105]. Specifically the stretching modes of Si-H, Si-H_2, Si-H_3, and Si-H_4 are expected at approximately 2120, 2130, 2180, and 2240 cm^{-1}, respectively [104–106].

Figure 4.3 shows the Si-H band from the as-grown film with the small nanocrystals is centered at 2185 cm^{-1}, while the film with medium nanocrystals is centered at 2195 cm^{-1}. The broadness of the Si-H band for both films is the result of the superposition of multiple peaks, specifically the Si-H, Si-H_2, Si-H_3, and Si-H_4 stretching modes. Fitting the Si-H bands with four Lorentzian peaks produced deconvolved peaks that agreed with the expected locations of the Si-H, Si-H_2, Si-H_3, and Si-H_4 modes and implied that Si-H_3 is the most dominant mode in each film. Comparing relative intensities of the Si-H band for the two films, it is seen that the film with the medium Si nanocrystals is 3.5 times as intense as that of the film with the small Si nanocrystals. This is consistent with the higher SiH_4 flow rates used to increase the Si nanocrystal size within the SiN_x film. A higher flow rate of SiH_4 implies that there are more SiH_x (x=1, 2, or 3) species present in the gas phase that can subsequently incorporate into the growing SiN_x film. This observation of a more intense Si-H band with increasing SiH_4 flow rate is consistent with the observations reported using Fourier transform infrared spectroscopy (FTIR) [107].

For the case of the N-H band shown in Fig. 4.3, the film with the small nanocrystals shows the band centered at 3362 cm^{-1} while for the film with medium nanocrystals it is at 3370 cm^{-1}. These locations are in agreement with the theoretical N-H stretching mode at 3350 cm^{-1}, which typically appears as a broad band and has been observed to vary between 3000 and 4000 cm^{-1} depending upon the specific environment [108, 109]. N-H_2 bonds are also Raman active, showing two distinct spectral peaks, located between 3300-3325 and 3360-3375 cm^{-1}, and associated with symmetric and asymmetric stretching, respectively [110]. The observed N-H band for the small nanocrystals was nearly 2.5 times more intense than that for the medium nanocrystals. A plausible explanation for this is as follows. Alexandrov et al. [111] have reported that N-H bond formation takes place at the film surface as a result of surface rearrangement of adsorbed SiH_x species and N ions. They also showed that film growth rates increase with increasing flow rates of SiH_4, which would provide less time for surface rearrangement and thus decrease the likelihood of N-H bond formation. This

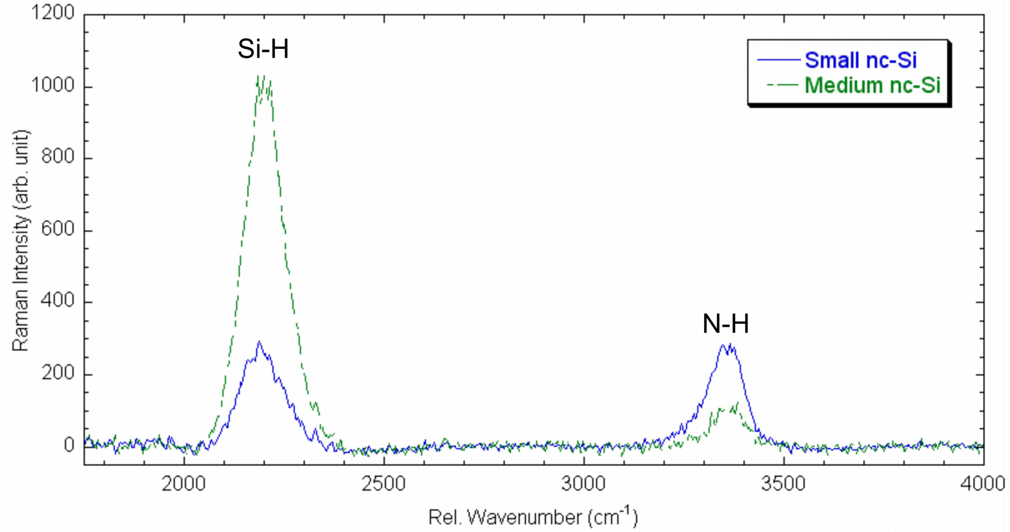

Figure 4.3: Room temperature confocal Raman spectra of 200 nm thick Si:SiN$_x$ films grown on Si that contain small and medium Si nanocrystals. Both spectra have been normalized using the 3TO Si peak at 1450 cm^{-1}.

implies that films with the larger Si nanocrystals, due to higher SiH_4 flow rate used in their growth, would contain fewer N-H bonds.

The presence of Si-H and N-H bonds is known to play a role in the observed PL emission since it has been widely observed that H passivates non-radiative and defect centers at the matrix/Si nanocrystal interface [72, 112, 113]. If H is not present, dangling bonds at the surface of the Si nanocrystals would act as non-radiative centers and thus provide a competing recombination mechanism to the radiative recombination of excitons.

For the film containing large nanocrystals and the stoichiometric Si_3N_4 film (containing no nanocrystals) PL emission was observed in the same spectral region as the H-related Raman bands. Both of these films had an evident Si-H band superimposed on the PL peak, but no clear evidence of the N-H band. The absence of the N-H band for the film with the large nanocrystals and the stoiciometric films is consistent with the previous discussion on the formation of N-H bonds.

Si-Si and Si-N bonds

The lower frequency region of the Raman spectrum is expected to contain peaks related to the Si nanocrystals. Figure 4.4 shows the Raman spectrum obtained for an as-grown SiN_x film containing the medium Si nanocrystals and a bulk crystalline Si substrate. The two spectra appear nearly identical. The strong but narrow Si peak near 520 cm^{-1} dominates the spectrum, followed in

intensity by the 2TO Si peak at 960 cm^{-1} and the 2TA Si peak at 303 cm^{-1}. Other less intense peaks are visible near 230, 430, 620, 670, and 830 cm^{-1} and are all related to multi-phonon modes of bulk crystalline Si [22].

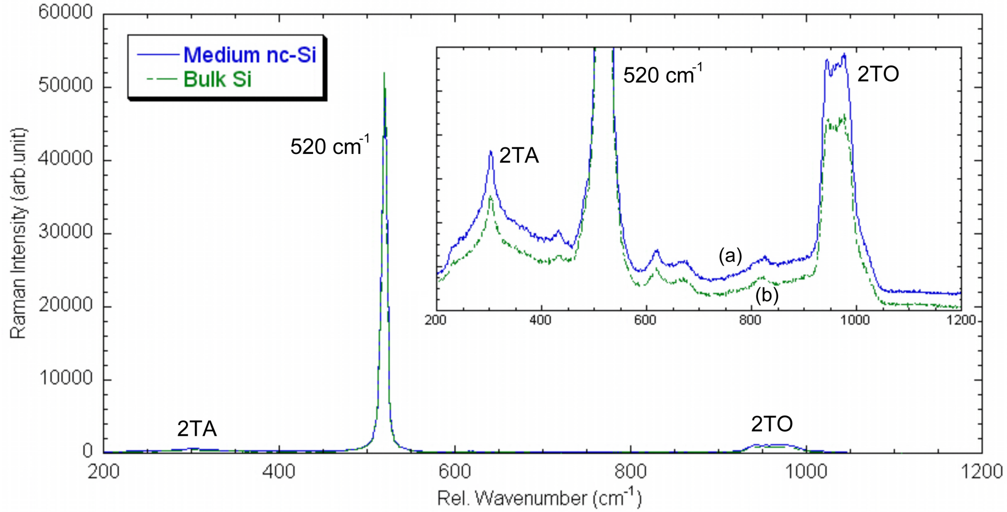

Figure 4.4: Room temperature confocal Raman spectra of (a) 200 nm thick amorphous SiN_x film grown on bulk Si that contains medium Si nanocrystals and (b) bulk crystalline Si. The inset shows structure of the lower intensity peaks and spectra (a) has been shifted up for clarity. All spectra have been normalized with respect to the 520 cm^{-1} peak.

As the size of the Si nanocrystals decrease from that of a bulk single crystal, it is expected that the 520 cm^{-1} peak would both shift to a lower frequency and broaden [114]. Iqbal et al. [114] observed that polycrystalline Si, with crystallite sizes of ∼4.7 nm, exhibited the peak at 513.5 cm^{-1} broadened to a FWHM of 13 cm^{-1} compared to that of FWHM of bulk Si which was 5.5 cm^{-1}. The observation of other Si-Si modes, such as symmetric breathing (470-490 cm^{-1}), serpentine-bending (460-470 cm^{-1}), and scissor-bending (450-465 cm^{-1}), as well as Si-N modes such as symmetric stretching (830 cm^{-1}) and asymmetric stretching (420-445 cm^{-1}) would likely be obersved for the film containing the nanocrystals [115].

So as to illustrate the differences in the Raman spectrum for single crystal Si and for Si containing an increasing amount of amorphous structure, bulk Si was implanted with Ar at increasing fluences and the resulting Raman spectra obtained are shown in Fig. 4.5. Each specimen started as bulk crystalline Si and as the fluence of the Ar ions increased, the amount of lattice damage increased until a fully amorphous layer was created at the highest fluence of 1×10^{15} ions/cm^2.

As the fluence increases, the intensity of the 520 cm^{-1} crystalline Si peak is seen to shift to lower

frequencies, indicating higher tensile stress. The 520 cm^{-1} peak and the 2TA and 2TO peaks of crystalline Si at 303 and 960 cm^{-1}, respectively, are all observed to continually decrease in intensity and eventually disappear with increasing Ar ion fluence. This decrease and disappearance of the peaks associated with crystalline Si implies that the bulk Si specimens are becoming less crystalline with increasing fluence. Further supporting this is the appearance of a broad amorphous Si band that first appears as a shoulder on the 520 cm^{-1} peak and eventually shifts to 465 cm^{-1} where it is the only peak observed for the specimen implanted with the highest fluence of 1×10^{15} ions/cm^2.

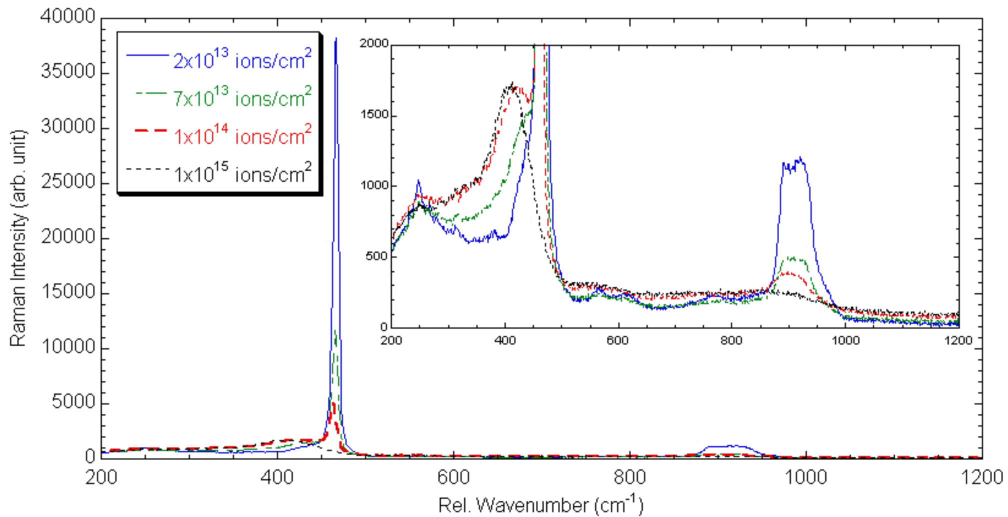

Figure 4.5: Confocal Raman spectra of bulk crystalline Si implanted with Ar at increasing fluences leading to an increasingly amorphous structure.

As discussed in Section 3.5, the absorption coefficient of SiN_x is sufficiently small that the 200 nm thick film of the present study is transparent to the excitation light of the Nd:YAG laser. Since the laser light can pass through the film with little intensity loss, the substrate is probed and the resulting signals overwhelm any signals originating from the SiN_x film. Longer integration times are not an option to observe signals from the film since the highest intensity measured in the spectra of Figure 4.4 is 52,000 counts and the CCD can achieve at most 65,000 counts before saturating.

In an attempt to observe Raman scattering from the Si nanocrystals, without the influence of the Si substrate signal, confocal Raman experiments were performed on 200 nm thick Si:SiN_x films that were grown on SiO_2. There were a total of four films that had nominal PL emissions in the blue, green, yellow, and red spectral regions. Figure 4.6 shows the Raman response of these films. The 532 nm excitation source induced a broad PL emission in both the yellow and red specimens, making the measurement of Raman signals in this spectral region difficult. As discussed previously,

for both the blue and green emitting films there were bands observed at 2180 and 3350 cm^{-1} that are associated with Si-H bonds and N-H bonds, respectively. Despite the presence of the PL, both the yellow and red specimens also had observable Si-H bands at 2180 cm^{-1}.

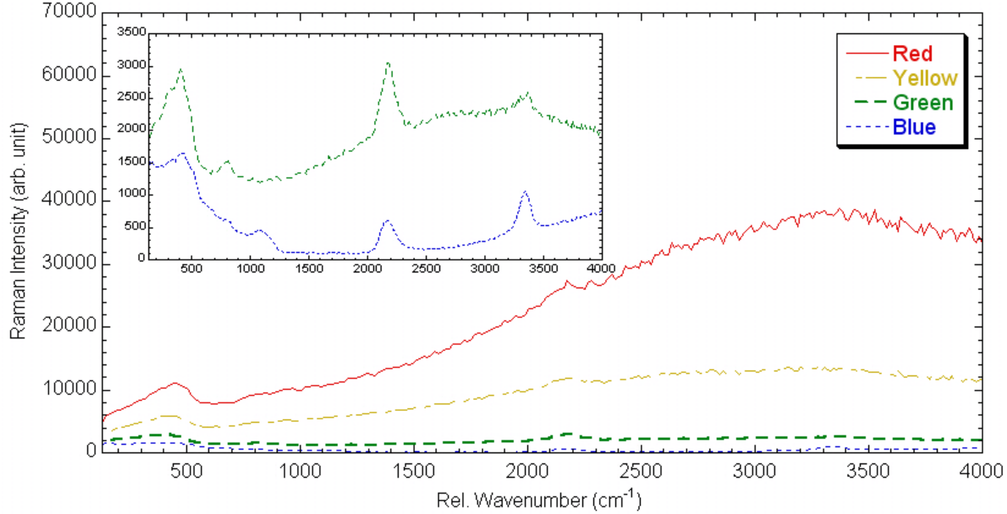

Figure 4.6: Room temperature confocal Raman spectra of 200 nm thick amorphous SiN_x films grown on SiO_2. Nominal PL emission of the nc-Si appeared in the red, yellow, green, and blue spectral regions as the nc-Si size decreased. Inset shows details of the blue and green emitting films.

In the low frequency region, only Raman bands associated with the SiO_2 substrate are observed; specifically these bands are near 440, 800, and 1060 cm^{-1}. The broad peak at 440 cm^{-1} is the result of the ω_1 mode of Si-O-Si symmetric stretching, the 800 cm^{-1} peak results from the ω_3 mode, and the 1060 cm^{-1} is related to the TO ω_4 mode [116]. Two commonly observed defect peaks associated with SiO_2 are at 490 and 610 cm^{-1}, which are related to symmetric stretching modes of four-fold and three-fold rings, respectively, of SiO_2 tetrahedra [117]. Although there is not a clear, distinct peak at 490 cm^{-1}, it might be evidenced as a broadening of the 440 cm^{-1} band.

Both choices of substrate materials, Si and SiO_2, resulted in Raman scattering from the nanocrystals not being detectable. Two potential techniques that have previously been used to overcome similar situations are: a) the inclusion of a reflective buffer layer between the substrate and film and b) the use of different polarization geometries. In the study of amorphous Si_3N_4 by Bandet et al. [118], a 200 nm thick layer of Al was deposited on the Si substrate prior to film growth. This layer is not Raman active and prevents laser light from reaching the substrate, and also helps to reflect scattered light toward the detector. Bandet et al. also created a film thicker than the probing depth

of the excitation source, but the signal increase was minimal and the thickness (2 μm) led to an intensity modulation due to interference. Volodin et al. [57] investigated Si nanocrystals formed in SiN_x films on Si(001) substrates and used polarization geometries to reduce the substrate signal. In a backscattering configuration only LO phonons are active; if both the excitation light and collected light are polarized in the (100) direction then scattering on LO phonons is prohibited. By combining these two schemes, in theory, no signal will result from the Si substrate. Since the Si nanocrystals in the study by Volodin et al. [57] were randomly oriented, scattering on LO phonons was allowed and thus Raman scattering was observed.

4.2 Lanthanide Ion Implantations

Based on the reported success of Er PL emission enhancement by implanting Er in SiN_x films containing Si nanocrystals [83, 84], a systematic investigation into the effect of implanting Ce, Nd, Eu, and Tb ions was conducted. This section presents the results of the Nd, Eu and Tb implantations, while Section 4.3.1 will focus specifically on the results of the Ce implantation.

In this initial baseline study, the effect of Si nanocrystal size on the PL response of amorphous Si rich SiN_x films that were implanted with a single lanthanide ion species was studied. All implantations were carried out at room temperature with 63 keV doubly charged ions at a fluence of 1×10^{15} ions/cm^2. Figure 4.7 shows the PL response of each Si nanocrystal size after the lanthanide ion implantation. Ce implantation in the films with the small and medium nanocrystals is the only implantation to show any PL intensity increase compared to that of the respective as-grown films. More details on the Ce implanted films will be provided in Section 4.3. Expected strong emissions from the lanthanide ions would be at approximately 1.17 eV for Nd, 2.02 eV for Eu, and 2.28 eV for Tb; there is no evidence of emissions originating from the implanted ions.

Ion implantation is known to induce damage that often results in the creation of non-radiative recombination centers and thus the post-implantation PL emission is greatly diminished. Post-implantation PL intensity of the Si nanocrystals, although less intense than as-grown, is still relatively strong. This would suggest that the Si nanocrystals structure and their interface with the matrix are largely unaffected by implantation damage. The presence of H could be one reason for the radiation damage tolerance since it provides the possibility of passivating newly created dangling bonds. The small size of the Si nanocrystals could also be a factor since small nanocrystals have a higher probability of dislocations cascading entirely through the nanocrystal [119].

To reduce implantation damage, the implanted films were heat treated for 30 minutes at 500 °C

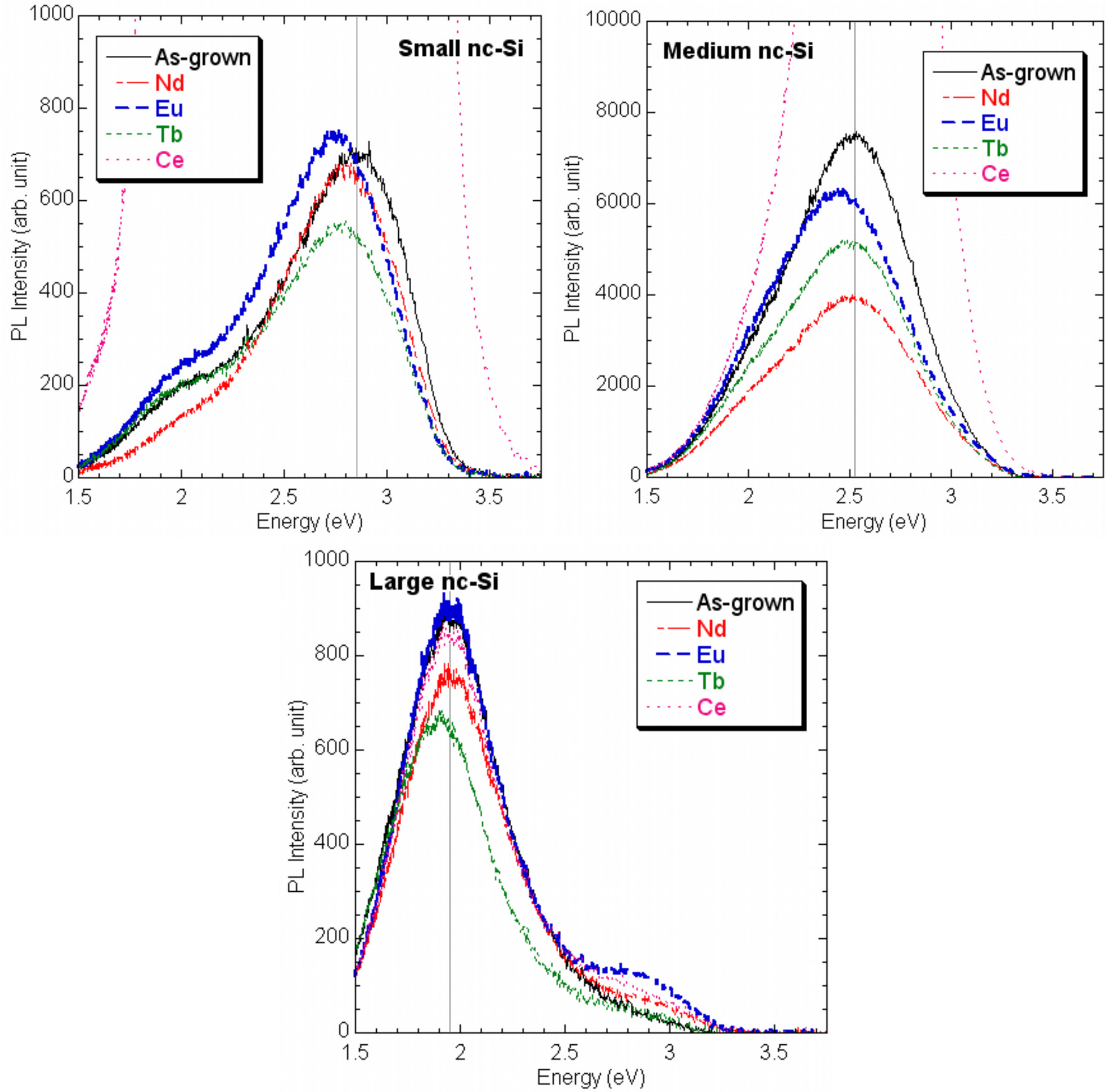

Figure 4.7: Room temperature confocal PL spectra of 200 nm thick amorphous SiN_x films grown on Si implanted with various lanthanide ions. Vertical lines show the approximate spectral centers of the as-grown films.(Note that the spectra from the Ce implanted small and medium Si nanocrystals is not fully shown as it is discussed further in Section 4.3).

under a flow of N_2 to prevent film oxidation. Little to no effect on nanocrystal size is expected for this time and temperature based on the results of 30 minute heat treatments on similar SiN_x films at 800 °C that showed no change in nanocrystal size [84]. Figure 4.8 shows the PL response of the implanted films heat treated at 500 °C for each Si nanocrystal size.

Comparing Figs. 4.7 and 4.8, the films containing small nanocrystals, especially those implanted with Eu, showed an increase in intensity, and a broadening that led to a red shift after the heat

treatment. Although the appearance of an Eu emission at 2.02 eV could explain the observed behavior of the Eu implanted film, the Nd and Tb implanted and heat treated films containing small Si nanocrystals showed the appearance of a new peak near 2.0 eV as well. The exact cause is unclear, but since all three of these ions showed similar behavior, there appears to be some mechanism other than lanthanide emission responsible for the new PL peak.

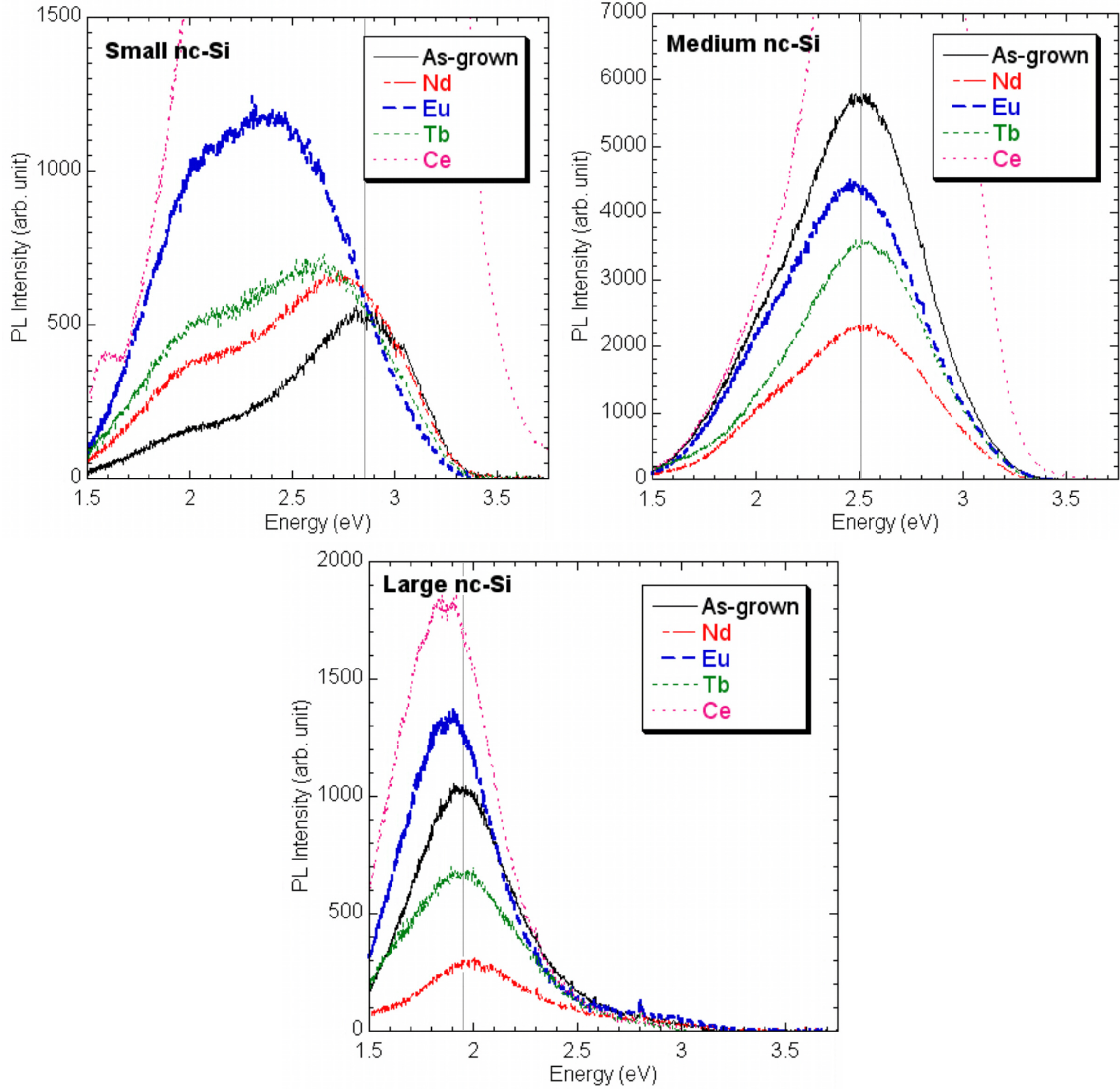

Figure 4.8: Room temperature confocal PL spectra of 200 nm thick amorphous SiN_x films grown on Si implanted with various lanthanide ions after the 500 °C heat treatment. Vertical lines show the approximate spectral centers of the as-grown films.

A second heat treatment at a higher temperature was conducted to investigate if any additional changes would occur. This second heat treatment was again performed for 30 minutes in a N_2

environment at an increased temperature of 800 °C. Figure 4.9 shows the PL response for the thin films after this final heat treatment.

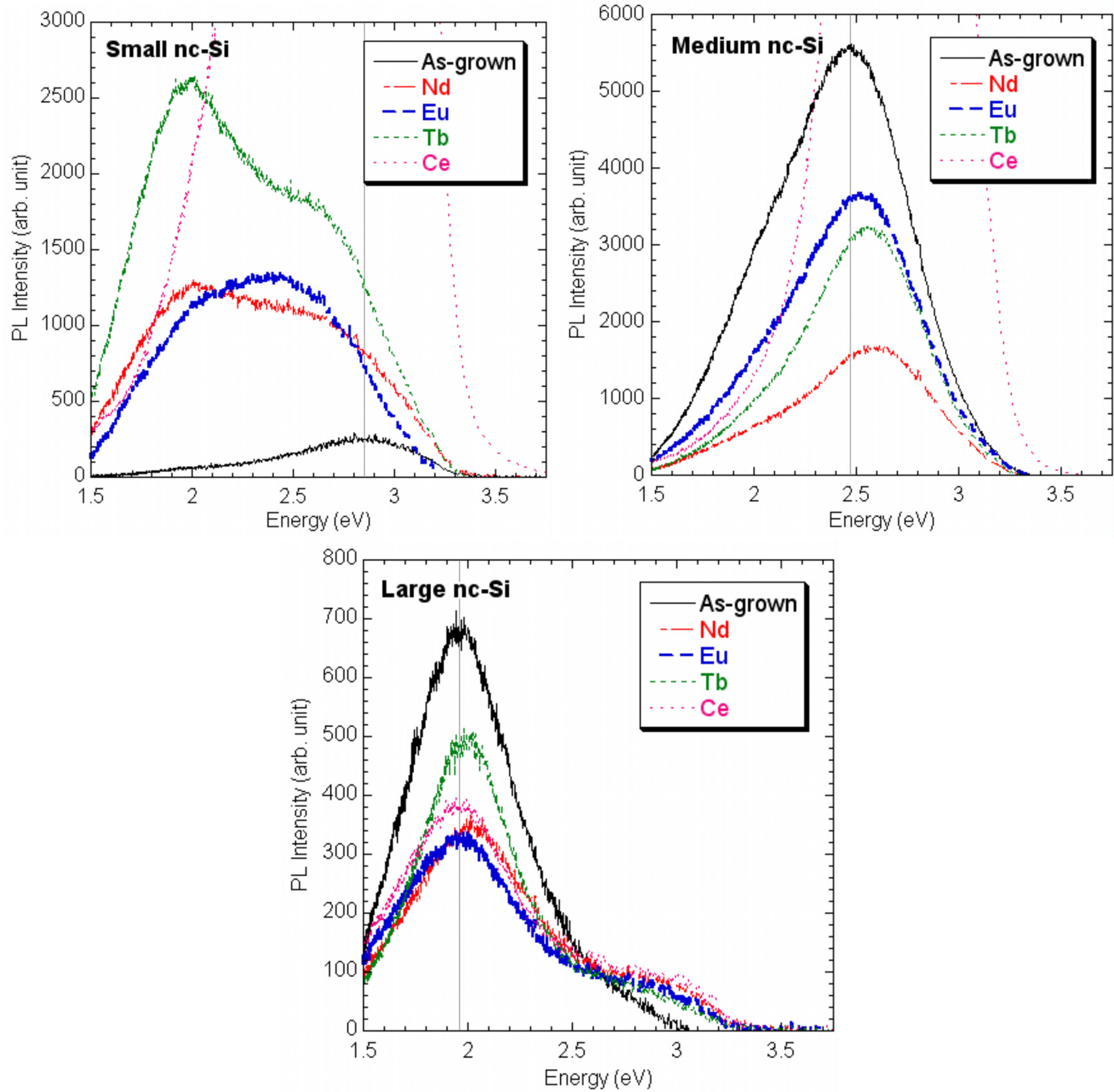

Figure 4.9: Room temperature confocal PL spectra of 200 nm thick amorphous SiN_x films grown on Si implanted with various lanthanide ions after the 800 °C heat treatment. Vertical lines show the approximate spectral centers of the as-grown films.

The absence of clear evidence of emissions from the lanthanide ions is likely the result of Nd, Eu, and Tb, similar to most lanthanide ions, having relatively low absorption cross sections (from 1×10^{-19} to $< 4 \times 10^{-21}$ cm^2), with narrow absorption bands (FWHM $<$ 1 nm), and lifetimes on the order of a few hundred microseconds [62, 64]. The combination of a low absorption cross section and narrow absorption bands create a situation where the excitation of the ion is difficult.

Once excited the relatively long lifetime enables non-radiative recombination processes to compete with the radiative recombination of the excitons. In the case of the previous studies involving Er ion implantation of SiN_x films containing Si nanocrystals, the excitation of Er resulted from an energy transfer from the nanocrystals to the Er ions [83,84]. This energy transfer results in the near extinction of the nanocrystal PL emission, which was not observed with the Nd, Eu, or Tb ions of this study.

4.3 Ce Implantation

Previous studies have shown that Ce doping, by way of diffusion from a CeF_3 thin film, can lead to the enhancement of the photoluminescence intensity of Si nanocrystals embedded in a SiO_x matrix [71,72,85]. These studies only considered one size of nanocrystal and the doping concentration was controlled by a combination of CeF_3 film thickness and the annealing temperature that led to diffusion. The present study enabled a more quantitative approach to the effect of Ce doping concentrations by the use of ion implantation and also investigated the effect of nanocrystal size.

4.3.1 Photoluminescence Enhancement

Implantations were carried out at room temperature with 63 keV Ce^{2+} ions at a fluence of 1×10^{15} ions/cm^2. Figure 4.10 shows the PL spectra obtained from the Ce implanted films compared to the as-grown films. The spectral center and intensity of the main PL emission from films containing large nanocrystals is essentially unchanged after Ce implantation, but there is the appearance of a broad peak at approximately 2.8 eV. For Ce implanted films containing both medium and small nanocrystals, there is an increase in the PL intensity. Films with the medium nanocrystals increased approximately four-fold and films with the small nanocrystals increased by nearly a factor of 30 after Ce implantation. The emission center of the small nanocrystals remains unchanged when compared to that of the as-grown film, but the PL center of the medium nanocrystals showed a blue-shift of 100 meV.

To reduce implantation damage, the implanted films were heat treated for 30 minutes under a flow of N_2 at 500 °C. Figure 4.11 shows the PL spectra obtained from the Ce implanted films after the 500 °C heat treatment, as well as those of the as-grown films. Heat treated Ce implanted films containing large nanocrystals showed a PL increase by a factor of 1.75 and a red-shift of 80 meV, compared with the as-grown film containing large nanocrystals. Heat treated Ce implanted films containing medium nanocrystals showed a PL intensity increase by a factor of 3.3 compared

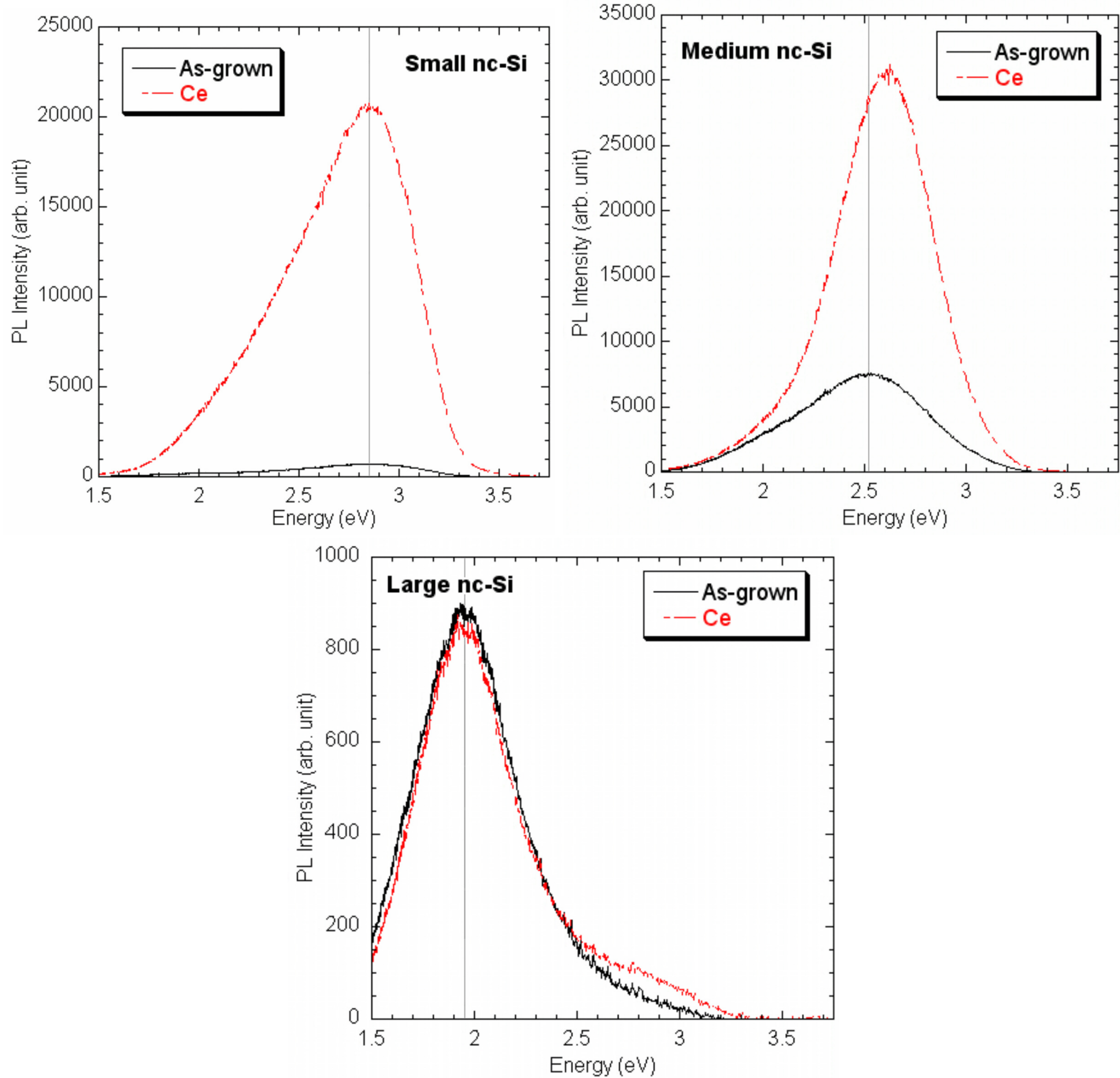

Figure 4.10: Room temperature confocal PL spectra of 200 nm thick amorphous SiN_x films grown on Si. Ce implanted films are compared with those of the as-grown film. Vertical lines show the approximate spectral centers of the as-grown films.

with the as-grown film, as well as a 170 meV blue-shift. Compared to the implanted film before heat treatment, this is a decrease in PL intensity and an additional blue-shift. A further increase in PL intensity of Ce implanted films containing small nanocrystals was observed after the heat treatment. PL intensity was more intense by a factor of 50 than the as-grown film and the increase was accompanied by a 90 meV blue-shift.

Figure 4.12 shows the PL spectra obtained from the Ce implanted films after a second heat treatment at 800 °C for 30 minutes under N_2 flow, as well as those of the as-grown films. Emission

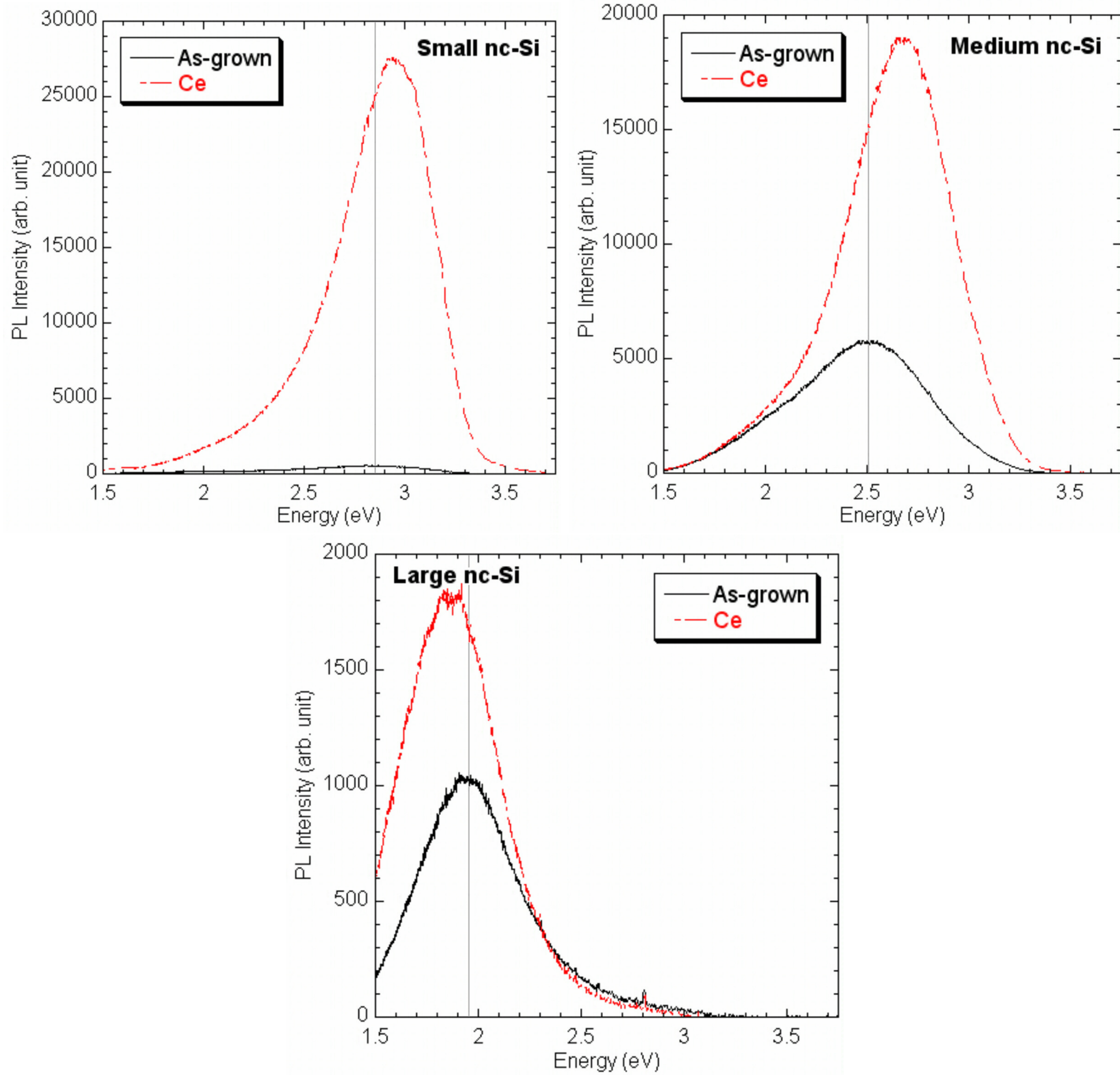

Figure 4.11: Room temperature confocal PL spectra of 200 nm thick amorphous SiN_x films grown on Si. Ce implanted films heat treated at 500 °C are compared with those of the as-grown films. Vertical lines show the approximate spectral centers of the as-grown films.

from the heat treated Ce implanted films containing large Si nanocrystals showed no spectral shift, but was nearly half as intense as the as-grown film. Again, as was observed for the Ce implanted film conatining large nanocrystals before heat treatment, there was a broad but relatively less intense second peak that appears in the vicinity of 3.0 eV. For the heat treated film containing the medium Si nanocrystals the blue shifting trend continued with the spectral center of the Ce implanted film being blue-shifted by 240 meV from that of the as-grown film. The 4.5-fold intensity increase of the

Ce implanted medium nanocrystals compared to the as-grown film was similar to that seen in the implanted and 500 °C heat treated films. The film containing small Si nanocrystals showed a further increase in PL intensity, with Ce implantation being about 82 times as intense as the as-grown film. A red-shift of 20 meV was observed in the spectral center of the heat treated Ce implanted film compared to the as-grown film.

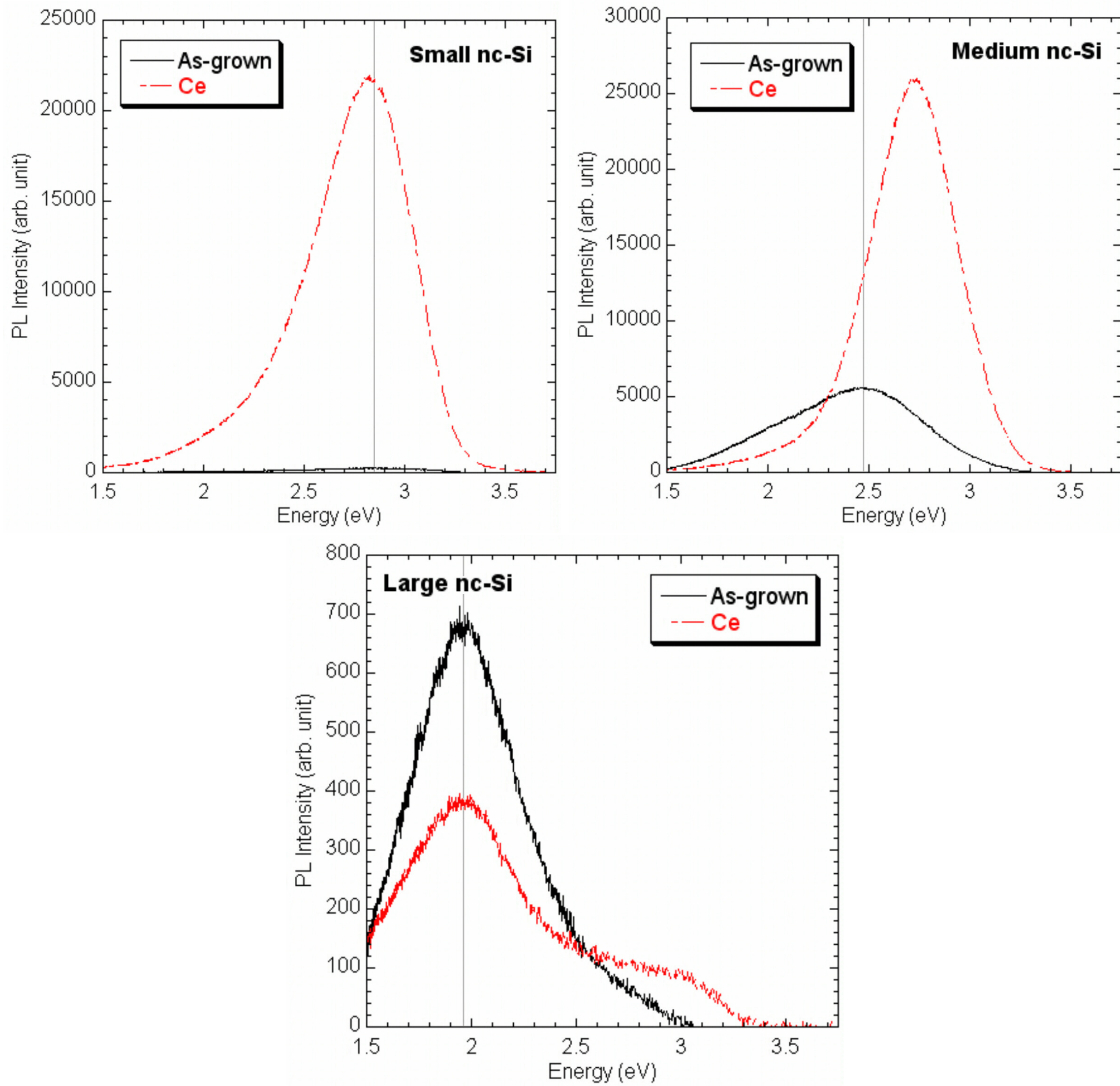

Figure 4.12: Room temperature confocal PL spectra of 200 nm thick amorphous SiN_x films grown on Si. Ce implanted films heat treated at 800 °C are compared with those of the as-grown films. Vertical lines show the approximate spectral centers of the as-grown films.

Table 4.1 gives a summary of the PL intensity change after Ce implantation and subsequent heat

treatments as a percentage of the PL intensity of the as-grown films, as well as the observed spectral shift relative to the spectral center of the as-grown films. Some trends imply that energy from the Ce ions is preferentially transferred to the smaller Si nanocrystals, resulting in a size dependent PL enhancement of the Si nanocrystals.

Table 4.1: Summary of Si nanocrystal PL intensity change and spectral shifting, relative to the as-grown film, due to Ce implantation.

Large nc-Si			
As-grown emission centered at 1.97 eV			
		Intensity change factor	Shift (meV)
Ce	as-implanted	1.0x	0
	500 °C	1.8x	-80
	800 °C	0.6x	0
Medium nc-Si			
As-grown emission centered at 2.48 eV			
		Intensity change factor	Shift (meV)
Ce	as-implanted	4.1x	100
	500 °C	3.3x	170
	800 °C	4.6x	240
Small nc-Si			
As-grown emission centered at 2.85 eV			
		Intensity change factor	Shift (meV)
Ce	as-implanted	29.5x	0
	500 °C	50.0x	90
	800 °C	82.4x	-20

First the SiN_x film containing the small Si nanocrystals shows the most enhancement in PL intensity when comparing the emission from as-grown films to that of films implanted with Ce. After implantation, the emission from the film with small Si nanocrystals increased by a factor of

29, after the 500 °C heat treatment there was additional enhancement resulting in a 50-fold total increase, and after the final heat treatment at 800 °C there was a total PL intensity increase of 82-fold compared to that of the as-grown film. This is a larger PL intensity increase than what has been reported in the literature. A group from Fudan University in China observed a 3.7-fold increase in the PL intensity of Si nanocrystals in a SiO_2 matrix when a single CeF_3 layer was used as a Ce dopant source [85]. The same group later used two CeF_3 layers, one on each side of the SiO_2 film containing the Si nanocrystals, and observed a 7.3-fold increase in the PL intensity of the Si nanocrystals [72]. A further hydrogenation process on the film with two doping layers achieved a final enhancement of a 14.6-fold increase of the PL intensity. In the present study a larger PL intensity increase observed when compared to that reported by Xie et al. [72]. In addition, the present synthesis method requires a lower thermal budget for specimen creation and doping, and also gives greater control over the doping concentration with the use of ion-implantation.

SiN_x films that contain medium Si nanocrystals showed an increase in PL intensity after Ce implantation, but the two heat treatments were not found to further increase PL intensity as was the case for the small nanocrystals. Instead of a continual increase in PL intensity with each heat treatment as was seen for the films containing the small nanocrystals, the films containing medium nanocrystals show a continual blue-shift of the PL emission spectral center. Starting with the as-grown emission centered at 2.48 eV, this center blue-shifts 100 meV after Ce implantation, followed by a further blue-shift of 70 meV after the 500 °C heat treatment, and finally by an additional 70 meV blue-shift with the 800 °C heat treatment. This resulted in a total blue-shift of 240 meV and placed the spectral center of the heat treated Ce implanted film at approximately 2.72 eV. This continual blue-shift implies that there is a continuous increase in emission intensity from smaller nanocrystals within the film. The SiN_x films contains a statistical distribution of Si nanocrystal sizes (standard deviation of $\sim$ 0.3 nm), and although the average diameter in this film was approximately 3.0 nm, smaller crystals exist in the film. The large intensity increase observed in the film with small nanocrystals and the observed blue-shift of the film with medium nanocrystals, implies that the sensitizing effect of Ce on Si nanocrystals is dependent upon size, with the emission of smaller nanocrystals being preferentially enhanced.

Finally, in the films containing large Si nanocrystals, there is little variation in either PL intensity or spectral center location for the as-grown state, the implanted state, or the heat treatmented films. The major difference between the implanted film containing large nanocrystals and the as-grown film was the appearance of a broad peak in the vicinity of 2.9 eV. The Ce implanted film with large nanocrystals after the 800 °C heat treatment also showed a new peak near 3.9 eV. Although this

peak was relatively weak, it could be the result of the Ce ions enhancing the emission from small Si nanocrystals that are present in the specimen, which would further support the claim that the Si nanocrystal and Ce ion interaction is strongest for the smaller nanocrystals.

4.3.2 Concentration Quenching

As the concentration of a species responsible for PL emission increases, the PL intensity should increase due to an increased number of recombination centers and more emitted photons. With most systems there is an optimal concentration, beyond which there will be an observed decrease in the PL intensity. This concentration quenching effect is the result of the fluorescing species spacing distance becoming small enough that the species can transfer energy between themselves. This interaction can eventually transfer the energy to impurity centers where the energy can decay non-radiatively or result in a photon emission at a mid-band-gap state. In either case, the PL intensity of the fluorescing species is decreased.

Based on the observed enhancement from the first Ce implantation, a series of films were prepared to investigate the dependence of implantation fluence on the PL of SiN_x films containing Si nanocyrstals. Films containing large, medium, or small Si nanocrystals were implanted with one of three different fluences, 3×10^{19}, 5×10^{20}, or 1×10^{26} ions/cm^2. Figure 4.13a shows the PL emission observed from films containing small Si nanocrystals implanted with Ce ions at different fluences. The PL intensity of the films with small Si nanocrystals shows a continuous increase with increasing fluence over the whole range considered.

Figure 4.13b shows the PL emission observed from films containing medium Si nanocrystals implanted with Ce ions at different fluences. The PL intensity of the films with medium Si nanocrystals shows an increase with fluence up to 5×10^{20} ions/cm^2 and then a decrease for a fluence of 1×10^{26} ions/cm^2.

Figure 4.13c shows the PL emission observed for a film containing large Si nanocrystals implanted with Ce ions at different fluences. The PL intensity of the films with large Si nanocrystals shows a continual decrease with increasing Ce implantation fluence.

Concentration quenching has been observed in a variety of systems and results when dopant concentrations are high enough that the spatial separation of neighboring ions make ion-ion interactions the most efficient energy transfer mechanism [2, 70, 84, 120]. The energy from a photoexcited ion is transferred to a neighboring ion, which in turn transfers the energy to another neighboring ion, and so on until the energy reaches a non-radiative recombination center. This could occur, for example,

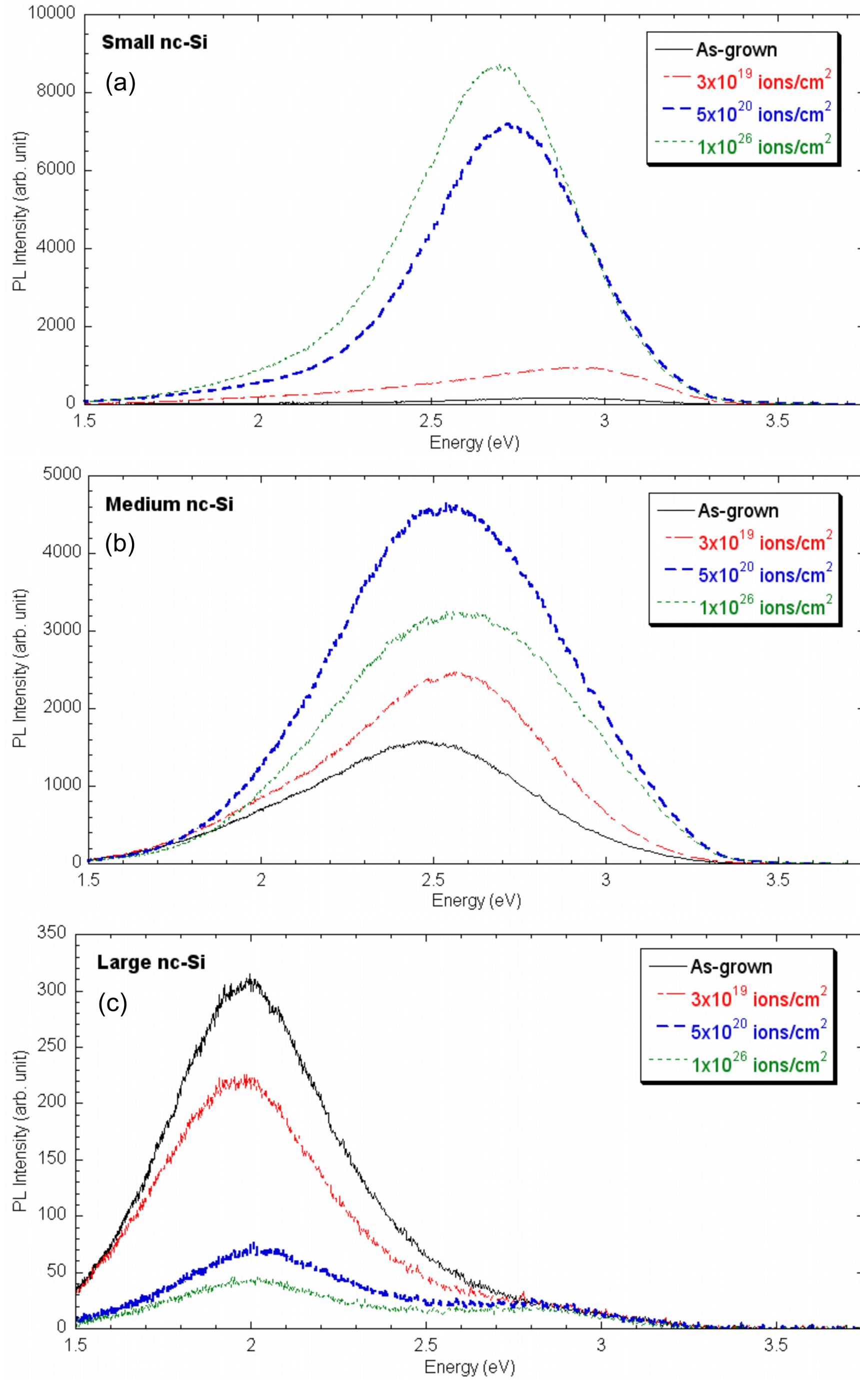

Figure 4.13: Room temperature confocal PL spectra of 200 nm thick amorphous SiN_x films grown on bulk Si that contain a) small, b) medium, and c) large Si nanocrystals. The as-grown films and films implanted with Ce ions at fluences of 3×10^{19}, 5×10^{20}, and 1×10^{26} ions/cm^2 are shown.

when an excited Ce ion can more easily transfer its energy to a neighboring Ce ion than to a Si nanocrystal, as a result of the average distance between neighboring ions being sufficiently small.

HRTEM measurements by Kim et al. [51] on a set of films previously prepared under the same conditions as those of the present study indicated that the density of the largest Si nanocrystals is $\sim 6 \times 10^{11}$ nanocrystals/cm^2. As the nanocrystal size increases, the number of ions near a single nanocrystal increases making it more likely that energy from an excited Ce ion will be transfered to another Ce ion than to a Si nanocrystal. As the Si nanocrystals decrease in size and their density increases, there will be fewer Ce ions competing to transfer their energy to a single Si nanocrystal and the transfer can remain efficient even at large doping concentrations. In the present study PL emission from the small nanocrystals was found to increase with increasing fluence, while the medium nanocrystals showed a decrease in PL intensity for the highest fluence, and the largest nanocrystals show a decrease in PL intensity with increasing fluence. For the films containing medium nanocrystals, at a fluence between 5×10^{20} and 1×10^{26} ions/cm^2 the spacing between the Ce ions reaches a critical distance such that they begin to transfer energy to non-radiative centers. For the large nanocrystals this critical distance has already been achieved for the lowest fluence, and as the fluence increases quenching becomes more pronounced.

4.4 Energy Transfer Mechanism

Based on the results presented in Section 4.3, a plausible explanation for the energy transfer mechanism is given. Xie et al. [72] offered three possible mechanisms for the enhancement of Si nanocrystal PL after Ce doping. They are: 1) a fluorescence resonant energy transfer (FRET) from a Ce ion to the Si nanocrystal, 2) an exciton charge transfer from a Ce ion to the Si nanocrystal, and 3) passivation of dangling bonds at the Si nanocrystal/matrix interface. They observed additional PL enhancement in Ce doped specimens after a hydrogenation process, which would eliminate the passivation mechanism. Results from the present study also seem to rule out the passivation mechanism as well, since H is present in the form of Si-H and N-H bonds.

Interactions between lanthanoid ions and semiconductor nanocrystals have been widely reported, with much attention given to Er and Si nanocrystals in a SiO_2 matrix as a result of potential applications in telecommunications [1–6]. The emission of Er is at 1540 nm, which coincides with the absorption minimum of optical fibers. It has been found that the Si nanocrystals act as a sensitizer to the Er ions, as a result of an energy transfer from the excited Si nanocrystal to the Er ion. Effects such as temperature, excitation energy and power, nanocrystal size, and Er concentration have all

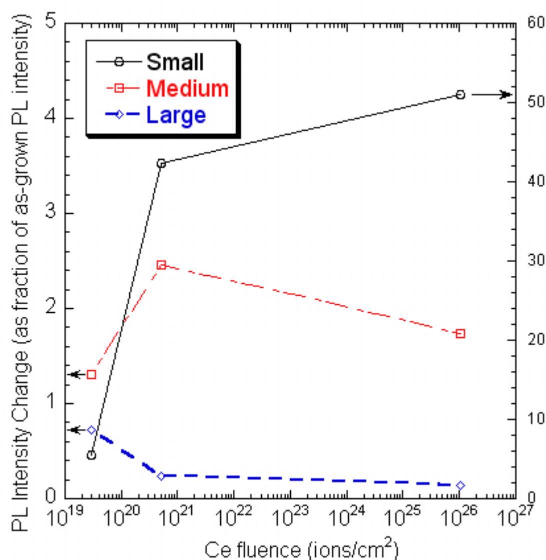

Figure 4.14: PL enhancement of Si nanocrystals after the implantation of Ce ions at fluences of 3×10^{19}, 5×10^{20}, and 1×10^{26} ions/cm^2. Enhancement is given as a fraction of the the intensity of the as-grown film for each size of nanocrystal. Note that fluence is plotted on a log scale.

been examined and all show that there is an energy transfer from the Si nanocrystal to the Er ion. Others have investigated and found similar behavior with the use of a SiN_x substrate instead of SiO_x [83]. Ge nanocrystals in SiO_2 that have been doped with either Er or Yb have also shown a preferential energy transfer to the rare-earth ion [121].

Energy transfer from Si nanocrystals to Er ions has been investigated both theoretically and experimentally. Kenyon et al. [122] investigated PL from Er-doped Si nanocrystals in a silica matrix. To model the energy coupling, a resonant energy transfer between the Si nanocrystals and the Er ions consistent with the Förster model was assumed. They also point out two other studies [82,123] in which the energy transfer is considered theoretically using two different approaches. The first is Qin et al. [123] who use a quantum-confinement luminescent center (QCLC) model, where the Er-ion is excited by a photoexcited free electron that tunnels from the nanocrystal to the ion. They considered a SiO_2 matrix and the argument that an electron can tunnel up to 10 Å into the barrier. The second study, by Franzo et al. [82], considers the dynamics of the exchange based on rate equations using time resolved PL measurements. However, no specific mechanism for the

energy transfer was proposed. It was argued that transfer takes place over some distance, since their experimental results did not indicate that the Er was inside the nanocrystal. Based on the spectral shape of the Er PL emission, they concluded that the excited Er ions are located in the SiO_2 matrix and not within the Si nanocrystals.

Imakita et al. [124] performed time dependent PL measurements on Er doped Si nanocrystals in SiO_2 which showed there were two transfer mechanisms present, one slow and the other fast. Er ions located within 1.5 nm of the Si nanocrystal were excited by a fast process (< 1 μs). The slow process (several tens of μs) was observed for Er ions located within 2.5 nm of the nanocrystal surface when no Er ions were located within 1.5 nm of that particular nanocrystal. The ratio of the two processes was dependent upon both the nanocrystal size and the Er concentration, where the fast mechanism was dominant in large nanocrystals and high Er concentrations. They attributed the fast process to an exciton being transfered from the Si nanocrystal to the Er ion by an Auger-like process. The slow process was attributed to the Förster type energy transfer.

Priolo et al. [2] observed that with increasing Er concentrations, the effective excitation cross section increases and the PL lifetime decreases. This was explained by Er-Er interactions resonantly transferring energy from the Si nanocrystal to a quenching center. They found that the decrease in PL lifetime began to occur for Er concentrations greater than $\sim 2 \times 10^{20}$ cm^{-3}. This is consistent with Park et al. [84] who showed smaller Si quantum dots had stronger Er emission than larger dots when the Er concentration was 10^{21} cm^{-3}. However, when the Er concentration was 10^{19} cm^{-3}, only the specimen with the largest quantum dots showed PL originating from the Er. At the higher concentrations, Er-Er interactions transfered energy from the largest quantum dots to non-radiative quenching sites.

Other groups have also pointed to resonant energy transfers involving semiconductor quantum dots. Anni et al. [125] demonstrated FRET in a system containing semiconductor nanostructures. Their system was a light emitting organic polymer acting as the donor and a CdSe/ZnS core/shell quantum dot acting as the acceptor. Time resolved PL was the principle investigation tool, where all measurements were performed at 18 K and their system resolution was approximately 10 ps. Measured relaxation times were typically a few hundred ps. Kovalev et al. [126] reported a resonant energy transfer from Si nanocrystals to molecular oxygen.

With most evidence pointing toward a Förster resonance energy transfer in the Er doped Si nanocrystal system, more discussion on the process and its relevance to the Ce doped Si nanocrystal system is warranted. Förster's theory on intermolecular energy transfer dates to his early work in 1948 [127] (English translation [128]) where energy transfer between identical fluorophores was

considered. His subsequent update in 1965 took on a more general approach to resonant energy transfer between dissimilar donor/acceptors [129].

Förster resonance energy transfer (FRET), or fluorescence resonance energy transfer as it is sometimes called, is most commonly utilized in biological systems and both the donor and acceptor are fluorophor molecules [130]. Energy is non-radiatively transfered by an electric dipole-dipole coupling between the donor and the acceptor. This dipole-dipole coupling and subsequent energy transfer can occur when the emission spectrum of the donor overlaps the absorption spectrum of the acceptor and the two are physically separated by a distance less than their Förster radius (on the order of 1 to 10 nm). It should be emphasized that although it is referred to as fluorescence resonance energy transfer, the energy transfer is non-radiative and does not involve the emission of a photon. Consequently, the term Förster resonant energy transfer is becoming more commonly used.

The Förster rate can be represented by the overlap of the normalized fluorescence spectrum of the donor with the normalized absorption spectrum of the acceptor, with more overlap indicating a higher rate [131]. If we assume Ce to be the donor for all of the films in the present study, the emission spectrum of the donor will be unchanged from film to film. Ce has its strongest emission at 3.35 and 3.06 eV (370 and 405 nm) and its $5d \rightarrow 4f$ transition is electric-dipole allowed [62]. The electric-dipole nature of Ce is important since it is necessary for FRET, and many of the lanthanide transitions, especially $4f \rightarrow 4f$, are often magnetic-dipole allowed. Ce donors are not necessarily single ions, but may be clusters of precipitates, especially in the heat treated films. Precipitates as large as 10-20 nm were observed by Polman et al. [132] for the case of Er ions implanted with a fluence of 5×10^{15} ions/cm^2 in SiO_2 and subsequently annealed at 1200 °C.

The absorption spectrum of the acceptor (i.e., the Si nanocrystal) will be dependent upon the size of the nanocrystals contained within the film. Quantum confinement leads to a blue-shift in both the emission and absorption spectra as nanocrystal size decreases. As a result, when the nanocrystal becomes smaller there is an increased overlap in the donor emission spectrum and acceptor absorption spectrum, which implies a higher Förster rate. With increasing spectral overlap, an oscillating dipole in the donor can more easily resonate with a dipole in the acceptor in the near field regime [133]. An increase in the FRET rate will result in a decrease in the lifetime of the donor as indicated by the equation $1/\tau = k_{FRET} + k_{OP}$, where τ is the fluorescence lifetime of the donor, k_{FRET} is the rate constant for FRET, and k_{OP} is the rate constant for all other processes [133].

Lanthanoids (almost always Tb or Eu) are being used as resonant energy transfer donors in order to study proteins and other large biological molecules [133,134]. Typically the FRET mechanism is used to measure the distance between different binding sites. Distance measurements result from the

Förster equation, which is given as $R_o^6 = 8.79 \times 10^{23} k^2 n^{-4} \Phi_d J_{da}$, where R_o is the donor/acceptor separation distance when FRET is 50% (Å), k is an orientation factor given as 2/3 for a random distribution, n is the refractive index of the solvent, Φ_d is the quantum efficiency of the donor, and J_{da} is the overlap of the donor emission and acceptor absorption (cm^3/M) [133]. FRET efficiency can be determined by steady state measurements using $E = (1 - I_{DA}/I_D)$, where I_{DA} and I_D are the donor emission intensities both in the presence of and without the acceptor, or time-resolved measurements using $E = (1 - \tau_{DA}/\tau_D)$, where τ_{DA} and τ_D are the donor emission decay time both in the presence of and without the acceptor.

Lanthanoid use in FRET experiments is advantageous from the point of view that their lifetime is on the order of a millisecond which simplifies the instrumentation required for time resolved measurements. However, the relatively long lifetime means that the emission intensity is rather weak, necessitating a low noise detector [134]. Energy transfer can be measured in a number of ways: 1) by a decrease in donor fluorescence intensity (because some of the energy is going to the acceptor, instead of into photons), 2) by a decrease in donor excited state lifetime (because energy transfer to the acceptor is an additional relaxation pathway of the donor excited state), 3) by a decrease in donor photobleaching rate (because the excited state lifetime of the donor decreases with energy transfer, which decreases the probability of a chemical reaction leading to photobleaching of the donor), or 4) by an increase in acceptor fluorescence (because energy transfer is an additional excitation pathway).

There were two key observations made from the Ce implantation and subsequent heat treatments. First, the films containing small nanocrystals showed the greatest increase in PL after Ce implantation and heat treatments. Second, the PL spectra of the films containing medium nanocrystals blue-shifted after heat treatments. The fact that the small nanocrystals show the largest PL intensity increase, the medium show a moderate increase, and the largest show no increase, indicate that the energy transfer is size dependent. Further, the blue-shift of the PL emission from the film with medium nanocrystals and the appearance of a higher energy peak in the film with large nanocrystals shows that the energy is transferred preferentially to smaller nanocrystals having a higher energy band-gap. This behavior is consistent with a FRET model since the absorption band of smaller nanocrystals is going to have more overlap with the emission band of Ce.

Additionally, the Ce transition is important since FRET requires both the donor and acceptor to have electric dipoles. Vedda et al. [135] found in Ce-doped silica glasses that the photoluminescence excitation (PLE) spectrum of Ce^{3+} peaks at 325 nm (i.e., say that a 325 nm excitation source yielded the strongest Ce^{3+} related emission). This energy corresponds to the lowest $4f \rightarrow 5d$ transition in

Ce^{3+}. The $f \rightarrow d$ transitions are electric dipole in nature, as compared to $f \rightarrow f$ transitions which are not. Although time dependent studies are necessary to investigate possible transfer mechanisms, a Förster energy transfer appears to be a plausible mechanism.

Chapter 5

Conclusions and Future Work

5.1 Conclusions

A study of the effect of lanthanoid ion implantation on the emission of Si nanocrystals embedded in SiN_x films has been performed. Changes observed in the PL response of the films indicate that there are interactions between the lanthanoid ions and the Si nanocrystals. Implanted Ce ions were found to enhance the intensity of the Si nanocrystal PL emission, with emission from smaller nanocrystals showing the greatest intensity increase. The observed trends imply that the energy transfer mechanism between the Ce ions and the Si nanocrystals will only take place when the Si nanocrystals are sufficiently small and the transfer process becomes more efficient as the nanocrystal size decreases. The following are specific conclusions resulting from this investigation.

1. Quantum confinement of carriers in the Si nanocrystals within the as-grown amorphous SiN_x films were responsible for the observed blue-shift of the PL emission with decrease in nanocrystal size.

2. Raman spectroscopy showed that films created with higher SiH_4 flow rates (larger Si nanocrystals) had more Si-H bonds and fewer N-H bonds than those grown with lower flow rates, likely as a result of the film growth rate. Higher SiH_4 flow rates led to faster film growth rates, suggesting that there is less time for N-H bonds to form and more residual Si-H bonds that remain.

3. As a result of the 200 nm thick SiN_x films being effectively transparent to the excitation laser light, strong Raman scattering from the substrate made the observation of Raman scattering from Si nanocrystals impossible.

4. Implanted Ce ions act as a sensitizer for the PL emission from the films containing Si nanocrystals. Compared to the as-grown films, the observed enhancement was nearly 30-fold in the film containing small Si nanocrystals. The film containing medium nanocrystals had a 4-fold increase in PL intensity and the film containing large nanocrystals showed no intensity change.

5. Heat treatments of 500 °C and then 800 °C resulted in the PL intensity from the Ce implanted film containing the small Si nanocrystals to increase 50-fold and 80-fold, respectively, compared to the as-grown films. The same heat treatments for the Ce implanted film containing medium nanocrystals did not show further PL intensity enhancement compared to the as-implanted film, but the spectral center of the PL emission showed a blue-shift of 70 meV after each heat treatment. Ce implanted films containing large nanocrystals showed relatively no changes in intensity or spectral center.

6. Concentration quenching was observed, such that with a sufficient Ce concentration, energy is transferred by Ce-Ce interactions to non-radiative centers. Films containing small nanocrystals showed no signs of concentration quenching up to a fluence of 1×10^{26} ions/cm^2. As the nanocrystal size increased, concentration quenching took place at lower fluences. Films with medium nanocrystals show a decrease in PL intensity of the highest fluence, which would indicate that concentration quenching begins at a fluence between 5×10^{20} and 1×10^{26} ions/cm^2. Films containing large nanocrystals show a PL intensity decrease at the lowest fluence considered (2×10^{19} ions/cm^2).

7. Films implanted with Nd, Eu, and Tb showed little change prior to heat treatment. After the 500 °C heat treatment, the films containing small nanocrystals showed an increase in PL intensity and a red-shift of the spectral centers. The film implanted with Eu showed the most increase (2-fold increase) and red-shifted from 2.85 eV to ∼2.4 eV. After the 800 °C heat treatment the films containing small nanocrystals showed a further increase in PL intensity, with that implanted by Tb increasing the most (a 10-fold increase). The PL spectra from films implanted with Tb and Nd appear to consist of two peaks after the heat treatments, the first centered near 2.0 eV and the second near 2.7 eV; the 2.0 eV peak shows the most enhancement with heat treatments. Films containing medium and large nanocrystals showed no spectral shifting and no clear trends in PL intensity.

5.2 Future Work

1. Using time resolved PL, investigate the energy transfer mechanism between the Ce-ions and Si nanocrystals to see if it is a Förster type energy transfer. PL lifetimes of the nanocrystals, and if observable the Ce ion emission lifetimes, should give insight into the nature of the energy transfer mechanism.

2. Investigate the coupled effects of strain and quantum confinement on the PL response of the Si nanocrystals.

3. Use HRTEM on Ce implanted films to determine the size of Si nanocrystals and to determine if Ce precipitates form after heat treatments.

4. Consider a wider range of heat treatment temperatures.

5. Deposit an Al reflector film on the substrate prior to SiN_x film growth in order to investigate the Raman spectra of the Si-rich SiN_x with a lower influence from the substrate signals.

6. Investigate why the as-grown films containing small nanocrystals have a lower PL intensity than the films containing medium nanocrystals. The smaller nanocrystals should have a higher oscillator strength than the medium nanocrystals, and as a result higher PL intensity.

Bibliography

[1] P.G. Kik, M.L. Brongersma, and A. Polman. Strong exciton-erbium coupling in Si nanocrystal-doped SiO_2. *Applied Physics Letters*, 76:2325, 2000.

[2] F. Priolo, G. Franzo, D. Pacifici, V. Vinciguerra, F. Iacona, and A. Irrera. Role of the energy transfer in the optical properties of undoped and Er-doped interacting Si nanocrystals. *Journal of Applied Physics*, 89:264–272, 2001.

[3] G. Franzo, S. Boninelli, D. Pacifici, F. Priolo, F. Iacona, and C. Bongiorno. Sensitizing properties of amorphous Si clusters on the 1.54-μm luminescence of Er in Si-rich SiO_2. *Applied Physics Letters*, 82:3871, 2003.

[4] M. Fujii, M. Yoshida, Y. Kanzawa, S. Hayashi, and K. Yamamoto. 1.54 μm photoluminescence of Er^{3+} doped into SiO_2 films containing Si nanocrystals: Evidence for energy transfer from Si nanocrystals to Er^{3+}. *Applied Physics Letters*, 71:1198–1200, 1997.

[5] M. Fujii, M. Yoshida, S. Hayashi, and K. Yamamoto. Photoluminescence from SiO_2 films containing Si nanocrystals and Er: Effects of nanocrystalline size on the photoluminescence efficiency of Er^{3+}. *Journal of Applied Physics*, 84:4525–4531, 1998.

[6] I. Izeddin and M. Fujii T. Gregorkiewicz. Non-radiative sub-microsecond recombination of excited Er^{3+} ions in SiO_2 sensitized with Si nanocrystals. *Physica E*, 38:144–147, 2007.

[7] R.E. Hummel. *Electronic Properties of Materials*. Springer-Verlag, 2nd edition, 1993.

[8] L.E. Brus. Zero-dimensional excitons in semiconductor clusters. *IEEE Journal of Quantum Electronics*, 22:1909–1914, 1986.

[9] L.E. Brus. Electron-electron and electron-hole interactions in small semiconductor crystallites: The size dependence of the lowest excited electronic state. *Journal of Chemical Physics*, 80:4403–4409, 1984.

[10] European Commission. *Technology Roadmap - Optoelectronic interconnects for integrated circuits*, 2nd edition, 1999.

[11] S. Tiwari, F. Rana, H. Hanafi, A. Hartstein, and E.F. Crabbe. A silicon nanocrystals based memory. *Applied Physics Letters*, 68:1377–1379, 1996.

[12] J. De la Torre, G. Bremond, M. Lemiti, G. Guillot, P. Mur, and N. Buffet. Using silicon nanostructures for the improvement of silicon solar cells' efficiency. *Thin Solid Films*, 511-512:163–166, 2006.

[13] C. Kittel. *Introduction to Solid State Physics*. John Wiley and Sons, 8th edition, 2005.

[14] *Periodic Table of the Elements*. Sargent-Welch Scientific, 5th edition, 1968.

[15] M.A. Green. Intrinsic concentraton, effective density of states, and effective mass in silicon. *Journal of Applied Physics*, 67:2944–2954, 1990.

[16] A.D. Yoffe. Low-dimensional systems: quantum size effects and electronic properties of semiconductor microcrystallites (zero-dimensional systems) and some quasi-two-dimensional systems. *Advances in Physics*, 42:173–266, 1993.

[17] O. Madelung, editor. *Semiconductors*. Springer-Verlag, 1991.

[18] D.E. Aspnes. *Properties of Crystalline Silicon*, chapter Optical Properties. INSPEC, IEE, 1999.

[19] S. Nishibe, T. Sasaki, H. Harima, K. Kisoda, T. Yamazaki, and W.S. Yoo. Raman study on the process of Si advanced integrated circuits. *Journal of Physics and Chemistry of Solids*, 32:211–215, 2006.

[20] E. Anastassakis and E. Burstein. Morphic effects II - effects of external forces on the frequencies of the $q \approx 0$ optical phonons. *Journal of Physics and Chemistry of Solids*, 32:563–570, 1971.

[21] I. De Wolf. Micro-Raman spectroscopy to study local mechanical stress in silicon integrated circuits. *Semiconductor Science and Technology*, 11:139–154, 1996.

[22] K. Uchinokura, T. Sekine, and E. Matsuura. Critical-point analysis of the two-phonon Raman spectrum of silicon. *Journal of Physics and Chemistry of Solids*, 35:171–180, 1974.

[23] A. Zwick and R. Carles. Multiple order Raman scattering in crystalline and amorphous silicon. *Physical Review B*, 48:6024–6032, 1993.

[24] S.S. Iyer and Y.-H. Xie. Light emission from silicon. *Science*, 260:40–46, 1993.

[25] D.J. Lockwood. *Light Emission in Silicon: From Physics to Devices*, chapter Light Emission in Silicon. Academic Press, 1998.

[26] U. Gnutzmann and K. Clausecker. Theory of direct optical transition in an optical indirect semiconductor with a superlattice structure. *Applied Physics B*, 3:9–14, 1974.

[27] U. Menczigar, G. Abstreiter, J. Olajos, H. Grimmeiss, H. Kibble, H. Presting, and E. Kasper. Enhanced bandgap luminescence in strain-symmetrized $(\mathrm{Si})_m/(\mathrm{Ge})_n$ superlattices. *Physical Review B*, 47:40999–4102, 1993.

[28] J. Engvall, J. Olajos, H.G. Grimmeiss, H. Kibble, and H. Presting. Luminescence from monolayer-thick Ge quantum wells embedded in si. *Physical Review B*, 51:2001–2004, 1995.

[29] D.J. Lockwood, Z.H. Lu, and J.-M. Baribeau. Quantum confined luminescence in $\mathrm{Si/SiO_2}$ superlattices. *Physical Review Letters*, 76:539–541, 1995.

[30] J.-P. Noel, N.L. Rowell, D.C. Houghton, and D.D. Perovic. Intense photoluminescence between 1.3 and 1.8 μm from strained $\mathrm{Si_{1-x}Ge_x}$alloys. *Applied Physics Letters*, 57:1037–1039, 1990.

[31] N.L. Rowell, J.-P. Noel, D.C. Houghton, and M. Buchanan. Electroluminescence and photoluminescence from $\mathrm{Si_{1-x}Ge_x}$ alloys. *Applied Physics Letters*, 58:957–958, 1991.

[32] S. Oguz, W. Paul, T.F. Deutsch, B.-Y. Tsaur, and D.V. Murphy. Synthesis of metastable, semiconducting Ge-Sn alloys by pulsed UV laser crystallization. *Applied Physics Letters*, 43:848–850, 1983.

[33] L.T. Canham, K.G. Barraclough, and D.J. Robbins. 1.3-μm light-emitting diode from silicon electron irradiated at its damage threshold. *Applied Physics Letters*, 51:1509–1511, 1987.

[34] H. Ennen, G. Pomrenke, A. Axmann, K. Eisele, W. Haydl, and J. Schneider. 1.54-μm electroluminescence of erbium-doped silicon grown by molecular beam epitaxy. *Applied Physics Letters*, 46:381–383, 1985.

[35] M.O. Henry, E.C. Lightowlers, N. Killoran, D.J. Dunstan, and B.C. Cavenett. Bound exciton recombination in beryllium-doped silicon. *Journal of Physics C*, 14:L255–L261, 1981.

[36] P.L. Bradfield, T.G. Brown, and D.G. Hall. Electroluminescence from sulfur impurities in a p-n junction formed in epitaxial silicon. *Applied Physics Letters*, 55:100–102, 1989.

[37] G. Davies. The optical properties of luminescence centres in silicon. *Physics Reports*, 176:83–188, 1989.

[38] L.C. Kimerling, K.D. Kolenbrander, J. Michel, and J. Palm. Light emission from silicon. *Solid State Physics*, 50:333–381, 1997.

[39] G.A Ozin and A.C. Arsenault. *Nanochemistry: A Chemical Approach to Nanomaterials*. Royal Society of Chemistry, 1st edition, 2005.

[40] A. Uhlir. Electrolytic shaping of germanium and silicon. *Bell System Technical Journal*, 35:333–347, 1956.

[41] M.I.J. Beale, J.D. Benjamin, M.J. Uren, N.G. Chew, and A.G. Cullis. An experimental and theoretical-study of the formation and microstructure of porous silicon. *Journal of Crystal Growth*, 73:622–636, 1985.

[42] C. Pickering, M.I.J. Beale, D.J. Robbins, P.J. Pearson, and R. Greef. Optical studies of the structure of porous silicon films formed in p-type degenerate and non-degenerate silicon. *Journal Physics C: Solid State Physics*, 17:6535–6552, 1984.

[43] S.R. Goodes, T.E. Jenkins, M.I.J. Beale, J.D. Benjamin, and C. Pickering. The characterisation of porous silicon Raman spectroscopy. *Semiconductor Science and Technology*, 3:483–487, 1988.

[44] L.T. Canham. Silicon quantum wire array fabrication by electrochemical and chemical dissolution of wafers. *Applied Physics Letters*, 57:1046–1048, 1990.

[45] H. Takagi, H. Ogawa, Y. Yamazaki, A. Ishizaki, and T. Nakagiri. Quantum size effects on photoluminescence in ultrafine Si particles. *Applied Physics Letters*, 56:2379–136, 1990.

[46] C. Wu, C.H. Crouch, L. Zhao, and E. Mazur. Visible luminescence from silicon surfaces microstructured in air. *Applied Physics Letters*, 81:1999–2001, 2002.

[47] P.M. Fauchet. Photoluminescence and electroluminescence from porous silicon. *Journal of Luminescence*, 70:294–309, 1996.

[48] M.V. Wolkin, J. Jorne, P.M. Fauchet, G. Allan, and C. Delerue. Electronic states and luminescence in porous silicon quantum dots: The role of oxygen. *Physical Review Letters*, 82:197–200, 1999.

[49] T. Shimizu-Iwayama, S. Nakao, and K. Saitoh. Visible photoluminescence in Si^+-implanted thermal oxide films on crystalline Si. *Applied Physics Letters*, 65:1814–1816, 1994.

[50] S. Cheylan and R.G. Elliman. The effect of ion dose and annealing ambient on room temperature photoluminescence from Si nanocrystals in SiO_2. *Nuclear Instruments and Methods in Physics Research B*, 148:986–990, 1999.

[51] T.-Y. Kim, N.-M. Park, K.-H. Kim, G.Y. Sung, Y.-W. Ok, T.-Y. Seong, and C.-J. Choi. Quantum confinement effect of silicon nanocrystals *in situ* grown in silicon nitride films. *Applied Physics Letters*, 85:5355, 2004.

[52] T. Baron, F. Martin, P. Mur, C. Wyon, and M. Dupuy. Silicon quantum dot nucleation on Si_3N_4, SiO_2 and SiO_xN_y substrates for nanoelectronic devices. *Journal of Crystal Growth*, 209:1004–1008, 2000.

[53] J. Valenta, R. Juhasz, and J. Linnros. Photoluminescence spectroscopy of single silicon quantum dots. *Applied Physics Letters*, 80:1070–1072, 2002.

[54] J.R. Heath. A liquid-solution-phase synthesis of crystalline silicon. *Science*, 258:1131–1133, 1992.

[55] K. Watanabe, M. Fujii, and S. Hayashi. Growth of Ge microcrystals in SiO_2 thin film matrices: a Raman and electron microscopic study. *Japanese Journal of Applied Physics*, 30:687–694, 1991.

[56] N.-M. Park, C.-J. Choi, T.-Y. Seong, and S.-J. Park. Quantum confinement in amorphous silicon quantum dots embedded in silicon nitride. *Physical Review Letters*, 86:1355–1357, 2001.

[57] V.A. Volodin, M.D. Efremov, V.A. Gritsenko, and S.A. Kochubei. Raman study of silicon nanocrystals formed in SiN_x films by excimer laser or thermal annealing. *Applied Physics Letters*, 73:1212–1214, 1998.

[58] K. Watanabe, M. Fujii, and S. Hayashi. Resonant excitation of Er^{3+} by the energy transfer from Si nanocrystals. *Journal of Applied Physics*, 90:4761–4767, 2001.

[59] C. Kittel. *Nomenclature of inorganic chemistry. IUPAC recommendations 2005*. Royal Society of Chemistry, 2005.

[60] L. Esterowitz, A. Schnitzler, J. Noonan, and J. Bahler. Rare earth infrared quantum counter. *Applied Optics*, 7:2053–2070, 1968.

[61] T.L. Brown, H.E. LeMay, and B.E. Bursten. *Chemistry*. Prentice Hall, 7th edition, 1997.

[62] J.J. Zayhowski, D. Welford, and J. Harrison. *The Handbook of Photonics*, chapter Miniature solid-state lasers. CRC Press, 2nd edition, 2006.

[63] G.H. Dieke and H.M. Crosswhite. The spectra of the doubly and triply ionized rare earths. *Applied Optics*, 2:675–686, 1963.

[64] M.L.V. Werts. Making sense of lanthanide luminescence. *Science Progress*, 88:101–131, 2005.

[65] G.H. Dieke. *Spectra and energy levels of rare earth ions in crystals*. Wiley Interscience, 1968.

[66] T. Aitasalo, J. Hölsä, M. Lastusaari, J. Niittykoski, and F. Pelle. Delayed luminescence of Ce^{3+} doped X_1 form of Y_2SiO_5. *Optical Materials*, 27:1511–1515, 2005.

[67] T. Aitasalo, J. Hölsä, M. Lastusaari, J. Legendziewicz, J. Niittykoski, and F. Pelle. Delayed luminescence of Ce^{3+} doped Y_2SiO_5. *Optical Materials*, 26:107112, 2004.

[68] C. Lin, H. Wang, D. Kong, M. Yu, X. Liu, Z. Wang, and J. Lin. Silica supported submicron SiO_2@Y_2SiO_5:Eu^{3+} and SiO_2@Y_2SiO_5:Ce^{3+}/Tb^{3+} spherical particles with a core-shell structure: Sol-gel synthesis and characterization. *European Journal of Inorganic Chemistry*, 2006:3667–3675, 2006.

[69] K. Chakrabarti, V.K. Mathur, L.A. Thomas, and R.J. Abbundi. Evidence of V^- centers in trivalent rare-earth doped MgS. *Physical Review B*, 38:894–896, 1988.

[70] P.I. Paulose, G. Jose, V. Thomas, N.V. Unnikrishnan, and M.K.R. Warrier. Sensitized fluorescence of Ce^{3+}/Mn^{2+} system in phosphate glass. *Journal of Physics and Chemistry of Solids*, 64:841–846, 2003.

[71] Y.C. Fang, Z.J. Zhang, Z.Q. Xie, Y.Y Zhao, and M. Lu. Photoluminescence enhancement of Si nanocrystals embedded in SiO_2 matrix by CeF_3 doping. *Applied Physics Letters*, 86:191919, 2005.

[72] Z.-Q. Xie, D. Chen, Z.-H. Li, Y.-Y. Zhao, and M. Lu. A combined approach to greatly enhancing the photoluminescence of Si nanocrystals embedded in SiO_2. *Nanotechnology*, 18:115716, 2007.

[73] Y.Q. Li, G. de With, and H.T. Hintzen. Luminescence properties of Ce^{3+}-activated alkaline earth silicon nitride $M_2Si_5N_8$ $(M = Ca, Sr, Ba)$ materials. *Journal of Luminescence*, 116:107–116, 2006.

[74] D. de Graaf, H.T. Hintzen, and G. de With. The influence of the composition on the luminescence of $\mathrm{Ce(III)} - \mathrm{Ln} - \mathrm{Si} - \mathrm{Al} - \mathrm{O} - \mathrm{N}$ glasses $(\mathrm{Ln} = \mathrm{Sc}, \mathrm{Y}, \mathrm{La}, \mathrm{Gd})$. *Journal of Luminescence*, 104:131–136, 2003.

[75] H. Ennen, J. Schneider, G. Pomrenke, and A. Axmann. 1.54-μm luminescence of erbium-implanted $\mathrm{III} - \mathrm{V}$ semiconductors and silicon. *Applied Physics Letters*, 43:943–945, 1983.

[76] D.J. Eaglesham, J. Michel, E.A. Fitzgerald, D.C. Jacobson, J.M. Poate, J.L. Benton, A. Polman, Y.-H. Xie, and L.C. Kimerling. Microstructure of erbium-implanted Si. *Applied Physics Letters*, 58:2797–2799, 1991.

[77] Y.H. Xie, E.A. Fitzgerald, and Y.J. Mii. Evaluation of erbium-doped silicon for optoelectronic applications. *Journal of Applied Physics*, 70:3223–3228, 1991.

[78] J. Michel, J.L. Benton, R.F. Ferrante, D.C. Jacobson, D.J. Eaglesham, E.A. Fitzgerald, Y.-H. Xie, J.M. Poate, and L.C. Kimerling. Impurity enhancement of the 1.54-μm Er^{3+} luminescence in silicon. *Journal of Applied Physics*, 70:2672–2678, 1991.

[79] A. Dorofeev, E. Bachilo, V. Bondarenko, N. Gaponenko, N. Kazuchits, A. Leshok, G. Troyanova, N. Vorozov, V. Borisenko, H. Gnaser, W. Bock, P. Becker, and H. Oechsner. Strong 1.54 μm luminescence from erbium-doped porous silicon. *Thin Solid Films*, 276:171–174, 1996.

[80] U. Hommerich, F. Namavar, A. Cremins, and K.L. Bray. A spectroscopic study on the luminescence of Er in porous silicon. *Applied Physics Letters*, 68:1951–1953, 1996.

[81] X. Wu, U. Hommerich, F. Namavar, and A.M. Cremins-Costa. Correlation between visible and infrared (1.54 μm) luminescence from Er-implanted porous silicon. *Applied Physics Letters*, 69:1903–1905, 1996.

[82] G. Franzo, V. Vinciguerra, and F. Priolo. The excitation mechanism of rare-earth ions in silicon nanocrystals. *Applied Physics A*, 69:3–12, 1999.

[83] N.-M. Park, T.-Y. Kim, S.H. Kim, G.Y. Sung, K.S. Cho, J.H. Shin, B.-H. Kim, S.-J. Park, J.-K. Lee, and M. Nastasi. Luminescence of Er-doped amorphous silicon quantum dots. *Thin Solid Films*, 475:231–234, 2005.

[84] N.-M. Park, T.-Y. Kim, K.-H. Kim, G.Y. Sung, B.-H. Kim, S.-J. Park, K.S. Cho, J.H. Shin, J.-K. Lee, and M. Nastasi. Effect of amorphous Si quantum dot size on 1.54 μm luminescence of Er. *Journal of the Electrochemical Society*, 152:G445–G447, 2005.

[85] Y.C. Fang, Z.Q. Xie, L.-J. Qi, W.-Q. Li, Z.J. Zhang, and M. Lu. The effects of CeF_3 doping on the photoluminescence of Si nanocrystals embedded in a SiO_2 matrix. *Nanotechnology*, 16:769–774, 2005.

[86] C.V. Raman and K.S. Krishnan. A new type of secondary radiation. *Nature*, 121:501, 1928.

[87] B.J. Bulkin. *Analytical Raman Spectroscopy*, chapter The Raman Effect: An Introduction. John Wiley and Sons, 1991.

[88] B.J. Kip and R.J. Meier. Determination of the local temperatures at a sample during Raman experiments using stokes and anti-stokes Raman bands. *Applied Spectroscopy*, 44:707–711, 1990.

[89] D.B. Chase. *Analytical Raman Spectroscopy*, chapter Modern Raman Instrumentation and Techniques. John Wiley and Sons, 1991.

[90] M. Minsky. *US Patent #3,013,467: Microscopy Apparatus*. 1957.

[91] M.J. Matthews, A.L. Harris, A.J. Bruce, and M.J. Cardillo. Characterization of phosphosilicate thin films using confocal Raman microscopy. *Review of Scientific Instruments*, 71:2117–2120, 2000.

[92] N.J. Everall. Confocal Raman microscopy: Why the depth resolution and spatial accuracy can be much worse than you think. *Applied Spectroscopy*, 54:1515–1520, 2000.

[93] F. Iacona, G. Franzo, and C. Spinella. Correlation between luminescence and structural properties of Si nanocrystals. *Journal of Applied Physics*, 87:1295, 2000.

[94] J.F. Ziegler. *SRIM, www.srim.org*. 2006.

[95] D.W. Hamby. *Effects of surface damage on the photoluminescence of* ZnO. Ph.D. Dissertation, Oklahoma State University, 2003.

[96] J.W. Beletic. *Optics in Astrophysics*, chapter Optical and Infrared Detectors for Astronomy. Springer-Verlag, 2005.

[97] D.E. Aspnes and A.A. Studna. Dielectric functions and optical parameters of Si, Ge, GaP, GaAs, GaSb, InP, InAs, and InSb from 1.5 to 6.0 eV. *Physical Review B*, 27:985–1009, 1983.

[98] R. Braunstein, A.R. Moore, and F. Herman. Intrinsic optical absorption in germanium-silicon alloys. *Physical Review*, 109:695–710, 1958.

[99] S.M. Sze. *Physics of Semiconductor Devices*. John Wiley and Sons, 2nd edition, 1981.

[100] J.I. Cisneros. Optical characterization of dielectric and semiconductor thin films by use of transmission data. *Applied Optics*, 37:5262–5270, 1998.

[101] M. Brun, S. Huant, J.C. Woehl, J.-F. Motte, L. Marsal, and H. Mariette. Excitons and multi-excitons in single CdTe quantum dots probed by near-field spectroscopy. *Solid State Communications*, 121:407–410, 2002.

[102] M.L. Brongersma, P.G. Kik, A. Polman, K.S. Min, and H.A. Atwater. Size-dependent electron-hole exchange interaction in Si nanocrystals. *Applied Physics Letters*, 76:351–352, 2000.

[103] L. Dal Negro, J.H. Yi, J. Michel, L.C. Kimerling, T.-W.F. Chang, V. Sukhovatkin, and E.H. Sargent. Light emission efficiency and dynamics in silicon-rich silicon nitride films. *Applied Physics Letters*, 88:233109, 2006.

[104] W. Dungen, R. Rob, Y. Ma, Y.L. Huang, W.R. Fahrner, L.O. Keller, and J.T. Horstmann. μ-Raman investigations on hydrogenated gettering in hydrogen implanted and hydrogen plasma treated czochralski silicon. *Solid State Phenomena*, 108-109:9196, 2005.

[105] O. Moutanabbir, B. Terreault, M. Chicoine, and F. Schiettekatte. The fluence effect in hydrogen-ion cleaving of silicon at the sub-100-nm scale. *Applied Physics A*, 80:1455–1462, 2006.

[106] F.-M. Liu, B. Ren, J.-W. Yan, B.-W. Mao, and Z.-Q. Tian. Initial oxidation processes on hydrogenated silicon surfaces studied by *in situ* Raman spectroscopy. *Journal of the Electrochemical Society*, 149:G95–G99, 2002.

[107] S.E. Alexandrov, M.L. Hitchman, and S.H. Shamlian. Bonded hydrogen in silicon nitride films deposited by remote plasma-enhanced chemical vapour deposition. *Journal of Materials Chemistry*, 4:1843–1847, 1994.

[108] L.J. Bellamy. *The Infrared Spectra of Complex Molecules*. Chapman and Hall, 2nd edition, 1980.

[109] T. Vo-Dinh, editor. *Biomedical Photonic Handbook*, chapter Spectroscopic data of biologically and medically relevant spieces and samples. CRC Press, 2002.

[110] N.M. Rocher, R. Frech, and M. Khan. Hydrogen bonding and the inductive effect in crystalline and solution phases of hexylamine:$LiCF_3SO_3$ and dipropylamine:$LiCF_3SO_3$: Application to branched poly(ethylenimine). *Journal of Physical Chemistry B*, 109:20697–20706, 2005.

[111] S.E. Alexandrov, M.L. Hitchman, and S.H. Shamlian. Formation of silicon nitride films by remote plasma-enhanced chemical vapour deposition. *Advanced Materials for Optics and Electronics*, 2:301–312, 1993.

[112] K.S. Min, K.V. Shcheglov, C.M. Yang, H.A. Atwater, M.L. Brongersma, and A. Polman. Defect-related versus excitonic visible light emission from ion beam synthesized Si nanocrystals in SiO_2. *Applied Physics Letters*, 69:2033–2035, 1996.

[113] B.G Fernandez, M. Lopez, C. Garcia, A. Perez-Rodriguez, J.R. Morante, C. Bonafos, M. Carrada, and A. Claverie. Influence of average size and interface passivation on the spectral emission of Si nanocrystals embedded in SiO_2. *Journal of Applied Physics*, 91:798–807, 2002.

[114] Z. Iqbal, S. Veprek, A.P. Webb, and P. Capezzuto. Raman scattering from small particle size polycrystalline silicon. *Solid State Communications*, 37:993–996, 1981.

[115] G. Yu, G. Chen, and F. Zhang. Theoretical study of the Raman spectrum in a-$Si_{1-x}N_x$:H films. *Physica Status Solidi B*, 152:7378, 1981.

[116] F.L. Galeener. Band limits and the vibrational spectra of tetrahedral glasses. *Physical Review B*, 19:4292–4297, 1978.

[117] S.K. Sharma, J.F. Mammone, and M.F. Nicol. Raman investigation of ring configurations in vitreous silica. *Nature*, 292:140–141, 1981.

[118] J. Bandet, B. Despax, and M. Caumont. Nitrogen bonding environments and local order in hydrogenated amorphous silicon nitride films studied by Raman spectroscopy. *Journal of Applied Physics*, 85:7899–7904, 1999.

[119] J.-K. Lee, T.A. Harriman, D.A. Lucca, H.S. Jung, D.B. Ryan, and M. Nastasi. Dynamic recovery and optical properties changes in He-implanted ZnO nanoparticles. *Nuclear Instruments and Methods B*, 257:71–74, 2007.

[120] W. Di, X. Wang, P. Zhu, and B. Chen. Energy transfer and heat-treatment effect of photoluminescence in Eu^{3+}-doped $TbPO_4$ nanowires. *Journal of Solid State Chemistry*, 180:467–473, 2007.

[121] J. Skov Jensen, T.P. Leervad Pedersen, J. Chevallier, B. Bech Nielsen, and A. Nylandsted Larsen. Rare earth ions and Ge nanocrystals in SiO_2. *Nanotechnology*, 17:2621–2624, 2006.

[122] A.J. Kenyon, C.E. Chryssou, C.W. Pitt, T. Shimizu-Iwayama, D.E. Hole, N. Sharma, and C.J. Humphreys. Luminescence from erbium-doped silicon nanocrystals in silica: Excitation mechanisms. *Journal of Applied Physics*, 91:367–374, 2002.

[123] G. Qin, G.G. Qin, and S.H. Wang. Theory for photoluminescence from SiO_2 films containing Si nanocrystals and Er ions. *Journal of Applied Physics*, 85:6738–6745, 1999.

[124] K. Imakita, M. Fujii, and S. Hayashi. The mechanism of energy transfer from Si nanocrystals to Er ions in SiO_2. *European Physical Journal D*, 34:161–163, 2005.

[125] M. Anni, L. Manna, R. Cingolani, D. Valerini, A. Creti, and M. Lomascolo. Förster energy transfer from blue-emitting polymers to colloidal CdSe/ZnS core shell quantum dots. *Applied Physics Letters*, 85:4169–4171, 2004.

[126] D. Kovalev, E. Gross, N. Kunzner, F. Koch, V.Y. Timoshenko, and M. Fujii. Resonant electronic energy transfer from excitons confined in silicon nanocrystals to oxygen molecules. *Physical Review Letters*, 89:137401, 2002.

[127] T. Förster. Zwischenmolekulare energiewanderung und fluoreszenz. *Ann. Phys.*, 2:166–175, 1948.

[128] T. Förster. *Biological Physics*, chapter Intermolecular energy migration and fluorescence. American Institute of Physics, 1993.

[129] T. Förster. *Istanbul Lectures, Part III: Action of Light and Organic Crystals*, chapter Delocalized excitation and excitation transfer. Academic Press, 1965.

[130] Olympus. *SRIM, www.olympusfluoview.com/applications/fretintro.html*. 2008.

[131] V. May and O. Kühn, editors. *Charge and Energy Transfer Dynamics in Molecular Systems*. Wiley-VCH, 2000.

[132] A. Polman, D.C. Jacobson, D.J. Eaglesham, R.C. Kistler, and J.M. Poate. Optical doping of waveguide materials by MeV Er. *Journal of Applied Physics*, 70:3778, 1991.

[133] D.L. Andrews and A.A. Demidov, editors. *Resonance Energy Transfer*. Wiley, 1999.

[134] P.R. Selvin. Lanthanide-based resonance energy transfer. *IEEE Journal of Selected Topics in Quantum Electronics*, 2:1077–1087, 1996.

[135] A. Vedda, N. Chiodini, D. Di Martino, M. Fasoli, F. Morazzoni, F. Moretti, R. Scotti, G. Spinolo, A. Baraldi, R. Capelletti, M. Mazzera, and M. Nikl. Insights into microstructural features governing Ce^{3+} luminescence efficiency in sol-gel silica glasses. *Chemistry of Materials*, 18:6178–6185, 2006.

[136] Y. Kanemitsu. Efficient light emission from crystalline and amorphous silicon nanostructures. *Journal of Luminescence*, 100:209–217, 2002.

[137] J.A. Caird. *Handbook of Lasers*, chapter Crystalline Paramagnetic Ion Lasers. CRC Press, 2001.

[138] K. Aono and M. Iwaki. Ion beam-induced luminescence of Eu-implanted Al_2O_3 and CaF_2. *Nuclear Instruments and Methods B*, 118:518–522, 1998.

[139] K. Aono, M. Iwaki, and S. Namba. Luminescence during Eu-implantation into calcium fluoride. *Nuclear Instruments and Methods B*, 32:231–234, 1988.

[140] K. Aono, M. Iwaki, and S. Namba. Luminescence during Eu, Fe, and Cr implantation into CaF_2. *Nuclear Instruments and Methods B*, 46:220–223, 1990.

[141] E. Alves, K. Lorenz, and R. Vianden. Optical doping of nitrides by ion implantation. *Modern Physics Letters B*, 15:1281–1287, 2001.

[142] S. Magalhaes, K. Lorenz, M. Peres, T. Monteiro, S. Tripathy, and E. Alves. Implantation of nanoporous GaN with Eu ions. *Nuclear Instruments and Methods B*, 257:328–331, 2007.

[143] S.V. Upadeo and S.V. Moharil. Radiation-induced valence changes in Eu-doped phosphors. *Journal of Physics: Condensed Mater*, 9:735–746, 1997.

[144] N. Salah, P.D. Sahare, and A. Prasad. Thermoluminescence and photoluminescence of $LiNaSO_4$: Eu irradiated with 24 and 48MeV ^{7}Li ion beam. *Journal of Luminescence*, 121:497–506, 2006.

[145] O.M. Ntwaeaborwa and P.H. Holloway. Enhanced photoluminescence of Ce^{3+} induced by an energy transfer from ZnO nanoparticles encapsulated in SiO_2. *Nanotechnology*, 16:865–868, 2005.

[146] W. Cai, H. Zhou, and L. Zhang. Luminescence of aggregated and dispersed nanosized cerium doped silica particles. *Journal of Materials Science Letters*, 18:1849–1851, 1999.

[147] I. De Wolf. Stress measurements in Si microelectronics devices using Raman spectroscopy. *Journal of Raman Spectroscopy*, 30:877–883, 1999.

[148] M. Levinshtein, S. Rumyantsev, and M. Shur, editors. *Handbook series on semiconductor parameters*. World Scientific, 1996.

[149] T.-W. Kim, C.-H. Cho, B.-H. Kim, and S.-J. Park. Quantum confinement effect in crystalline silicon quantum dots in silicon nitride grown using SiH_4 and NH_3. *Applied Physics Letters*, 88:123102, 2006.

Appendix A

Operation of WITec Alpha SNOM in Confocal Mode

The following is a checklist outlining the basic usage of the WITec Alpha SNOM while in the confocal configuration. It is not intended to replace the user manuals provided by the manufacturers of the devices in question, nor to fully describe all safety procedures, but merely to cover the salient points regarding the operation and use of this instrument.

Startup

1. After verifying that the shutter is closed, power on the desired laser.
2. Turn on and enable the active vibration isolation system.
3. Turn on the monochromator,
4. On the computer open the programs 'ScanCtrl Spectroscopy Plus 1.34' and 'WITec Video Ctrl 1.16'.
5. Verify in the CCD Settings window that the target temperature of the CCD in the software is set to $-75\,^{\circ}$C and press the 'Cooler On' button.
6. Select the Raman mode in the Hardware Options menu and make the appropriate selections of units and laser wavelength in the Spectrograph window.
7. Verify that the Z-Stage switch on the controller is on, the Z-Control Input does not have a cable attached, and the Z-DC Offset is adjusted to 10 μm.

8. If it is not already in place, the beamsplitter for the desired laser needs to be in place on the microscope. Once in place verify that proper optical fiber coming from the laser coupler is firmly attached. Note that it is important when connecting or removing any optical fiber that there is no signal being transmitted. If it is transmitting, there is a risk of irreparable damage due to potentially large power densities and localized heating of anything in contact with the fiber tip. Dust or oils on the tip can have the same effect; care should be taken to not leave the fiber exposed to the environment and if necessary cleaned by gently wiping it on a business card.

9. After the laser has been given 20 to 30 minutes to reach steady state and the CCD temperature reaches its minimum (usually $-73\,^{\circ}\mathrm{C}$), the system is ready for measurements.

Aligning confocal pin-hole fiber

1. Especially if the beamsplitter was replaced, the confocal pinhole must be aligned and the signal optimized.

2. To do this mount a reference specimen (bulk ZnO for PL and bulk Si for Raman) on the scan stage. Note that depending upon the objective, a top cover glass slide may be required.

3. Under white light illumination and using the eyepiece video camera, use the remote control to focus on the surface of the specimen with the upright objective. When using flat and relatively pristine specimens, it may be impossible to know when it is in focus; closing the field diaphragm and making sure that it is in focus will ensure that the specimen is in focus.

4. Block the white light source and unblock the laser and set it to a low power.

5. The video camera will show a series of laser spots that are grouped together in the bottom center of the field of view (these are internal reflections within the microscope) and a single spot in the upper center of the field of view (this is the excitation spot). If the reflected spots do not appear sharp, adjust the collimation next to the optical fiber input unit to ensure that the beam is parallel.

6. Focus on the specimen to minimize the excitation spot size.

7. Block the laser and remove confocal pin-hole fiber. Be careful not to look into the fiber connector at any time.

8. Unblock the laser and divert the signal from the video camera to the fiber connector.

9. Using a piece of paper held above the connector find the excitation spot (this will likely require increasing the laser power) and use the micrometer screws to position this spot in the center of the output coupler.

10. Block the laser again and reattach the confocal pin-hole fiber.

11. Unblock the laser and select an appropriate grating and spectral center in the Spectrograph window. For PL center on the 380 nm emission of the ZnO and for Raman center on the 520 cm^{-1} peak of Si. Try not to include the main laser wavelength or any of its harmonics in the collected spectra since the CCD will be overflow and possibly damaged with 65,000 counts.

12. If performing Raman measurements put the laser blocking filter in the beam path.

13. Starting with a small integration time (0.01 to 0.1 s) use FOCUS SPECTRUM to start continuously collecting spectra. If no signal is observed make small movements to the fiber coupler micrometer screws. If still no signal is observed return to the earlier step of centering the excitation spot on a piece of paper. If the proper signal is observed then optimize the signal with one of the fiber coupler micrometer screws. Once a maximum is reached, use the second fiber coupler micrometer screw. When the maximum is reached use the remote control to focus up and down until a maximum signal is reached. Repeat each of these three optimizations until there is no improvement in the signal intensity.

14. The pin-hole position is now optimized and measurements can begin.

Measurements

1. Startup the WITec system.

2. Verify that the confocal pin-hole is aligned and its signal throughput is maximized.

3. Place the specimen on a glass slide. If the objective in use is corrected for a cover glass slide then place one on the top surface.

4. For Raman spectroscopy make certain that the specimen surface is perpendicular to the microscope objective. For PL spectroscopy, unless the emission is sufficiently intense, the specimen should be tilted to reduce the intensity of plasma lines that make it to the CCD detector.

5. Under white light illumination and using the eyepiece video camera, use the remote control to focus on the surface of the specimen with the upright objective. When using flat and relatively pristine specimens, it may be impossible to know when it is in focus; closing the field

diaphragm and making sure that it is in focus will ensure that the specimen is in focus. Note that depending upon the objective, a top cover glass slide may be required.

6. Block the white light source and unblock the laser with its power set to a low setting to start (i.e., a micrometer reading ¡ 1.50).

7. The video camera will show a series of laser spots that are grouped together in the bottom center of the field of view (these are internal reflections within the microscope) and a single spot in the upper center of the field of view (this is the excitation spot). If the reflected spots do not appear sharp, adjust the collimation next to the optical fiber input unit to ensure that the beam is parallel.

8. Focus on the specimen to minimize the excitation spot size.

9. If performing Raman measurements put the laser blocking filter in the beam path.

10. Divert the signal from the video camera to the fiber connector.

11. Starting with a small integration time (0.01 to 0.1 s) use FOCUS SPECTRUM to collect a spectrum. Incrementally increase the integration time until the signals are measurable, with care being taken not to allow any region of the spectrum to reach 65,000 counts since this would cause the CCD to saturate.

12. After determining an optimal integration time measurements can be made using the SINGLE SPECTRUM (collects a single spectrum at a single point in space), TIME SPECTRUM (collects multiple spectra at different time intervals), LINE SPECTRUM (collects multiple spectra evenly spaced along a 2-D line in space), or IMAGE SPECTRUM (collects multiple spectra evenly spaced across a plane through space).

VITA

Tres Harriman

Candidate for the Degree of

Masters of Science

Thesis: EFFECTS OF LANTHANOID ION IMPLANTATION ON THE PHOTOLUMINESCENCE OF SILICON NANOCRYSTALS EMBEDDED IN SILICON NITRIDE FILMS

Major Field: Mechanical Engineering

Biographical:

Personal Data: Born in Elkhart, KS, USA on February 24, 1981, the son of Carman and Jan Harriman.

Education:
Graduated from David H. Hickman High School, Columbia, Missouri in June 1999. Received the Bachelor of Science degree in Mechanical Engineering from the University of Missouri, Columbia, Missouri in December 2003. Completed the requirements for the Master of Science in Mechanical Engineering at Oklahoma State University, Stillwater, Oklahoma in July, 2008.

Experience:
Student supervisor, University Bookstore, 1999 to 2004; Substitute teacher, Columbia Public Schools, 2004 to 2005; Graduate research/teaching assistant, Oklahoma State University, 2005 to present.

Professional Memberships:
Order of the Engineer, Student member ASTM International.

Name: Tres A. Harriman Date of Degree: July, 2008

Institution: Oklahoma State University Location: Stillwater, Oklahoma

Title of Study: EFFECTS OF LANTHANOID ION IMPLANTATION ON THE PHOTOLUMINESCENCE OF SILICON NANOCRYSTALS EMBEDDED IN SILICON NITRIDE FILMS

Pages in Study: 77 Candidate for the Degree of Master of Science

Major Field: Mechanical Engineering

A study on the effects of lanthanoid ion implantation on the optical behavior of Si nanocrystals synthesized in 200 nm thick amorphous SiN_x films has been performed. The Si nanocrystals were fabricated using plasma enhanced chemical vapor deposition (PECVD) on (100) Si substrates. By regulating the flow rate of reactant gases, Ar-diluted SiH_4 and N_2, the resulting nanocrystal size could be controlled. The synthesized films were investigated by photoluminescence (PL) spectroscopy and Raman spectroscopy.

Due to quantum confinement effects the three different sizes of Si nanocrystals investigated, 2.6, 3.0, and 3.9 nm, had PL emissions of 2.85, 2.48, and 1.97 eV, respectively. The Si:Si_xN_y films were subsequently implanted with lanthanoid ions and finally heat treated to reduce implantation damage. Specific ions used in this study were Ce^{2+}, Eu^{2+}, Tb^{2+}, and Nd^{2+}, all with incident energies of 63 keV and a fluence of 1×10^{15} ions/cm^2.

In the as-implanted films, Ce^{3+} ions led to an increase in the PL intensity of the small and medium nanocrystals. This behavior was not observed for the other ion species. After each of the two independent heat treatment cycles, the Ce-doped small particles showed further intensified PL emission, while the emission from the Ce-doped medium particle emission blue-shifted.

The observed PL intensity increase and blue shifting from the Si nanocrystals appears to result from an energy transfer from Ce ions to the Si nanocrystals that is dependent upon the nanocrystal size, with energy being preferentially transferred to smaller Si nanocrystals. The exact nature of the transfer mechanism requires further study.

A follow up investigation examined the effect of Ce ion fluence on the PL response of the Si nanocrystals. As the fluence increased from 3×10^{19}, to 5×10^{20}, and to 1×10^{26} ions/cm^2, the smallest particles showed a continual PL intensity increase, the medium particles showed an increase for the first two fluences and a decrease for the highest fluence, and the largest particles showed a continual decrease in PL intensity. This behavior is attributed to concentration quenching effects.

ADVISOR'S APPROVAL: ______________________________